High-Resolution, Quantitative, and Three-Dimensional Coherent Diffractive Imaging with a Tabletop EUV Source

by

Elisabeth Rose Shanblatt

B.S., New York University, 2010

M.S., University of Colorado Boulder, 2014

A thesis submitted to the

Faculty of the Graduate School of the

University of Colorado in partial fulfillment

of the requirements for the degree of

Doctor of Philosophy

Department of Physics

2017

This thesis entitled:
High-Resolution, Quantitative, and Three-Dimensional Coherent Diffractive Imaging with a Tabletop EUV Source
written by Elisabeth Rose Shanblatt
has been approved for the Department of Physics

Prof. Margaret M. Murnane

Prof. Henry C. Kapteyn

Date

The final copy of this thesis has been examined by the signatories, and we find that both the content and the form meet acceptable presentation standards of scholarly work in the above mentioned discipline.

Shanblatt, Elisabeth Rose (Ph.D., Physics)

High-Resolution, Quantitative, and Three-Dimensional Coherent Diffractive Imaging with a Tabletop EUV Source

Thesis directed by Prof. Margaret M. Murnane

Imaging is a critical tool used across a broad range of applications in science, technology, medicine, and manufacturing. Microscopy, the type of imaging which allows us to access the elusive yet rich world of what is smaller than we can naturally see– makes it possible to observe and design the nano-world of biological, material, and nanofabricated systems.

In this thesis, I describe the development of a new type of microscopy that combines two powerful tools: coherent extreme ultraviolet (EUV) light sources produced by high harmonic generation, and ptychographic coherent diffractive imaging. This microscope produces high-resolution, chemically-specific, phase- and amplitude- contrast images with large fields of view on the order of hundreds of microns, while preserving a high spatial resolution on the scale of tens of nanometers.

Recently, we extended this new tabletop microscopy technique to image reflective samples, periodic samples, and to image dynamic nano-scale elastic and thermal processes. I will discuss these advances and in particular demonstrate two new capabilities: first, a new imaging technique with high compositionally- and morphologically-sensitive quantitative information, capable of imaging reactions and diffusion at a buried interface. This capability will open up a new, exquisitely sensitive layer-by-layer imaging that has many applications in nanoscience and nanotechnology, including surface and materials science and metrology. Secondly, I will demonstrate imaging of a thick sample in three dimensions. By accounting for diffraction within a thick sample, it is possible to obtain high-resolution three-dimensional images of biological and meta-material samples non-invasively, and without the use of staining or labeling.

Dedication

To my family.

Acknowledgements

Firstly, I would like to thank and acknowledge my advisors, Professors Margaret Murnane and Henry Kapteyn. Their generous support, guidance, and scientific insight have helped shape me professionally and personally, and have made working in their group a pleasure. It is a privilege to share some small part in their legacy.

I also want to thank my mentors, Professor Daniel Adams and Doctors Giulia Mancini, Matthew Seaberg, Bosheng Zhang, and Dennis Gardner.

Dan has been a part of the Imaging Team for a long time, and taught me much of what I needed to know to complete the work done in this thesis. He has also shown by example what a scientific mentor should be; demonstrated by technical ability, leadership, project management, skill and commitment to teaching, and keeping the lab a fun and productive environment.

Giulia joined us two years ago, and in that time has made a tremendous impact. Her technical abilities, creative ideas, and thoughtful scientific advice have advanced and enabled every experiment she has been a part of. Additionally, her kindness, sense of humor, and generosity make her a key component to both lab productivity and positivity.

Matt, Bosheng, and Dennis gave me a great start within the Imaging Team and taught me a lot of what I know about the experiment and being a grad student. Additionally, their years of hard work and dedication built the foundation on which the work in this thesis was done. They each accomplished an incredible amount during their time in the lab, and while being hard acts to follow, their work ethics, creativity, and accomplishments have been inspiring.

I also want to acknowledge the newer members of the imaging team that have joined over

the past few years. Charles Bevis, who is taking over the 3D project, has been a delight to work with and mentor. I am pleased to be leaving the project in such good hands, and look forward to what he will accomplish. Christina Porter, Robert Karl, Michael Tanksalvala, and our newest additions Bin Wang and Peter Johnsen have all shown the dedication and creativity necessary to push imaging capabilities further over the coming years.

I want to thank the rest of the KM group at JILA and KMLabs who I have been able to work with over the years. Thank you to Nico Hernandez-Charpak, Franklin Dollar, Chris Mancuso, Tory Carr, Susannah Brown, Daisy Raimondson, Xiaoshi Zhang, Sterling Backus, Michael Gerrity, Patrik Grychol, Seth Cousin, Tenio Popmintchev, Bill Peters, Kevin Dorney, Jennifer Ellis, Travis Frazer, Ming-Chang Chen, Ben Galloway, Tingting Fan, Maithreyi Gopalakrishnan, Daniel Hickstein, Dmitriy Zusin, and everyone else, past and present, who has been a part of the group. I also want to thank a few of our many collaborators: John Miao, John Badding, Justin Shaw, and Weilun Chao.

None of this would be possible without the help of JILA staff. In particular, David Alchenberger, Hans Green, J.R. Raith, and Lauren Mason have provided valuable technical and administrative support that keep things running. I also want to thank the rest of JILA staff; administrative, machine shop, computing, electronic, purchasing, and custodial. Thank you to the Physics department staff, and the Women in Physics group for all the lunches, support, and discussions over the years.

I also want to thank my undergraduate advisor and mentor, Professor David Grier, who got me started in research and whose advice, encouragement, and wisdom was instrumental in my decision and opportunity to pursue a Ph.D. Thank you also to my colleagues from the Grier group and everyone from the NYU physics department who helped me throughout undergraduate classes, research, and grad school applications.

Another incredibly important group of people I need to thank are my friends. Thank you Nicky Squyres, Cathy Klauss, AJ Johnson, Ben Pollard, Yomay Shyur, Sara Campbell, Bob Peterson, Andrew Koller, Nico Hernandez-Charpak, Victor Collussi, Suzannah Sterten, Brian

O'Callahan, Jack Houlton, Michelle Miller, Scott Johnson, Helen McCreery, Dani Merriman, Brad Johnson, Charlie Goodwin, Alex Tingle, Teesa Christian, Ben Chapman, Oscar Henriksson, and everyone else I have had adventures, homework sessions, lunch table banter, and coffee breaks with over the years.

I want to thank the love of my life, Andy Missert, for his support, kindness, patience, and love– and for teaching me so many important things about both physics and life.

Finally, I want to thank my sister Em, and my Mom and Dad for their continuous encouragement, love, and advice. I couldn't have done this without you.

Contents

Chapter

Tables

Table

Figures

Figure

Chapter 1

Introduction and Motivation

Efforts to understand the universe by observing the electromagnetic radiation emitted by distant galaxies, noninvasively looking inside the human body to diagnose illnesses, and testing the laws of quantum mechanics all require the control, use, and understanding of light. Light is one of the most useful tools for furthering technology and learning about the natural world, and its use continues to change and improve our relationship to nature and technology.

The interaction of light and matter is an enormous field of study permeating nearly every field of science. In general, the use of light or other materials to observe features smaller than those easily resolvable by the human eye is known as microscopy.

This thesis discusses the ongoing development of a new type of microscopy which uses coherent extreme ultraviolet (EUV) light, which is more than 20 times shorter wavelength than visible light and therefore much more sensitive to nanoscale structures. This light is upconverted from the near-infrared using high harmonic generation– a tabletop technique, making it accessible to high-throughput laboratory environments, as well as industrial settings. This new microscope is capable of imaging many different kinds of objects on the nanometer scale, and is a tool ideally suited for exploring the fundamental physics and technological applications of the nano-world.

1.1 Exploring the micro- and nano-world with microscopy

1.1.1 Historical perspective

The compound lens light-based microscope was first invented by the Dutch spectacle-makers Hans and Zacharias Jansen in 1595. However, the first published scientific use of a microscope was not until 1665, when Robert Hooke published *Micrographia*, including detailed illustrations of the invention [1, 2]. Early microscopes like this were based on the use of two lenses; the objective lens, which magnified the image, and the eyepiece, which the user would look through to view the image. Though variations on this model are still in use today, microscopes have expanded to include the use of all different wavelengths of light and even particles such as electrons, as well as the power of computational and fluorescence techniques [3–5].

A major development in microscopy came in 1873, when Ernst Abbe, building on the work of George Airy and Emile Verdet, formalized the diffraction limit of light, stating that the smallest resolvable feature cannot be smaller than half the wavelength of the illuminating light [1, 6]. This limit is still in use for many techniques today, and will be referred to many times in this thesis.

Essentially all microscopy techniques up until the early 20^{th} century only measured the intensity of the wave, and missed much of the available information– the phase. However, a breakthrough came in 1942, when Frits Zernike invented the phase contrast microscope. By using a phase plate of etched glass, he was able to convert phase differences due to the scattering of the sample to amplitude differences in the image, resulting in much higher contrast [1, 7], and therefore much more information about the sample. This invention earned Zernike the 1953 Nobel Prize in Physics [8].

Today, microscopy is an important tool in nearly every branch of science and technology. New types of microscopes, suitable for imaging different types of systems, are under constant development. To understand the context in which coherent EUV microscopy fits, some important types of microscopy will now be discussed, along with some fundamentals.

1.1.2 Imaging and microscopy fundamentals

Before diving in to the different types of microscopy, some basics and definitions used in imaging will be mentioned. This will serve as a primer to the different types of microscopies, discussed in the next subsection.

1.1.2.1 Amplitude versus phase information

For the purpose of optics and imaging, light can be considered a complex wave of the form

$$\psi = \sqrt{I}e^{i\phi} \tag{1.1}$$

where I is the intensity–usually what is measured by detectors– and ϕ is the phase. The quantities I and ϕ are both real. The quantity $\sqrt{I}$ is known as the amplitude, A. Over distances of propagation, amplitude and phase information can mix. Visible interference fringes are a good example of this.

Often, for visible wavelengths of light, the amplitude carries information about absorption and phase carries information about structure. Objects that do not significantly attenuate the light are known as phase objects. For instance, a glass lens focusing visible light is a phase object. It works be imparting a quadratic phase on the wave, which in turn focuses the beam. This illustrates that the phase carries a lot of important information about the field, but it is lost on detectors that only measure intensity, which is the case for many detectors. Fortunately, there are a number of phase imaging techniques that allow either the phase information to be translated into amplitude information, or that allow the phase to be algorithmically solved for. The topic of phase imaging, and what information is gained from the phase of an image, is discussed in detail in Chapter 2.

1.1.2.2 Focusing and image formation

A fundamental equation in imaging is known as the Lensmaker's equation. It describes where an image will be formed with an optic of a given focal length,

$$\frac{1}{f} = \frac{1}{d_o} + \frac{1}{d_i} \tag{1.2}$$

where f is the focal length, d_o is the object distance, and d_i is the image distance. The magnification of the image with respect to the object is given by [8]

$$M = -\frac{d_i}{d_o}. \tag{1.3}$$

1.1.2.3 Resolution

Ernst Abbe developed the commonly used measure of diffraction-limited resolution, that the smallest resolvable feature Δr is greater than or equal to half of the illuminating wavelength, $\lambda/2$ [8]. Rayleigh's criterion states that two objects are resolved when the maximum of one object's diffraction pattern is at the position of a neighboring object's first minimum. For circular apertures, the diffraction will be in the shape of an Airy function, which is related to a Bessel function of the first kind, $J_1(x)$. More precisely, the first zero of the Airy function is the first zero of $J_1(x)/\pi$. This value is approximately equal to 1.22. Then, the smallest resolvable feature for such an imaging system is [8]

$$\Delta r = \frac{1.22\lambda}{2n\,sin\theta} \tag{1.4}$$

where Δr is the smallest resolvable feature, λ is the illuminating wavelength, n is the refractive index, and θ is the collection angle, illustrated in Fig. 1.4. In vacuum, and to a good approximation in air, n is equal to 1. It is convenient to make the approximation $1.22 \approx 1$, so the equation reduces to

$$\Delta r \approx \frac{\lambda}{2NA} \tag{1.5}$$

where NA (numerical aperture), defined as $sin\theta$, is a quantity depending on the geometry of the imaging system, and is a measure of how much information the detector can record. There are different resolution criteria used for different applications, for instance, a system with a non-circular aperture may have a different constant multiplying the quantity λ/NA. However, the limit in Eqn. 1.5 is commonly used in imaging. and will be used throughout this thesis.

The NA typically ranges from 0 to 1, where $NA = 1$ sets the diffraction limit of the imaging system. An NA of greater than 1 can be achieved using techniques such immersing an objective

lens in high-refractive index material [9]. The geometrical arguments for this quantity are discussed later in this chapter, but in general, imaging techniques that exceed this diffraction limit, that is, $\Delta r < \lambda/2$, are known as super resolution techniques.

1.1.2.4 Point versus full-field scanning in imaging

There is an important distinction between various scanning techniques. Some imaging modalities such as SEM (scanning electron microscopy) [10], and AFM (atomic force microscopy) [11,12], are imaging techniques which build up an image point-by-point, one pixel at a time. Although the resolution at each pixel might be high, the need for point-by-point scanning makes these techniques more difficult for imaging dynamics, or to study wide areas of the sample in a timely manner. In contrast, other scanning techniques such as ptychography (discussed in detail in Chapter 2) are what are known as "full-field" scanning techniques, where an area greater than one pixel is imaged per scan position. Microscopy techniques such as bright-field imaging are full-field, but do not necessarily employ scanning. These techniques are much more flexible for imaging dynamic systems and high-throughput imaging of large fields-of-view.

1.1.2.5 Coherence

In wave mechanics, coherence is a measure of how correlated the fields of two sources are [13]. The two types of coherence primarily of interest in imaging are the temporal coherence (which can be equivalently thought of as the longitudinal spatial coherence), and transverse spatial coherence.

Longitudinal spatial coherence

Temporal (or longitudinal spatial) coherence indicates the correlation of a beam with itself at a fixed point but at different times. The coherence time, t_c is defined as the time over which the phase of the wave can be predicted at a fixed point. It is related to the frequency bandwidth of the wave, $\Delta\nu$. Temporal coherence can also be thought of as a longitudinal spatial coherence by incorporating a factor of the speed of light c, such that $L_L = ct_c$ [13]. In terms of wavelength, for a wave with bandwidth $\Delta\lambda$ centered around an average wavelength λ_0, the longitudinal coherence

length is a measure of how monochromatic the system is,

$$L_L = \frac{\lambda_0^2}{\Delta\lambda}. \tag{1.6}$$

Transverse spatial coherence

Transverse spatial coherence refers to the correlation between phases at transverse points on the beam. That is, two spatially separated points at a fixed time. For two scattering points, if they are separated by one coherence length, the fringe visibility will be 0.88 [13]. A central assumption of traditional CDI is that the diffraction pattern is proportional to the Fourier transform of the object, which is only true if the illumination is fully coherent.

For a CDI system with a object size D (or beam size D in the case of ptychography), the transverse coherence length L_T much be greater than or equal to D. Otherwise, the fringes at the edge of the detector will not be properly separated, and this will degrade the quality of the reconstructed image [14].

Incoherent and coherent imaging

Many different types of imaging exist for both incoherent and coherent light, as well as partially coherent light. Incoherent sources include light bulbs and the sun. So long as the image forming optic can focus all the different wavelengths to more or less the same place, the image at the image plane (the plane at d_i in Eqn. 1.2) will appear sharp. Generally, the image will only include intensity information. These methods are convenient because a variety of polychromatic bright sources are readily available, and they often do not require much post-processing.

Meanwhile, coherent imaging utilizes light that is at least partially coherent, typically in order to gain some kind of phase information. By using the interference in the imaging system, phase information can be transcribed into amplitude information. The most commonly used coherent source is a laser, but incoherent sources can be made coherent with the use of spectral and spatial filtering. Types of coherent imaging include holography, interferometry, and diffraction imaging.

1.1.3 Modern light-based microscopy

Light-based microscopy spans a wide range of instruments, samples, and applications. The list presented here is not exhaustive, but is meant to introduce some common types of microscopy– particularly ones that will be used throughout this thesis.

1.1.3.1 Bright- and dark-field microscopy

Bright field microscopy is when the sample is illuminated with white light, which is transmitted through the sample, and the image contains various dark shapes due to spatially-dependent absorption. This is the type of microscopy pioneered by Hooke and others in the 1600's, and is still widely used today [1].

In dark field microscopy, images are created by collecting the scattered light from the sample, and thus regions where there is no sample material present show up as dark.

There are many variations on bright-field and dark-field microscopy, but in general, these methods use lenses and visible light, and are diffraction-limited. Therefore, unless other techniques are employed, these types of microscopes cannot resolve features smaller than around 200 nm [1]. Furthermore, because this design involves lenses, it is not suitable for EUV/X-ray imaging, as there are no appropriate refractive optics in the EUV/X-ray wavelength range. This issue is discussed further in Chapter 2.

1.1.3.2 Phase-contrast microscopy

In addition to Zernike phase-contrast microscopy discussed earlier, other methods have been developed to obtain phase information from a sample. Differential interference contrast (DIC) microscopy uses a polarized beam to map path length differences through a sample [15, 16], resulting in phase contrast. Digital holographic microscopy and holographic video microscopy utilize coherent light to record the wavefront scattered from a specimen as a hologram [17]. Holographic video microscopy allows real-time video capture of samples in motion, for instance, in a colloidal suspension, the three-dimensional position, refractive index, and radius of a colloid can be recovered for

each frame [18].

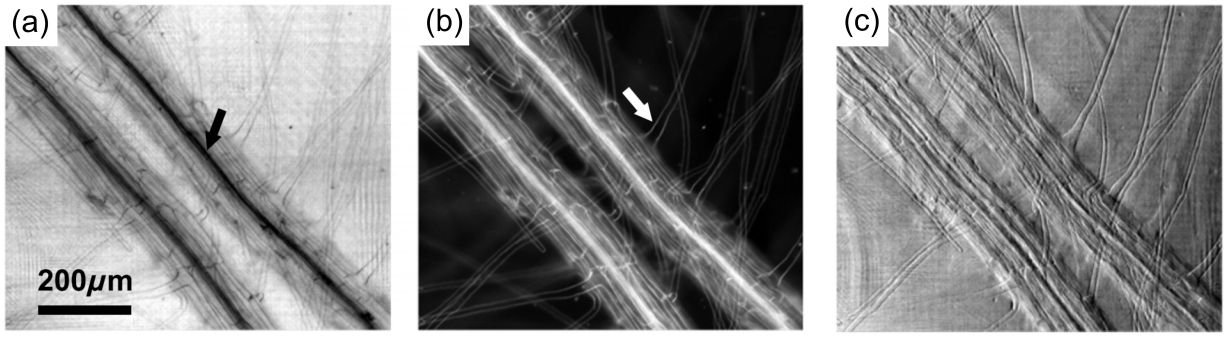

Figure 1.1: **Images taken with bright field, dark field, and phase contrast microscopy**. Images of nutrition tubes in a sample of the *Arabidopsis* plant obtained with (a) bright-field, (b) dark-field, and (c) phase-contrast microscopy. Figure adapted from Ref. [19].

1.1.3.3 Near-field microscopy

The previously mentioned microscopy techniques all detect light in the far-field, meaning that the detector is very far away compared to the size of the sample and the wavelength. However, not all modern microscopy techniques rely on light in the far-field. Some techniques detect light in the near-field. A variety of scanning probe techniques take advantage of evanescent waves in the near field to obtain image resolution far below the diffraction limit. These techniques are generally known as scanning near-field optical microscopy (SNOM, or NSOM), and sometimes employ a metal tip to as a probe. These techniques are excellent for probing surfaces, and have also been combined with spectroscopy to obtain chemical information, surface information, and molecular dynamics [20–23].

1.1.3.4 Fluorescence and super-resolution microscopy

Fluorescence is a property of certain materials to absorb and re-emit a different color of light. While simple optical microscopes use the attenuation or scattering of a material to image, fluorescent microscopes use fluorescence as well, gaining spectral and localization information from the signal. While fluorescence is a natural property of certain materials, it can also be introduced

via a stain or a protein [24, 25].

In the past 20 years, fluorescence microscopy has been able to achieve super-resolution, breaking the diffraction limit. In 2000, stimulated emission depletion (STED) microscopy [26,27] showed super-resolution capabilities using specially constructed beams that only cause fluorophores to emit in certain locations. Photo-activated localization microscopy (PALM) [28] and stochastic optical reconstruction microscopy (STORM) [24] use photoswitchable sparse emitting single-molecule fluorophores to localize the emitters to within tens of nanometers. These techniques earned Eric Betzig, Stefan Hell, and William Moerner the Nobel Prize in Chemistry in 2014 [1].

While super-resolution fluorescence techniques are excellent for biological samples, they are generally invasive and require staining or genetic engineering. They are not readily extended to inorganic or semi-conductor materials.

1.1.3.5 Coherent diffractive microscopy

Coherent diffractive microscopy (usually referred to as coherent diffractive imaging) will be discussed extensively in Chapter 2. It is a computational technique that collects the scattered intensity of an incident coherent beam on a sample. The primary advantages of this approach are that it is widely applicable, provides phase and amplitude contrast, and is capable of achieving diffraction limited resolution, as it can be done without the use of lenses. However, the technique currently is not real-time; data must be acquired and then reconstructed. Furthermore, it is computationally intensive– particularly for large data sets or advanced reconstruction techniques.

1.1.4 Non light-based techniques

1.1.4.1 Electron microscopy

In the past 30 or so years, multiple microscopy techniques using electrons have revolutionized nanoimaging as well as nanofabrication. Transmission electron microscopy (TEM) and scanning electron microscopy (SEM) use beams of electrons to generate very high resolution images. This is

made possible because the deBroglie wavelength of an electron is quite small,

$$\lambda = \frac{h}{p}, \tag{1.7}$$

so for example, an electron at 30 kV has a deBroglie wavelength of 7 pm. Electron microscopes in addition can do more than just image: they can expose resist to do nano-patterning, allow the observation of material-characteristic electrons (Auger electrons) and X-rays, such as in energy dispersive X-ray spectroscopy (EDS, or EDX) techniques [29]. However, electron microscopy suffers from issues such as charging effects and hydrocarbon deposition, and the images are a mixture of material and height information [30]. Many electron microscopes and techniques are not appropriate for all samples, such as insulating samples. This is discussed further in the context of imaging buried nanostructures in Chapter 5.

1.1.4.2 Atomic force microscopy

Another widely used type of microscopy is atomic force microscopy, or AFM. This technique uses the electrostatic repulsion of a very small, thin cantilever to measure the height of a surface [11]. AFMs have proven to be an important tool for nanosurface science [31] and have are also able to do force spectroscopy, including, measuring biological forces to sub-pN precision [32].

The resolution of an AFM image depends on the size of the cantilever's tip, and additionally, material information such as the elastic modulus can be obtained [33]. However, AFMs are limited to imaging surfaces, and are very sensitive to noise and sample contamination. They can also cause damage to the sample, and are a point-scanning technique, so it takes a long time to acquire high field-of-view, high-resolution images [34].

1.2 A primer on electromagnetism and diffraction physics

The fundamentals of electromagnetism and optics span quantum mechanics, electrodynamics, and high energy physics. Here, the discussion is restricted to a classical treatment based on the wave theory of light, in the context of imaging, as this regime is valid and sufficient for the work

done in this thesis.

1.2.1 Maxwell's equations

Maxwell's equations describe the classical interaction of electromagnetic fields, and form the fundamental basis for all of optics [35],

$$\text{Gauss's Law: } \nabla \cdot \mathbf{E} = \frac{\rho}{\epsilon_0} \tag{1.8}$$

$$\text{Gauss's Law for Magnetism: } \nabla \cdot \mathbf{B} = 0 \tag{1.9}$$

$$\text{Faraday's Law: } \nabla \times \mathbf{E} = -\frac{\partial \mathbf{B}}{\partial t} \tag{1.10}$$

$$\text{Ampère's Law: } \nabla \times \mathbf{B} = \mu_0 \mathbf{J} + \mu_0 \epsilon_0 \frac{\partial \mathbf{E}}{\partial t} \tag{1.11}$$

where $\mathbf{E}$ is the electric field, $\mathbf{B}$ is the magnetic field, $\mathbf{J}$ is the displacement current, and μ_0 and ϵ_0 are the permeability and permittivity of free space respectively, such that the speed of light c is [35]

$$c = \frac{1}{\sqrt{\mu_0 \epsilon_0}} = 299\,792\,458 \text{ m/s}. \tag{1.12}$$

However, electromagnetic fields of interest are often inside a material. Then, it is important to define the material's refractive index n,

$$n = \sqrt{\frac{\epsilon \mu}{\epsilon_0 \mu_0}} \tag{1.13}$$

where μ and ϵ are the permeability and permittivity of the material, respectively, and this equation is valid in a linear, homogeneous material.

The wave equation can be derived simply from Maxwell's equations, for a system with no charges or currents such that ρ and $\mathbf{J}$ are both equal to 0. Taking the curl of both sides of Eqn. 1.10 and then substituting in Eqns. 1.11 and 1.12 (now with $\mu_0 \epsilon_0 \to \mu \epsilon$, since the following treatment will be done for waves in a medium), results in the time-dependent wave equation for an electric field,

$$\nabla^2 \mathbf{E} - \frac{n^2}{c^2} \frac{\partial^2 \mathbf{E}}{\partial t^2} = 0. \tag{1.14}$$

This equation can be partially evaluated if it is assumed that the electric field has a harmonic time dependence. For instance if $\mathbf{E}(\mathbf{r},t) = A(\mathbf{r})e^{-i\omega_0 t}$ where $A(\mathbf{r})$ is a spatially dependent amplitude and ω_0 is the angular frequency of the wave, the second term in Eqn. 1.14 can be evaluated to yield what is known as the homogeneous Helmholtz equation,

$$(\nabla^2 + n^2 k_0^2)\mathbf{E} = 0 \tag{1.15}$$

where the wavenumber is $k_0 = \omega_0/c$.

1.2.2 The Born approximation

Scattering theory is applicable to many physical problems, and forms the basis for how diffraction is commonly understood. Here, a light field scattering from an object is considered. The following derivation of the first-order Born approximation follows from [8] and [36], and assumes that this system is being treated for a monochromatic wave. The Helmholtz equation can now be written with explicit spatial dependence as

$$\nabla^2\mathbf{E}(\mathbf{r}) + k_0^2\, n^2(\mathbf{r})\, \mathbf{E}(\mathbf{r}) = 0. \tag{1.16}$$

The Laplacian operator allows the electric field vector $\mathbf{E}$ in Eqn. 1.16 to be fully decoupled into its Cartesian components. For illustrative purposes, it is simpler to consider just one of these components, E_x. Then, Eqn. 1.16 for one cartesian component can be written as

$$\nabla^2 E_x(\mathbf{r}) + k_0^2 E_x(\mathbf{r}) = -f(\mathbf{r})E_x(\mathbf{r}) \tag{1.17}$$

where the quantity $f(\mathbf{r})$ has been introduced, and is defined as

$$f(\mathbf{r}) = k_0^2\left(n^2(\mathbf{r}) - 1\right). \tag{1.18}$$

This is often called the "scattering potential" or "scattering amplitude" of the medium.

Next, an important assumption is made that there will be only one scattering event, described by one scattering potential. Then, the field at all locations can be written as the sum of the incident

field, denoted with an (i), and scattered field, denoted with an (s),

$$E_x(\mathbf{r}) = E_x^{(i)}(\mathbf{r}) + E_x^{(s)}(\mathbf{r}). \tag{1.19}$$

At this point, solving the differential equation 1.17 is difficult and the scattering potential is unknown. Fortunately, this differential equation can be transformed into an integral equation by the use of a Green's function[1] . A Green's function, $G(\mathbf{r} - \mathbf{r}')$ in this example, is an impulse response for an observation point $\mathbf{r}$ and a source point $\mathbf{r}'$.

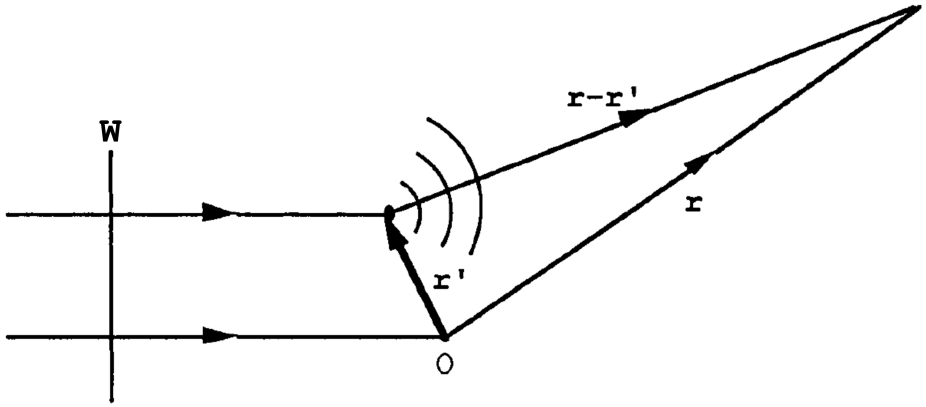

Figure 1.2: **Geometry of a scattering event**. An incoming plane wave **W** scatters from an object at a distance $\mathbf{r}'$ away from the origin O. The scattered field is observed at a distance $\mathbf{r}$ away from the origin. Figure adapted from Ref. [36].

For this case, an appropriate Green's function is the outgoing free-space Green's function of the Helmholtz operator [8],

$$G(\mathbf{r}, \mathbf{r}') = \frac{e^{ik_0|\mathbf{r}-\mathbf{r}'|}}{4\pi|\mathbf{r} - \mathbf{r}'|}. \tag{1.20}$$

Now, the wave can be written as

$$E_x(\mathbf{r}) = E_x^{(i)}(\mathbf{r}) + E_x^{(s)}(\mathbf{r}) \tag{1.21}$$

$$= E_x^{(i)}(\mathbf{r}) + \int_V d^3\mathbf{r}' \; G(\mathbf{r}, \mathbf{r}') \; f(\mathbf{r}') \; E_x(\mathbf{r}'). \tag{1.22}$$

[1] For a discussion on the use of "Green's function" versus "Green function", see the correspondence published by M.C.M. Wright, *Green function or green's function?* Nature Physics **2**, 646 (2006).

It is assumed that the scattering potential is weak such that $E^{(s)}(\mathbf{r}) \ll E^{(i)}(\mathbf{r})$, and the incident wave is a plane wave of the form,

$$E_x^{(i)}(\mathbf{r}) = e^{i\mathbf{k}_0 \cdot \mathbf{r}} \tag{1.23}$$

where $\mathbf{k}_0$ is the incident wave vector.

Now the first Born approximation can be made: because the scattering potential is weak and will scatter only once, the field in the integrand is approximately equal to the input field,

$$E_x(\mathbf{r}') \approx E_x^{(i)}(\mathbf{r}'). \tag{1.24}$$

Higher order terms may be introduced as well (adding the second term in the series is known as the second Born approximation, and so on).

Now, applying the approximation 1.24, the Green's function 1.20 and the form of the incident wave 1.23 to Eqn. 1.22,

$$E_x(\mathbf{r}) = e^{i\mathbf{k}_0 \cdot \mathbf{r}} + \int_V d^3\mathbf{r}' \; \frac{e^{ik_0|\mathbf{r}-\mathbf{r}'|}}{4\pi|\mathbf{r}-\mathbf{r}'|} f(\mathbf{r}') \; e^{i\mathbf{k}_0 \cdot \mathbf{r}'}. \tag{1.25}$$

At this point, it is convenient to change variables to momentum transfer space, such that $\mathbf{q} = \mathbf{k} - \mathbf{k}_0$, where $\mathbf{k}$ is the scattered wavevector. Furthermore, the approximation is now made that the observation point is sufficiently far away such that the extent of the source is relatively small, $|\mathbf{r}| \gg |\mathbf{r}'|$. Then, the approximation can be made that

$$k_0|\mathbf{r} - \mathbf{r}'| \approx k_0 r - \mathbf{k} \cdot \mathbf{r}' \tag{1.26}$$

for the oscillatory term in the numerator of Eqn. 1.25. A less strict approximation for the denominator of Eqn. 1.25 can be made that $|\mathbf{r} - \mathbf{r}'| \approx r$. Making these substitutions,

$$E_x(\mathbf{r}) = e^{i\mathbf{k}_0 \cdot \mathbf{r}} + \int_V d^3\mathbf{r}' \frac{e^{i(k_0 r - \mathbf{k}\cdot\mathbf{r}')}}{4\pi|\mathbf{r}-\mathbf{r}'|} \; f(\mathbf{r}') \; e^{i(\mathbf{k}\cdot\mathbf{r}' - \mathbf{q}\cdot\mathbf{r}')} \tag{1.27}$$

$$\approx e^{i\mathbf{k}_0 \cdot \mathbf{r}} + \frac{e^{ik_0 r}}{4\pi r} \int_V d^3\mathbf{r}' \; f(\mathbf{r}') \; e^{-i\mathbf{q}\cdot\mathbf{r}'}. \tag{1.28}$$

The second term on the right hand side of Eqn. 1.28, the scattered wave, can be rewritten as

$$E_x^{(s)}(\mathbf{r}) = \frac{e^{ik_0 r}}{4\pi r} \int_V d^3\mathbf{r}' \; f(\mathbf{r}') \; e^{-i\mathbf{q}\cdot\mathbf{r}'} \tag{1.29}$$

$$= \frac{e^{ikr}}{4\pi r} F(\mathbf{q}) \tag{1.30}$$

where

$$F(\mathbf{q}) = \int_V d^3\mathbf{r}' \; f(\mathbf{r}')\, e^{-i\mathbf{q}\cdot\mathbf{r}'}. \tag{1.31}$$

The quantity $F(\mathbf{q})$ is recognized as the Fourier transform of the scattering potential $f(\mathbf{r}')$. This will often be written as $F(\mathbf{q}) = \mathscr{F}\{f(\mathbf{r}')\}$, where $\mathscr{F}$ is the Fourier transform operator as discussed next.

1.2.3 The Fourier transform

As shown in the previous section, under the Born approximation a wave scattering from a potential in the far field is the Fourier transform of the scattering potential. More generally, the Fourier transform is a mathematical transformation that performs a change of basis in Hilbert space. In general, the Fourier transform can be written as

$$F(\mathbf{q}) = \int_{-\infty}^{\infty} d^3\mathbf{r}' \; f(\mathbf{r}')\, e^{-i\mathbf{q}\cdot\mathbf{r}'} = \mathscr{F}\{f(\mathbf{r}')\} \tag{1.32}$$

with the inverse function defined as

$$f(\mathbf{r}') = \int_{-\infty}^{\infty} d^3\mathbf{q} \; F(\mathbf{q})\, e^{i\mathbf{q}\cdot\mathbf{r}'} = \mathscr{F}^{-1}\{F(\mathbf{q})\}. \tag{1.33}$$

Fourier transforms are often used in imaging and other applications to transform between spaces described by conjugate variables. For example space and spatial frequency, or time and frequency.

Fourier transforms are useful in many contexts involving optics, and are often used in the mathematical propagation of light between planes. Propagation is incredibly important in computational imaging, but different situations require different approximations and treatments, which is discussed next, following from Refs [36] and [37].

1.2.3.1 The Fraunhofer and Fresnel approximations

Wave propagation is treated a number of different ways, depending on the system. For the purposes here, a good way to distinguish between different regimes is to use the Fresnel number. Using the notation of the previous section, the Fresnel number is defined as

$$F_N = \frac{r'^2}{\lambda r} \tag{1.34}$$

where r' is the diameter of the scatterer, r is the scatterer-observation point separation, and λ is the illuminating wavelength.

The Fraunhofer approximation

The approximation made to obtain Eqn. 1.26 was that the extent of the source was much smaller than the observation distance, that is, $r \gg r'$. In this regime, known as the "far-field", $F_N \ll 1$, and the Fraunhofer approximation– which states that the wave a distance z away is proportional to the the Fourier transform of the scattering potential– is valid. Since the Fourier transform is an integral, it is important to understand how to transform the coordinates. Fortunately, in the Fraunhofer regime, the transformation is simple [37]:

$$f_x = \frac{x'}{\lambda z} \tag{1.35}$$

for each spatial frequency in the one-dimensional case. For most purposes, propagation of the field $E(x', y')$ to $E(x, y)$ over a distance z under the Fraunhofer approximation can be found simply. First, the Fourier transform in terms of spatial frequency can be written,

$$\tilde{E}(f_x, f_y) = \mathscr{F}\{E(x', y')\} \tag{1.36}$$

$$f_x = \frac{x'}{\lambda z} \tag{1.37}$$

$$f_y = \frac{y'}{\lambda z}. \tag{1.38}$$

To construct the spatial coordinates (x, y), the spatial frequencies at that plane can be used. All that needs to be known are the maximum spatial frequency f_x^{Max}, and the spacing between

frequencies, df_x. Similarly, the maximum of the spatial coordinate x is x_{Max} and its spacing is dx.

$$x_{Max} = \frac{1}{df_x} \tag{1.39}$$

$$dx = \frac{1}{f_x^{Max}} \tag{1.40}$$

and similarly for y. Then, the field in spatial coordinates at both planes can be succinctly written,

$$E(x,y) = \mathscr{F}\{(E(x',y')\}|_{x'\to f_x\to x}^{y'\to f_y\to y}. \tag{1.41}$$

The Fresnel approximation

It is also important to consider what happens when the observation point is not in the far-field. When $F_N \approx 1$, known as the "Fresnel-regime", a different treatment is warranted. Approximation 1.26 is valid, but now the higher order terms in that expansion become important, and it is instructive to write the coordinates out explicitly.

Now, the source is taken to be a two-dimensional object, perhaps a screen with an arbitrary wave incident upon it, as per Huygens' principle [37]. The observation point is taken to be a two dimensional object as well, some kind of screen or detector. If the origin of the source and the origin of the detector are a distance z apart, perpendicular to the planes of the object and detector, then the distance $|\mathbf{r}-\mathbf{r}'|$ shown in Fig. 1.2 can now be written as,

$$|\mathbf{r}-\mathbf{r}'| = z\sqrt{1+\Big(\frac{x-x'}{z}\Big)^2+\Big(\frac{y-y'}{z}\Big)^2} \tag{1.42}$$

and the incident wave vector is of the form

$$\mathbf{k}_0 = k_0\hat{z} \tag{1.43}$$

shown explicitly in Fig. 1.3.

The Fresnel approximation, valid in the regime where $r'^2/\lambda \approx r$, is that it is sufficient to take the first two terms of the binomial expansion of $|\mathbf{r}-\mathbf{r}'|$ [37],

$$|\mathbf{r}-\mathbf{r}'| \approx z\left[1+\frac{1}{2}\Big(\frac{x-x'}{z}\Big)^2+\frac{1}{2}\Big(\frac{y-y'}{z}\Big)^2\right]. \tag{1.44}$$

In contrast, Eqn. 1.26 took only the first term in the binomial expansion.

Returning to the expression in Eqn. 1.25, the term $e^{i\mathbf{k}_0\cdot\mathbf{r}'}$ is now 0, as $\mathbf{k}_0$ is in the $\hat{z}$ direction and is perpendicular to $\mathbf{r}'$. The equation for the scattered wave is then,

$$E^{(s)}(x,y) = \iint_{-\infty}^{+\infty} dx'dy' \frac{e^{ik_0 z\{[1+\frac{1}{2z^2}[(x-x')^2+(y-y')^2]\}}}{z\{1+\frac{1}{2z^2}[(x-x')^2+(y-y')^2]\}} f(x',y'). \tag{1.45}$$

Next, the following expression is factored out,

$$e^{\frac{ik}{2z}(x^2+y^2)} \tag{1.46}$$

so that the Eqn. 1.45 becomes

$$E^{(s)}(x,y) = \frac{e^{ik_0 z}}{z} e^{\frac{ik_0}{2z}(x^2+y^2)} \iint_{-\infty}^{+\infty} dx'dy' \frac{e^{-\frac{ik_0}{2z}(x'^2+y'^2)} e^{\frac{ik_0}{z}(xx'+yy')}}{1+\frac{1}{2z^2}[(x-x')^2+(y-y')^2]} f(x',y'). \tag{1.47}$$

The oscillatory term is the numerator is important, but in the denominator, it is appropriate to again use the approximation $|\mathbf{r}-\mathbf{r}'| \approx r$, so that the second term is small and can be neglected.

An important approximation in optics, the paraxial approximation, states that the location being observed on the detector is fairly close to the origin. That is, the angle θ in Fig. 1.4 is small. More explicitly,

$$z \gg \sqrt{x^2+y^2}. \tag{1.48}$$

This means that the denominator will be small, so that the final expression is

$$E^{(s)}(x,y) = \frac{e^{ik_0 z}}{z} e^{\frac{ik_0}{2z}(x^2+y^2)} \iint_{-\infty}^{+\infty} dx'dy' e^{-\frac{ik_0}{2z}(x'^2+y'^2)} \left[e^{\frac{ik_0}{z}(xx'+yy')} f(x',y') \right]. \tag{1.49}$$

This equation is recognized as containing the Fourier transform as in Eqn. 1.31. The difference here is that the input field, $f(x,y)$, must first be multiplied by a quadratic phase factor. Eqn. 1.49 is known as the Fresnel diffraction integral [37].

In terms of the Fourier transform operator, the Fresnel diffraction integral can be written as

$$E^{(s)}(x,y) = \frac{e^{ik_0 z}}{z} e^{\frac{ik_0}{2z}(x^2+y^2)} \mathscr{F}\left\{ e^{-\frac{ik_0}{2z}(x'^2+y'^2)} f(x',y') \right\}. \tag{1.50}$$

As expected, in the limit $z \gg k_0(x'^2+y'^2)$, the quadratic phase term is negligable and the simple far-field Fourier transform is recovered.

1.2.3.2 Spectrum of plane waves propagation

While wave propagation to the far and mid-field have been treated, it is now important to understand propagation very close to- perhaps even within- the scattering potential. The spectrum of plane waves approach is indeed valid everywhere, but if numerically propagating a significant distance using the fast Fourier transform (FFT) routine, a new spatial frequency grid may need to be calculated. Thus, this approach is convenient for treating diffraction over very small distances.

Returning to the Helmholtz equation (Eqn. 1.15),

$$0 = (\nabla^2 + n^2 k_0^2)\, E(\mathbf{r}) \tag{1.51}$$

$$= (\frac{\partial^2}{\partial x^2} + \frac{\partial^2}{\partial y^2} + \frac{\partial^2}{\partial z^2} + n^2 k_0^2) E(\mathbf{r}) \tag{1.52}$$

a method by which to solve this differential equation is by taking the two dimensional Fourier transform, from $(x, y) \rightarrow (k_x, k_y)$ in order to be consistent with the k_0 in the Helmholtz equation. Under the paraxial approximation, it is assumed that the input and detected field are well-defined at planes, such that the fields themselves do not depend on z.

$$\mathscr{F}\{(\nabla^2 + n^2 k_0^2)\, E(x, y; z)\} = \iint_{-\infty}^{+\infty} dx\, dy\, (\frac{\partial^2}{\partial x^2} + \frac{\partial^2}{\partial y^2} + \frac{\partial^2}{\partial z^2} + n^2 k_0^2)\, E(x, y, z) \tag{1.53}$$

$$= \left((ik_x)^2 + (ik_y)^2 + \frac{\partial^2}{\partial z^2} + n^2 k_0^2\right) \tilde{E}(k_x, k_y, z) \tag{1.54}$$

$$= (-k_x^2 - k_y^2 + \frac{\partial^2}{\partial z^2} + n^2 k_0^2)\, \tilde{E}(k_x, k_y, z). \tag{1.55}$$

The solution to the differential equation 1.55 assuming only forward scattering and no backwards scattering is,

$$\tilde{E}(k_x, k_y, z) = Ce^{ik_z z} \tag{1.56}$$

where C is a constant and

$$k_z = \sqrt{n^2 k_0^2 - k_x^2 - k_y^2}. \tag{1.57}$$

To choose the constant C, a boundary condition must be applied. At $z = 0$, the field has not propagated any distance, therefore is unchanged. Then,

$$C = \tilde{E}(k_x, k_y, 0) \tag{1.58}$$

so that final equation for the spectrum of plane waves propagation is

$$E(x,y,z) = \mathscr{F}^{-1}\Big\{\tilde{E}(k_x,k_y,0)e^{iz\sqrt{n^2k_0^2-k_x^2-k_y^2}}\Big\}. \tag{1.59}$$

1.2.4 The Ewald sphere and numerical aperture

As mentioned in the treatment of the Born approximation, in an elastic scattering event energy is conserved and therefore for a single scattering event, there will be a surface of possible momentum transfer. In three-dimensional space this surface is known as the Ewald sphere.

In the case where $\mathbf{k}_0 = k_0\hat{z}$. The scattered k-vector in spherical coordinates is then $\mathbf{k} = k_0\,(sin(\phi)\,sin(\theta)\hat{x} + sin(\phi)\,cos(\theta)\hat{y} + cos(\phi)\hat{z})$. The momentum transfer $\mathbf{q} = \mathbf{k} - \mathbf{k}_0$ in each direction is then,

$$q_x = k_0\,sin(\phi)\,sin(\theta) \tag{1.60}$$

$$q_y = k_0\,sin(\phi)\,cos(\theta) \tag{1.61}$$

$$q_z = k_0\,cos(\phi) - k_0 \tag{1.62}$$

where as before, the wavevector k_0 is proportional to $1/\lambda_0$. It can be seen then that the radius of the Ewald sphere is determined by the wavelength of the scattering light, and photons of different wavelength will produce Ewald spheres of different radii.

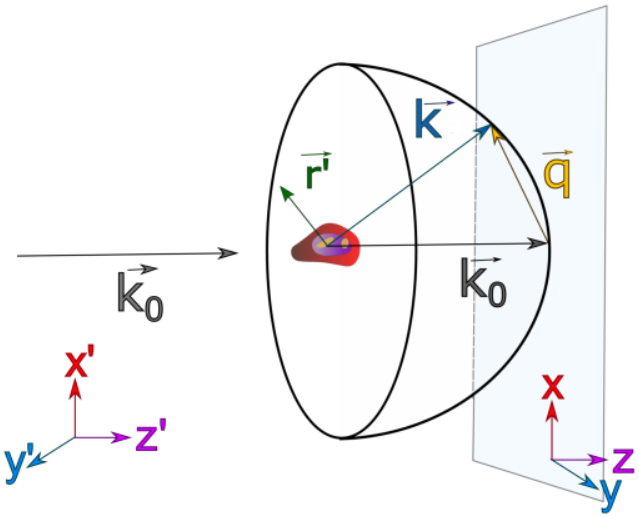

Figure 1.3: **Schematic of the Ewald sphere showing a forward scattering event**. The scattered momentum **k** traces out a variety of angles. The length of **k** is the radius of the Ewald sphere.

Figs. 1.3 and 1.4 show that there is a relationship between the Ewald sphere and numerical aperture (NA). In fact, the numerical aperture can be thought of as relating to the solid angle of the Ewald sphere that is captured on the detector. As the information at high angle corresponds to high spatial frequency, it is intuitive that higher resolution results from capturing scatter at higher angles. In certain imaging systems, the numerical aperture is limited by an optical element like a lens or pinhole. For the scattering event shown here, as well as in lensless imaging techniques, the NA is limited only by the size of the detector and its distance away from the sample.

For a lensless system with a detector of width $2d$ and an object-detector separation z, the NA is defined as,

$$NA = sin\theta = \left(\frac{d}{\sqrt{d^2 + z^2}} \right). \tag{1.63}$$

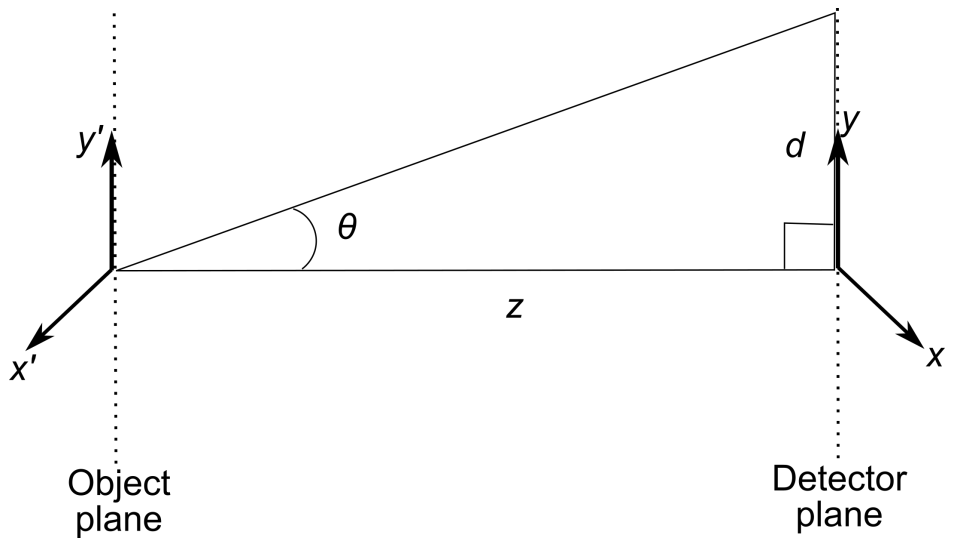

Figure 1.4: **Numerical aperture of a lensless system**. Schematic showing the numerical aperture (NA) of a system defined by detector of half width d and object-detector separation z.

1.2.4.1 Curvature correction and tilted plane correction

As seen in Fig. 1.3, it is clear that at very high NA, it is no longer accurate to describe the wave in only two dimensions. Curvature in the Ewald sphere is necessarily non-paraxial. Experimentally, this means that measuring the diffraction pattern on a two-dimensional detector will result in distortions at high spatial frequencies, due to the three-dimensional Ewald sphere being projected onto a two-dimensional surface.

Further complications arise at non-normal incidence, where not only is the Ewald sphere projection distortion present, but a phenomenon known as conical diffraction occurs as well, where the diffraction pattern is asymmetrically distorted due to the angle of incidence. A distorted diffraction pattern is shown in Fig. 1.6(a). This phenomenon is discussed further below.

In reflection geometry, the Ewald sphere will be flipped along the z direction relative to the input wavevector (at normal incidence), pictured in Fig. 1.5.

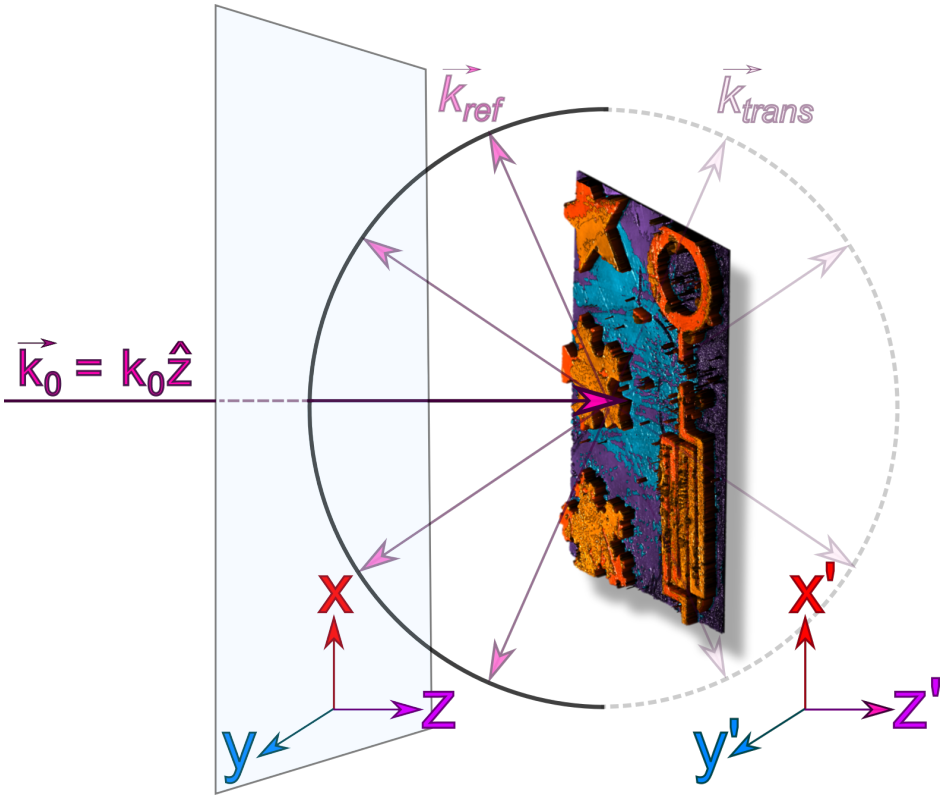

Figure 1.5: **Schematic showing the Ewald sphere in reflection geometry**. Light scattered backward is shown along the reflected Ewald sphere $\mathbf{k}_{ref}$, and forward scattered light (if the object were partially transmissive) is shown as the forward-scattered Ewald sphere along $\mathbf{k}_{trans}$.

Both the symmetric normal incidence and the asymmetric non-normal incidence distortions pose problems. The FFT routine assumes a linearly spaced spatial frequency grid. Fortunately, the nonlinear spatial frequency grid can be calculated using knowledge of the sample angle, sample-detector distance, and wavelength. The nonlinear spatial frequency grid can then be interpolated back to a linear spatial frequency grid using a technique called tilted plane correction (TPC) [38,39], which allows the FFT routine to be used.

Fig. 1.6 shows diffraction data before and after TPC. The correction re-maps the spatial frequencies back onto a linear grid, allowing FFT routines to be used and a uniform pixel size in each dimension in the reconstructed sample.

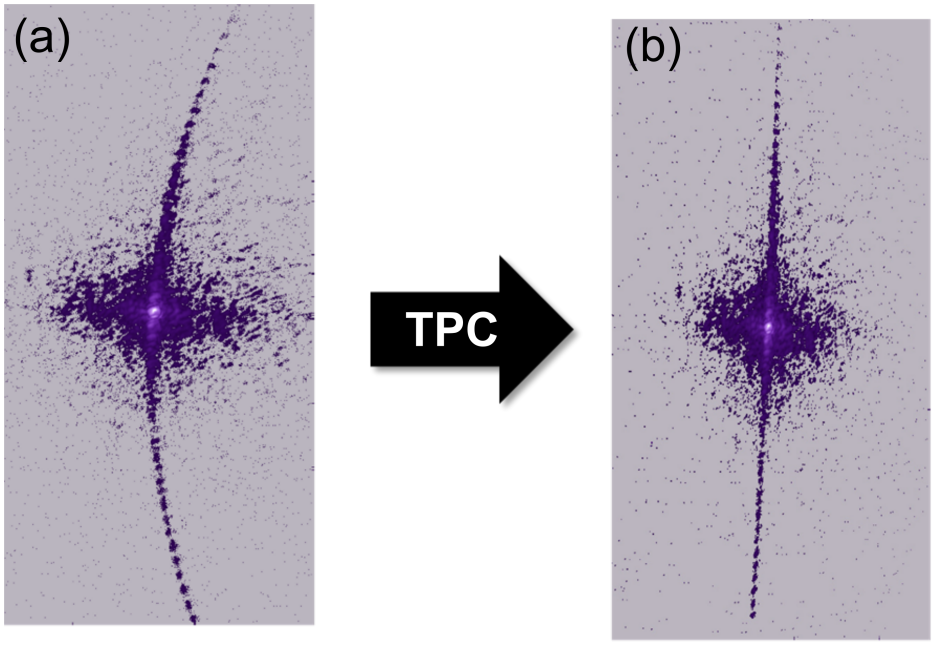

Figure 1.6: **Example of tilted plane correction**. Diffraction pattern before and after tilted plane correction for a pattern distorted by conical diffraction at approximately 45°, (a) before and (b) after tilted plane correction (TPC). Figure adapted from Ref. [40].

1.3 EUV and X-ray microscopy

A significant challenge of imaging in the EUV/X-ray is that there are limited suitable optics. One advantage of short wavelength light is its penetrating power, but this also means that there are essentially no materials that can form an appropriate refractive lens. Diffractive and reflective optics can be used, some of which are shown in Fig. 1.7, as can lensless techniques, which will be discussed extensively in the next chapter.

1.3.1 Refractive index

For visible wavelengths, the refractive index can often be estimated as the ratio of the speed of light in vacuum and the speed of light in the material,

$$n = \frac{c}{v}. \tag{1.64}$$

This model is good for certain materials and wavelengths, but fails to account for the fact that the refractive index depends upon the wavelength of light in question- which becomes very important in the EUV.

To understand how refractive indices are modeled in the EUV/X-ray regime, first consider the building blocks: the atomic scattering factors f_1 and f_2. These numbers are wavelength-dependent constants of the elements for a given isotope, and describe the refraction and absorption of electromagnetic radiation.

The refractive index can be constructed from the atomic scattering factors, and the density of the material, in the following way [41],

$$n(\lambda) = 1 - \delta - i\beta \tag{1.65}$$

where

$$\delta(\lambda) = \frac{n_a r_e \lambda^2}{2\pi} f_1(\lambda) \tag{1.66}$$

$$\beta(\lambda) = \frac{n_a r_e \lambda^2}{2\pi} f_2(\lambda) \tag{1.67}$$

where n_a is the atomic number density (that is, the number of atoms per unit volume) r_e is the classical electron radius, and λ is the wavelength. Avogadro's number and the atomic mass of an element can be used to go between bulk density and atomic number density. The atomic scattering factors are available in databases such as CXRO [42]. For most materials, the refractive index in the EUV/X-ray region will be close to 1 (except near absorption edges). This is why it is difficult to manufacture focusing optics in the EUV spectral region.

1.3.2 Focusing and imaging techniques

Due to the refractive indices in the EUV/X-ray being close to 1, and because many materials are highly absorbing in the EUV, fabricating refractive focusing and image-forming optics is a challenge in this region of the electromagnetic spectrum.

Diffraction-based optics, such as Fresnel zone plates, shown in Fig. 1.7(a) [43], are often implemented, but they are not high-efficiency and their fabrication quality limits the resolution of

the image. Schwartzchild objectives (Fig. 1.7(b)) can focus light, but due to the geometry cut out flux in the middle of the beam. Furthermore, they need to be coated in order to be reflective, and reflectivity, even with coatings, is generally poor near normal incidence in the EUV/X-ray. Imaging with Kirkpatrick-Baez mirrors (Fig. 1.7(c)), which are curved mirrors that focus the beam in two dimensions separately has been done [44], but there are problems with aberrations and resolution. However, this focusing geometry is still often used in synchrotrons and free electron lasers. Another option is a Laue lens, which uses multilayer coatings and different periods to focus the light, shown in Fig. 1.7(d).

As for image-forming methods using these optics, one method is transmission X-ray microscopy (TXM), which uses a zone plate or other optic to form a full-field image on a detector, shown in Fig. 1.7(e). Scanning transmission X-ray microscopy (STXM) is a method using zone plates that focuses an X-ray beam to a small point and scans the sample, building up a point-by-point image [45], shown in Fig. 1.7(f).

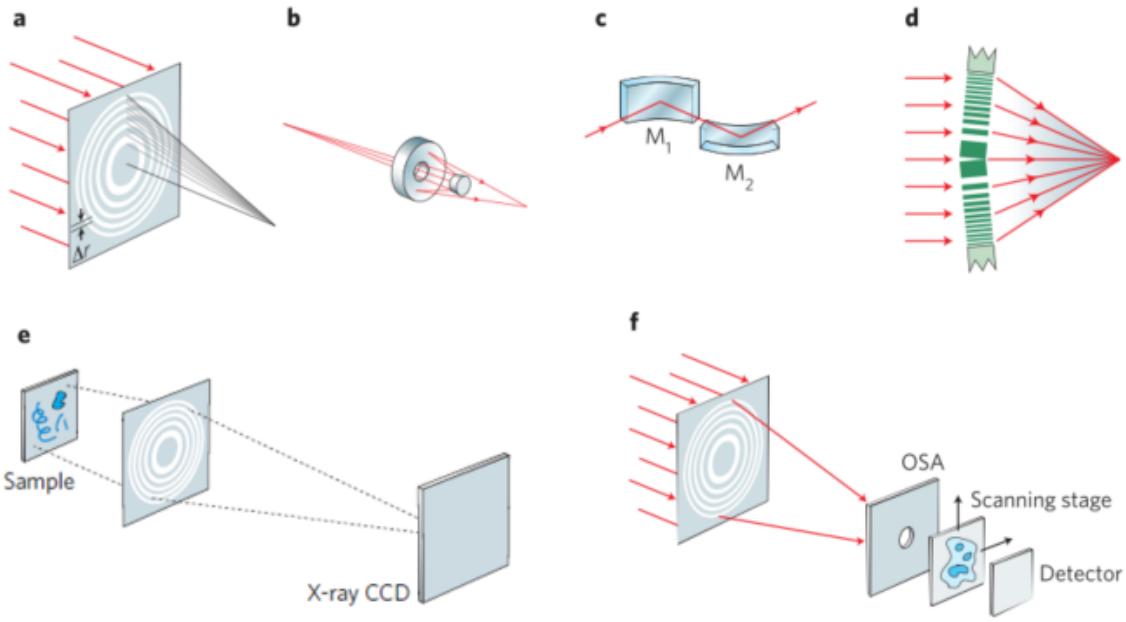

Figure 1.7: **X-ray imaging and optics**. (a) Fresnel zone plate, a diffractive optic capable of focusing light. (b) Schwartzchild objective, a reflective optic which focuses light. (c) Kirkpatrick-Baez mirrors, used to focus the beam in two directions at glancing incidence. (d) Laue lens with multilayer coatings. Different periods are formed and able to focus the light. (e) Experimental set-up for transmission X-ray microscopy using a Fresnel zone plate. (f) Scanning transmission X-ray microscopy (STXM), where the beam is focused, filtered by an order sorting aperture, and then the sample is raster scanned across the beam. Figure adapted from Ref. [46]

.

Coherent methods, such as Fourier transform holography [47], can be used as well, but these methods require a suitable size and location of reference hole, and there is a trade-off between image resolution and the signal-to-noise ratio in the hologram.

While each of these techniques is appropriate for certain systems, the work described in this thesis uses a general lensless method known as coherent diffractive imaging (CDI). CDI has many advantages; in particular it is able to achieve phase and amplitude contrast, and because there are no intervening optics between the sample and the detector it can provide diffraction-limited resolution, where only the size of the detector, object-detector separation, and illuminating wavelength limit the resolution of the image. Using image-forming optics generally requires fabrication for a specific wavelength, and the optics can introduce aberrations in the image. CDI is discussed in detail in

the next chapter.

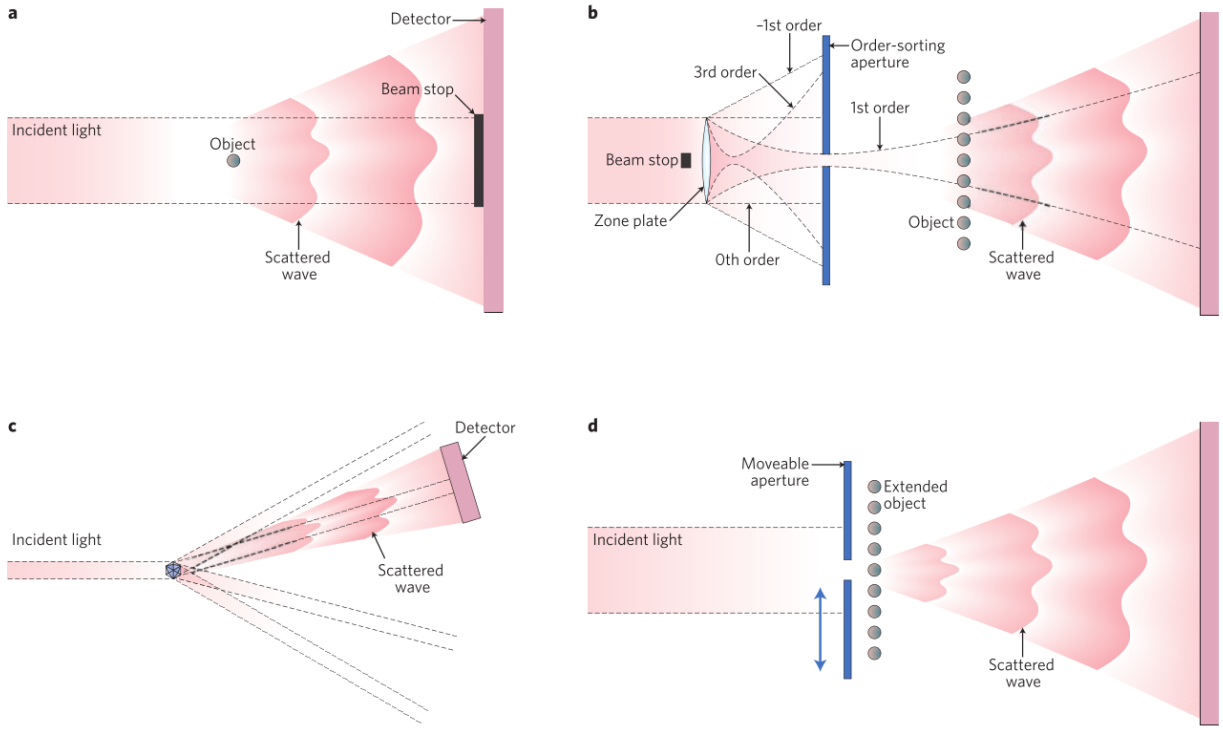

Figure 1.8: **Different experimental setups for lensless CDI**. (a) Plane-wave CDI uses coherent plane waves. (b) Fresnel CDI uses zone plates or other optics to focus the beam onto the sample. An aperture and beam stop let through the first order diffracted light and blocks the other, unwanted orders. (c) Bragg CDI investigates crystalline structures by rocking the sample at different angles and observing shifts in the Bragg peaks. (d) Scanning diffraction microscopy scans an aperture across the beam and observes the diffraction from small spots within a sample. Figure adapted from Ref. [48].

Chapter 2

Coherent Diffractive Imaging and Ptychography

2.1 Introduction

Coherent diffractive imaging (CDI) is a promising imaging technique that can be used without lenses– making it an excellent choice for EUV/X-ray imaging, as there are limited image-forming optics for short-wavelength illumination. CDI utilizes phase retrieval; a computational technique capable of reconstructing the amplitude and phase of an object based on constraints in the system. Due to its capability for high-resolution, phase-contrast imaging, CDI is the method used for the EUV/X-ray microscopy performed in this thesis. This chapter will discuss the motivation behind CDI and phase retrieval, as well as the description of some common techniques.

2.2 Phase retrieval and isolated-object CDI

2.2.1 The phase problem

Phase information is incredibly important for a variety of applications. Understanding a nanosystem's topographical structure, chemical composition, and thickness all heavily depend on information learned from the phase of the exit surface wave (ESW), which is the two-dimensional wave leaving an object. Phase contrast is also important for many biological applications, which may have poor amplitude contrast to visible wavelengths. However, measuring phase is often difficult.

While light intensity is collected on detectors such as photographic paper, charge coupled

devices (CCDs) and the human eye, the phase is lost. This is known as *the phase problem*, and can be understood simply by considering a complex wave $\psi = Ae^{i\phi}$, where A is the amplitude and ϕ is the phase, and A and ϕ are both real numbers. Intensity-sensitive detectors will measure the following field:

$$I = |\psi|^2 = \psi\psi^* = Ae^{i\phi}Ae^{-i\phi} = A^2. \tag{2.1}$$

Hence, the phase is lost, and only the intensity (which is the square of the amplitude) is recorded.

If a detector could be built to directly measure the phase of light at high frequencies, then phase contrast techniques would not be necessary. However this is currently an intractable engineering problem: such a detector would need an electronic response time faster than current technology allows. For instance, the phase of visible light oscillates on the order of 10^{14} Hz, and currently even the fastest electronic detectors have response frequencies of less than 10^{12} Hz.

2.2.2 Phase retrieval

Phase retrieval has been developed over the past 60 years to allow the lost phase of an image to be computationally reconstructed by imposing a few constraints on the imaging system [49–51]. It has a number of advantages over other phase-contrast techniques [52]. For instance, it does not require interferometric scanning or a reference beam. CDI, a technique which uses phase retrieval, returns quantitative, physical contrast images, which can be used to determine materials present in the sample [53]. This makes CDI an excellent tool for more fully characterizing a system through imaging.

An important aspect of many phase retrieval systems is that the data recorded is a far-field diffraction pattern, and is proportional to the Fourier transform. This nominally requires that a beam be coherent and monochromatic, although exceptions to these requirements are possible and will be discussed later in this chapter and in Chapter 4. For such a beam, in the far-field ($F_N \ll 1$), the diffraction pattern is related to the Fourier transform by a simple scaling, which can be obtained based on known experimental parameters. Another requirement on the system is that the data in Fourier space be properly sampled, which is an important consideration when recording any signal.

Phase retrieval was first described by David Sayre in 1952 [3], who noted that the phase of an image could be retrieved with a properly sampled diffraction pattern, based on earlier work by Shannon utilizing the Nyquist sampling theorem. This idea was developed further by Gerchberg and Saxon [54], who introduced the error reduction algorithm and the idea of using the Fourier transform to iterate between image and diffraction space.

2.2.2.1 Gerchberg-Saxon and generalized projection algorithms

Gerchberg-Saxon (GS) phase retrieval is a type of generalized projection algorithm that uses two constraint sets, the support constraint S and the amplitude constraint A [54]. To better understand the GS algorithm, it is helpful to first understand the spaces and sets involved.

Consider a Hilbert space that consists of all possible solutions for a complex image of a given size. The support constraint set S is the set of all functions that satisfy the support constraint, and the amplitude constraint set A is the set of all functions which satisfy the amplitude constraint. Then, the GS algorithm consists of projections between these two sets, which intersect at one nontrivial point. This is illustrated in Fig. 2.1.

Generally, in the GS algorithm the support constraint is performed in object space while the amplitude constraint is performed in Fourier space. The support of a function is the set of all points in the function that are non-zero, so the support constraint sets all of the points outside of a small isolated region, usually in the object's center, equal 0– thus enforcing a particular support. The support constraint, though in image space, enforces oversampling in Fourier space and reduces the number of unknowns in the system. This is discussed more in the following section.

The amplitude constraint, which requires that the guess for the diffraction pattern be consistent with the measured intensity, is enforced in Fourier space. This also reduces the number of unknowns in the system, as the measured intensity data is usually considered to be known. The Fourier transform is used to go between these two spaces.

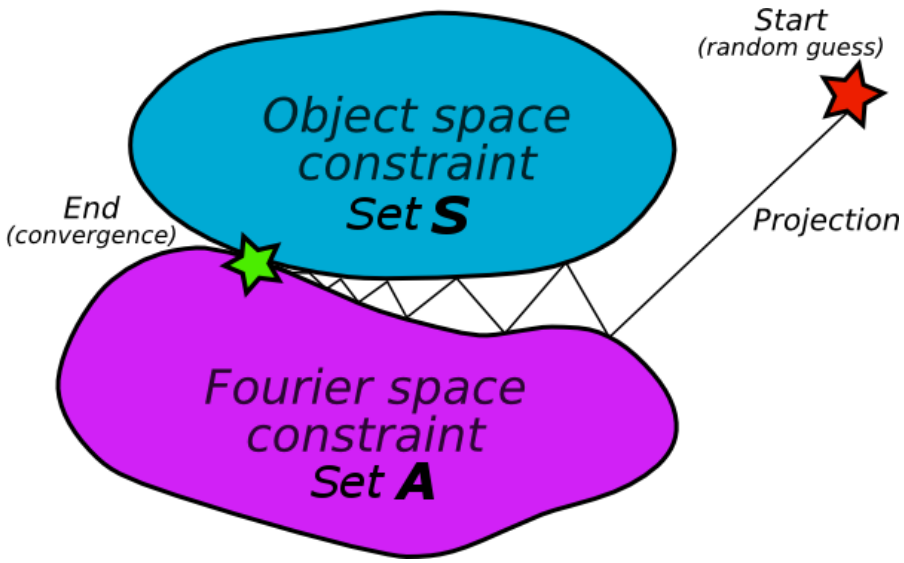

Figure 2.1: **Sets in Gerchberg-Saxon phase retrieval**. Set-space diagram of a generalized projection algorithm, in this case the Gerchberg-Saxon algorithm is illustrated. S and A are subsets of Hilbert space.

The isolation constraint can also be understood from the point of view of unknowns versus knowns in the measurement. Consider a two-dimensional case with a detector consisting of $N \times N$ pixels. Since the wave is complex, there are a total of $2N^2$ unknowns. The corresponding object will also have $N \times N$ complex points and $2N^2$ unknowns. The measured intensity on the detector gives N^2 knowns, so now the detector plane has the same number of knowns and unknowns. In the object domain, the isolation or support constraint demands that part of the object is known, and one way this is achieved is by setting some of the object in each dimension equal to 0. Now, to have the same number of knowns and unknowns in the object domain, the region that is unknown is restricted to $N/\sqrt{2} \times N/\sqrt{2}$, so there are now $N^2/2$ unknowns in the amplitude and phase of the object, with the rest being set to 0. This assures that the intensity on the detector is Nyquist sampled, and makes the number of knowns and unknowns in the object domain both equal to N^2. The entire system now has the same number of knowns and unknowns, and a unique solution may be obtained.

2.2.3 Sampling and the isolation constraint

As mentioned previously, properly sampling the diffraction pattern is paramount to the ability to do phase retrieval. Though this constraint might seem easily satisfied, it is actually not so. It restricts the objects to a subset that are isolated, which often means using a pinhole-like sample, or imaging a pinhole onto the sample, which can be experimentally challenging and cumbersome.

The Nyquist-Shannon sampling theorem states that the sampling frequency must be at least twice the highest frequency of the waveform being sampled [55]. Indeed, spatial frequencies are no exception, and therefore the diffraction pattern must be sampled properly on the detector to ensure image convergence.

As shown in Eqn. 1.35, in the object domain with spatial coordinates x' and y', the spatial frequencies in the Fourier domain (under the paraxial approximation) are

$$f_x = \frac{x'}{\lambda z} \tag{2.2}$$

$$f_y = \frac{y'}{\lambda z}. \tag{2.3}$$

Now, consider the spatial frequency on the detector as $1/p$, where p is the pixel size, then the oversampling of the system can be derived based on the highest possible sampling rate (pixel size) from the object and that of the detector.

Taking the maximum extent of the object D, the largest spatial frequency on the detector is equal to $\frac{D}{\lambda z}$ from Eqn. 2.2. Hence, one can define the *oversampling ratio*, σ, as the ratio of the maximum object and detector sampling frequencies in the same domain:

$$\sigma = \frac{s_{detector}}{s_{object}} \tag{2.4}$$

$$= \frac{\lambda z}{pD} \tag{2.5}$$

As per the Nyquist-Shannon theorem, this sampling rate must be at least equal to 2. Keeping in mind that the diffraction-limited resolution of an imaging system is $\lambda/(2NA)$, where the NA is

inversely proportional to z, it is apparent that there is a trade-off between the resolution of the system and its oversampling.

2.3 Isolated-object phase retrieval algorithms

In 1978, Fienup demonstrated 2D phase retrieval using an iterative algorithm [56] and since then it has continued to be a popular technique [57]. In the X-ray regime, phase retrieval was demonstrated in 1999 by Robinson [58] and Miao [59]. Since then, it has been used and developed for a wide variety of applications from visible light all the way to the hard X-ray [60, 61]. Many algorithmic advances have been made along the way. For instance, the shrinkwrap algorithm allows the support to shrink to a small shape around the object [51]. A smaller support effectively reduces the number of unknowns in the system. Other algorithmic advances have made CDI faster, more general, and robust to noise and ambiguities [62–66].

There are many different phase retrieval algorithms for performing CDI on an isolated object (ioCDI). They range in complexity, and it is instructive to mention a few here.

The simplest GS phase retrieval is the error-reduction (ER) algorithm. Defining the support constraint set S, for a guess of the complex object in image space $g(\mathbf{r})$, updated guess $g'(\mathbf{r})$ on iteration k, the ER algorithm amounts to the following real-space constraints;

$$g_{k+1}(\mathbf{r}) = g'_k(r);\ \mathbf{r} \in S \tag{2.6}$$

$$g_{k+1}(\mathbf{r}) = 0;\ \mathbf{r} \in (1 - S). \tag{2.7}$$

However, this algorithm can sometimes get stuck in local minima, such as a super-position of the image and its inversion- known as the twin-image problem- which are ambiguous solutions. Variations on the ER algorithm can help free it from stagnation in local minima, one such variation is known as the Hybrid input-output (HIO) algorithm [57],

$$g_{k+1}(\mathbf{r}) = g'_k(\mathbf{r});\ \mathbf{r} \in S \tag{2.8}$$

$$g_{k+1}(\mathbf{r}) = g_k(\mathbf{r}) - \beta g'_k(\mathbf{r});\ \mathbf{r} \in (1 - S) \tag{2.9}$$

where β is a relaxation parameter. Another variation is the relaxed averaged alternating reflections (RAAR) algorithm [67],

$$g_{k+1}(\mathbf{r}) = g'_k(\mathbf{r}) \ \mathbf{r} \in S \tag{2.10}$$

$$g_{k+1}(\mathbf{r}) = \beta g(\mathbf{r}) + (1-2\beta) - g'(\mathbf{r}); \ \mathbf{r} \in (1-S). \tag{2.11}$$

2.3.1 EUV/X-ray isolated object CDI

After CDI was first demonstrated with X-rays in 1999 [58, 59], its use at synchrotrons continued [50, 68] with many improvements in algorithms and applications to a variety of samples [43, 45, 51, 63, 69–73]. X-ray CDI proven to be an important tool for biological applications as well [74–76]. Tabletop EUV CDI was first demonstrated in 2007 [47]. In 2011, 22 nm resolution was achieved using a 13 nm source [52], which at the time was the highest resolution of any light-based tabletop microscope. The technique was further advanced with a combination of in-line holography in and keyhole CDI in 2013 [77].

These tremendous improvements in imaging were of incredible importance. However, they were restricted to isolated, two-dimensional samples. Keyhole CDI provided an opportunity for imaging wider fields of view and extended samples [78], but with several limitations on the beam. With the advent of ptychography, discussed in the next section, CDI was no longer limited to isolated systems, did not require fully characterized beams, and could achieve large fields of view with a very robust approach.

2.4 Ptychography CDI

A powerful new CDI technique known as ptychography CDI [79], has emerged fairly recently [80, 81]. In ptychography CDI, the beam and sample are scanned relative to each other, and diffraction is collected from fields-of-view with a strong degree of overlap ($> 70\%$ of the area of the beam). This introduces a high degree of information redundancy into the algorithm, making it much more robust.

2.4.1 The ptychography algorithm

The ptychography algorithm is a gradient-descent method that blindly deconvolves the object and illuminating beam (or "probe"). The algorithm is as follows, as described by Maiden et al. [81].

At a given position j, the spatial object $O(\mathbf{r})$ and probe $P(\mathbf{r})$ are multiplied together to form the exit surface wave (ESW) $\psi_j(\mathbf{r})$;

$$\psi_j(\mathbf{r}) = O_j(\mathbf{r})P(\mathbf{r} - \mathbf{R}_j). \tag{2.12}$$

This form of the exit surface wave is valid under the projection approximation, which assumes that the object is thin enough that the ESW can be approximated as a multiplication of a 2D wave (in this case, the probe) by a 2D transmission function (in this case, the object). The projection approximation is discussed further in Chapter 6.

In Eqn. 2.12, $\mathbf{R}_j$ is the relative shift of the probe at the j^{th} position. The ESW is then Fourier transformed to obtain the guess for the diffraction pattern,

$$\Psi_j(\mathbf{u}) = \mathscr{F}\{\psi_j(\mathbf{r})\} = A_j(\mathbf{u})e^{i\phi_j(\mathbf{u})}. \tag{2.13}$$

Here, $\mathscr{F}$ is the Fourier transform operator and $\mathbf{u}$ is the spatial frequency coordinate vector. Next, the amplitude constraint is applied, where the square root of the measured intensity of the diffraction pattern replaces the guess for the amplitude of the diffraction pattern. For the measured intensity $I_j(\mathbf{u})$, corresponding to the diffraction pattern from the j^{th} position,

$$\Psi'_j(\mathbf{u}) = \sqrt{I_j(\mathbf{u})}e^{i\phi_j(\mathbf{u})}. \tag{2.14}$$

At this step, it is convenient to define and calculate the error metric, which is typically the RMS difference of the known amplitude $\sqrt{I_j(\mathbf{u})}$ and the algorithm's guess for the amplitude, $A_j(\mathbf{u})$. Next, by returning to object space via the inverse Fourier transform, an updated exit surface wave is obtained,

$$\psi'_j(\mathbf{r}) = \mathscr{F}^{-1}\{\Psi'_j(\mathbf{u})\}. \tag{2.15}$$

Finally, the guesses for the object and probe are updated to become $O'_j(\mathbf{r})$ and $P'_j(\mathbf{r})$. This is achieved using a combination of probe and object information, as well as the difference between the updated and non-updated ESW:

$$O'_j(\mathbf{r}) = O_j(\mathbf{r}) + \alpha \frac{P_j^*(\mathbf{r} - \mathbf{R}_j)}{|P_j(\mathbf{r} - \mathbf{R}_j)|^2_{max}} \big(\psi'_j(\mathbf{r}) - \psi_j(\mathbf{r})\big) \tag{2.16}$$

$$P'_j(\mathbf{r}) = P_j(\mathbf{r}) + \alpha \frac{O_j^*(\mathbf{r} + \mathbf{R}_j)}{|O_j(\mathbf{r} + \mathbf{R}_j)|^2_{max}} \big(\psi'_j(\mathbf{r}) - \psi_j(\mathbf{r})\big) \tag{2.17}$$

where α and β are weighting factors, and the superscript $*$ denotes a complex conjugate.

2.4.2 Improvements and variations on ptychography

Many variations on and improvements to ptychography have been developed. Algorithmic improvements that correct errors in the position due to stage errors or uncertainty in wavelength or pixel size [82] have been demonstrated. Ptychography has also been extended to allow simultaneous reconstruction of mutually incoherent modes [83–85], improve the guess for the probe [86], upsample undersampled data [87], and achieve super resolution [88] have been demonstrated. Ptychography has also been applied to non-imaging problems, such as pulse characterization using the FROG algorithm [89]. Some of these improvements are discussed further in Chapter 4.

Chapter 3

Coherent EUV/X-ray Light Sources

3.1 Introduction to X-ray Sources

The previous chapter discussed the advantages and capabilities of coherent diffractive imaging. CDI is predicated on having coherent (or partially coherent) light. Abbe's diffraction limit (Eqn. 1.5) indicates that smaller wavelengths can resolve smaller features. For this reason, the development of coherent short-wavelength sources allows microscopes to combine the robustness and power of CDI while taking advantage of the high resolution and chemical specificity of EUV and X-ray radiation. This chapter discusses various sources of coherent EUV and X-ray light and the process of High Harmonic Generation (HHG); the coherent source with which the work done in this thesis was done.

While many microscopy techniques utilize incoherent light, such as those discussed in Chapter 1, coherent imaging techniques have become increasingly important since the prediction and demonstration of the laser by Schawlow, Townes, and Maiman nearly 60 years ago [90]. In particular, coherent light is useful for various phase-contrast and interferometric imaging techniques, as discussed in Chapters 1 and 2. An excellent probe of the nano-world is EUV and X-ray light, due to its short wavelength, many absorption edges (shown in Fig. 3.1), and strong penetrating power. Furthermore, if the source is ultrafast, this provides access to temporal dynamic information.

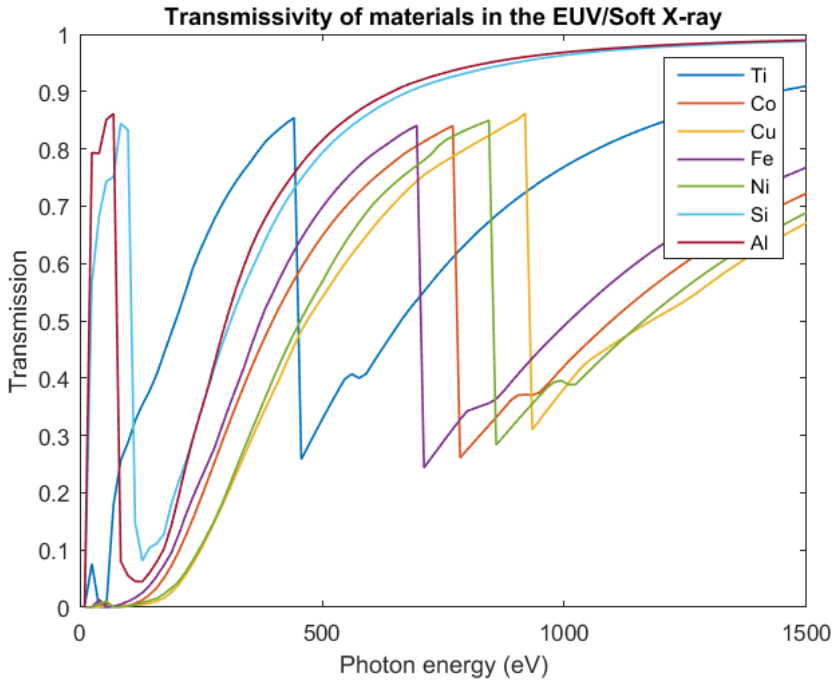

Figure 3.1: **Transmissivity of different materials in the EUV/Soft X-ray**. Transmission versus photon energy from the EUV to soft X-ray for different 100 nm-thick materials [42].

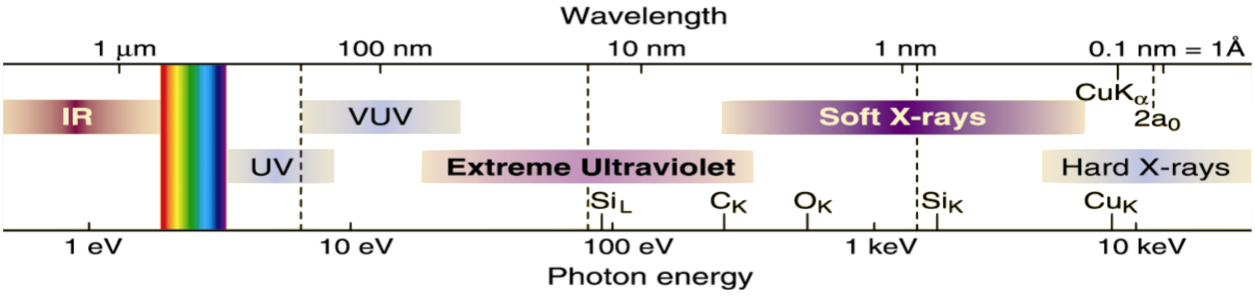

Figure 3.2: **Wavelengths and photon energies of different types of radiation**. Spectral ranges of IR, visible, UV, VUV, EUV, soft X-ray, and hard X-ray radiation. Figure adapted from Ref. [41].

Fig. 3.2 shows where the different spectra fall with respect to wavelength and energy, as well as some important absorption lines.

This chapter contains a brief discussion of incoherent X-ray light, followed by discussions of coherent EUV/X-ray light sources: facility-scale sources; synchrotrons and free electron lasers, and then tabletop sources; plasma discharge lasers and high harmonic generation (HHG). Since HHG

is the process used to produce the light used in this thesis, it will be discussed in more detail.

3.1.1 Incoherent X-ray light

Incoherent X-ray light was first demonstrated by Röntgen in 1895. It was produced in a vacuum tube by Bremsstrallung; a process by which electrons or other particles are slowed down (for instance, by hitting a thick target), and release high energy photons in the process [35]. Since then, X-ray light has become an essential tool in the medical field in the form of CT scans, radiographic X-rays, and other diagnostic and therapeutic tools [91]. This was the only form of X-ray light for about 50 years, until synchrotrons were developed in the late 1940's/early 1950's [92, 93].

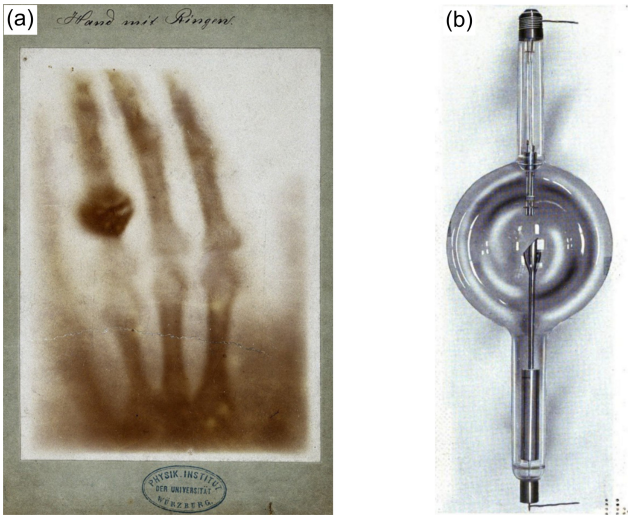

Figure 3.3: **Incoherent X-ray image and tube**. (a) First X-ray image ever taken in 1895 by Wilhelm Röntgen. (b) Image of century-old X-ray tube. Figures adapted from Refs. [94, 95]

3.2 Facility-scale sources

Large-scale facilities that produce coherent X-ray light, such as synchrotrons and free electron lasers (FELs) are excellent high-brilliance sources of energetic X-rays [96]. These sources can reach well into the keV range of photon energies and produce bright light, which can be made spatially coherent by filtering. However, they are extremely large, often the size of multiple buildings, and they share many different users. Therefore, they are not ideal for experiments involving rapid-

prototyping, but are effective for studies needing coherent high-energy X-ray light and high flux.

3.2.1 Synchrotrons

Synchrotrons were originally developed for studies of high-energy physical phenomena [93], and emitted X-rays as a secondary process [97]. However, as uses for coherent X-ray sources grew, synchrotrons began to be commissioned as high-flux X-ray sources as their primary use. Synchrotrons use strong magnets to oscillate an electron beam at incredibly high speeds. These relativistic electrons then emit coherent light, which can be used at end-stations to conduct experiments such as imaging [98] and pump-probe spectroscopy [99].

Different magnetic field schemes result in different spatial, spectral, and temporal radiation characteristics. For example, bending magnets result in a broad spectrum emission. Undulators and wigglers, which are comprised of periodic structures of permanent magnets, output a collimated beam [96].

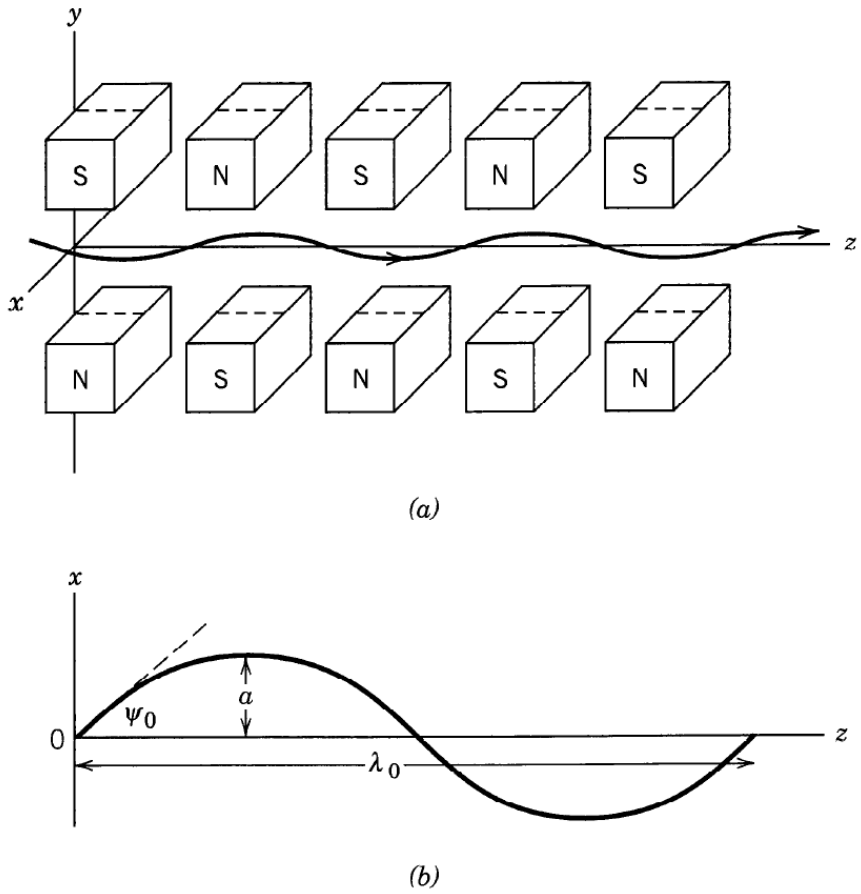

Figure 3.4: **Magnets and electron paths in a synchrotron**. (a) Image of bending magnets in a synchrotron. (b) Path of an electron with maximum transverse amplitude (a) and maximum angle ψ_0. Figure adapted from Ref. [35].

While synchrotrons emit large quantities of light, it is not necessarily monochromatic or temporally coherent from the outset. Often, an aperture must be inserted to obtain a high degree of monochromaticity [96]. Furthermore, for ultrafast time-resolved experiments, temporal slicing must be implemented. This process uses an intense femtosecond laser to scatter off of the relativistic electrons, thus shortening the otherwise tens of picosecond-long pulses [100].

3.2.2 X-ray free-electron lasers

Free electron lasers use a series of strong magnets to oscillate unbound electrons at high speeds. High-energy electrons are injected in bunches into multiple undulators. The electrons and

X-rays co-propagate and eventually interact, causing micro-bunches, which in turn emit coherent X-ray light [96]. This process is illustrated in Fig. 3.5.

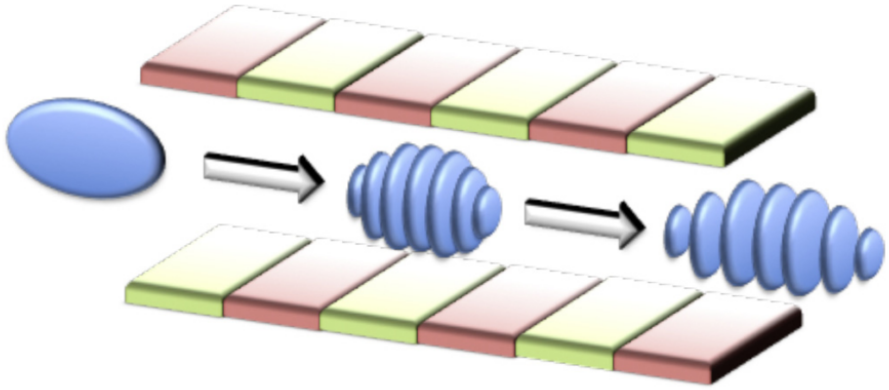

Figure 3.5: **Electron bunching in a free electron laser**. Schematic of electron bunch forming micro-bunches in between permanent magnets in a free electron laser. Figure adapted from Ref. [96].

FELs are highly tunable, and can emit light across many orders of magnitude of photon wavelengths, from the 10's of nm down to angstrom level [101]. They are also capable of producing extremely bright, femtosecond-scale pulses.

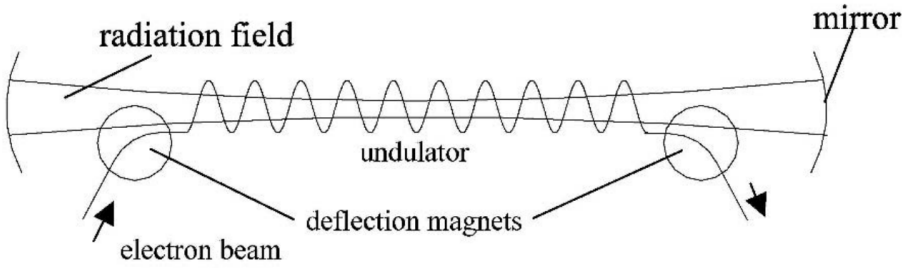

Figure 3.6: **Schematic of a free electron laser**. Diagram showing magnets, electron beam, undularor, and cavity in a free electron laser. Figure adapted from Ref. [102].

The first emission of light by this process was demonstrated in 1953 [103], when the electron beam from the Stanford Linear Accelerator (SLAC) was sent through an undulator, and light of mm-scale wavelength was produced. However, it wasn't until 1977 that a FEL demonstrated a lasing transition and gain using this technique [104]. In 2010, wavelengths on the order of Angstroms and pulses as short as 10 fs were produced using an FEL [101]. FELs continue to be a

short-wavelength, high-brilliance source capable of producing ultrafast pulses for a wide variety of of applications. Whereas synchrotrons can have multiple end-stations with multiple users at once, FELs are restricted to one end-station, and can only host one experiment at a time [96].

3.3 Tabletop sources

A significant advantage of tabletop sources is that they can be installed in a research or industrial laboratory, and therefore are readily accessible to the scientist rather than requiring proposal submission, travel, and potentially waiting months or longer for beam time. This in turn allows for rapid prototyping, high throughput, and significant customizability. Additionally, tabletop high harmonic sources are seeing rapid improvement in flux, are ultrafast, and temporally coherent from the outset with no slicing required- making their coherent flux quite high, on the order of $\approx 10^{10}$ photons/s for a single harmonic [77].

3.3.1 X-ray lasers

X-ray lasers use ionized atoms, sometimes in the form of a plasma, as a gain medium [105]. They were first demonstrated in 1985 using Ni-like selenium with a new "exploding foil" technique [106, 107] at Lawrence Livermore National Laboratory. In 1994, Rocca et al. [108] demonstrated soft X-ray lasing with a discharged plasma. A high amperage pulse was used to create a plasma in Ne-like Argon around 47 nm.

More recently, high energy Yb:YAG 1.03 μm lasers have been used to pump 0.4 kHz laser at 18.9 nm, with pulse durations of a few ps, and significant pulse energy of up to a Joule [109].

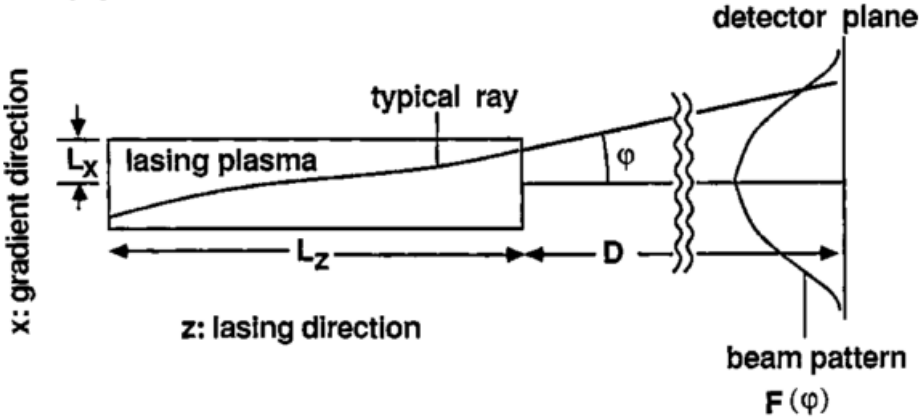

Figure 3.7: **Schematic of a plasma discharge laser**. Figure adapted from Ref. [105]

These lasers can produce high flux but do not scale favorably with wavelength since power required to pump goes like inverse wavelength to the fifth power, $P \propto \lambda^{-5}$ [110].

3.3.2 High harmonic generation

High harmonic generation (HHG) is an extreme nonlinear process driven by femtosecond lasers [111–115]. It is capable of producing spatially coherent light all the way from the EUV down to the soft X-ray. The generated wavelength scales inversely with driving laser wavelength [116], and through ever-improving laser technology continues to grow in brightness and energy. The work done in this thesis is all produced by HHG, and it will be discussed in depth in this section.

High harmonic generation has been ushering in a revolution in tabletop coherent nanoscience [115–121]. Generating the harmonic beam used in this work involves three basic components: an oscillator, a chirped pulse amplification system, and a waveguide. Systems are being developed with other types of lasers, such as mid-IR optical parametric chirped pulse amplifiers (OPCPA) systems, and gas jets rather than waveguides. These techniques are important for various types of experiments, as well as pushing the generated harmonics to higher and higher energies. Here, the focus will be on the system used for the work in this thesis; a Ti:Sapphire oscillator and a multi-pass ring CPA, and a gas-filled waveguide used to produce 29 and 13 nm light. Details of the laser system can be found in Appendix B.

High harmonic generation consists of two important processes. The first is the three-step model [114], which describes the single-atom picture. The second process is phase matching, which allows constructive interference of the harmonic light and results in the full spatial coherence of the beam [115].

3.3.2.1 The three-step model

The three-step model describes the semi-classical picture by which a high-energy photon is emitted from a single atom. The first step is the intense laser field distorting the Coulomb potential of an atom, allowing the electron to tunnel ionize out of the atom. This is illustrated in the left side of Fig. 3.8(a). Next, the electron is ripped away from the ion on the upcycle of the laser, and accelerated back on the downcycle of the laser. Finally, there is a probability of the electron recombining with the parent ion and releasing a high energy photon. Steps 2 and 3 are illustrated on the right side of Fig. 3.8(a).

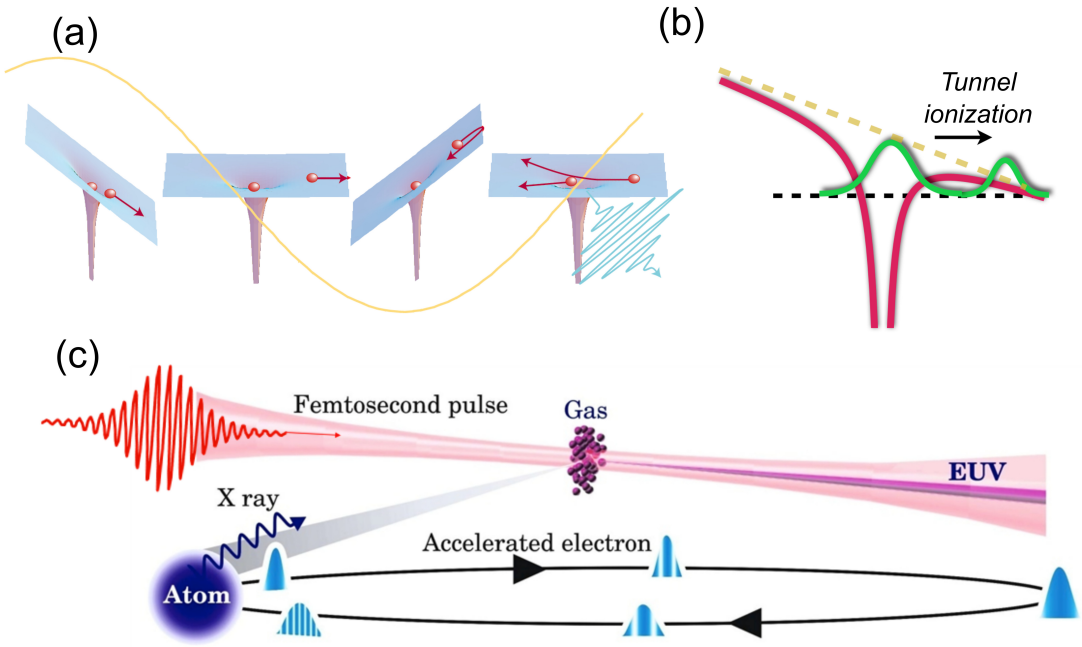

Figure 3.8: **Microscopic single-atom pictures of high harmonic generation**. (a) Three step model showing the distortion of the laser field, tunnel ionization and acceleration of the electron, and recombination and release of a photon. Adapted from Ref. [122] (b) Tunnel ionization of an electron away from an atom. (c) Semi-classical picture of HHG, adapted from Ref. [123].

Often, the atoms used in HHG are a dilute noble gas confined to a waveguide [119], but gas jets are used as well [124, 125]. HHG has also been observed in solids [126].

There are several important quantitative parameters in order to understand and predict HHG. The importance of using an ultrafast laser to drive the high harmonic process comes from the fact that the peak intensity of an ultrafast laser pulse contains an extremely strong electric field. For a 2 mJ pulse of 30 fs duration focused down to 100 microns, the peak intensity is on the order of 10^{14} W/cm^2.

The Ponderomotive energy of the laser must be considered as well. It needs to be on the order of the ionization energy of the atoms in order to facilitate tunnel ionization. The Ponderomotive

energy describes the energy in an oscillating electric field,

$$U_P = \frac{e^2 E_a^2}{4m\omega^2} \tag{3.1}$$

where e is the charge of the electron, E_a is the strength of the electric field, m is the mass of the electron, and ω is the laser frequency [41].

When the laser switches to its downcycle, the electron is accelerated towards the parent ion, and there is some probability of recombination. The maximum energy photon (or "cutoff energy") that can be emitted is related to the following [113, 117],

$$h\nu_{cutoff} \approx I_p + 3.17U_P \tag{3.2}$$

$$\propto I_L \lambda_L^2 \tag{3.3}$$

where h is Planck's constant, ν_{cutoff} is the cutoff frequency, I_p is the ionization potential and U_p is the Ponderomotive energy as defined in Eqn. 3.1. I_L and λ_L are the laser intensity and wavelength, respectively.

It is interesting to note that driving lasers with longer wavelengths are capable of producing higher energy harmonic photons. This is because the Ponderomotive energy is inversely proportional to the square of the driving laser's angular frequency, and because longer wavelengths allow the electron to be accelerated for a longer time. The trade off is that an incredible number of driving laser photons are required to make one high energy photon, so the result is lower output flux. Recently, mid-IR lasers have been used to generate supercontinuum harmonics with over 1 keV of photon energy, of harmonic order over 5000 [116].

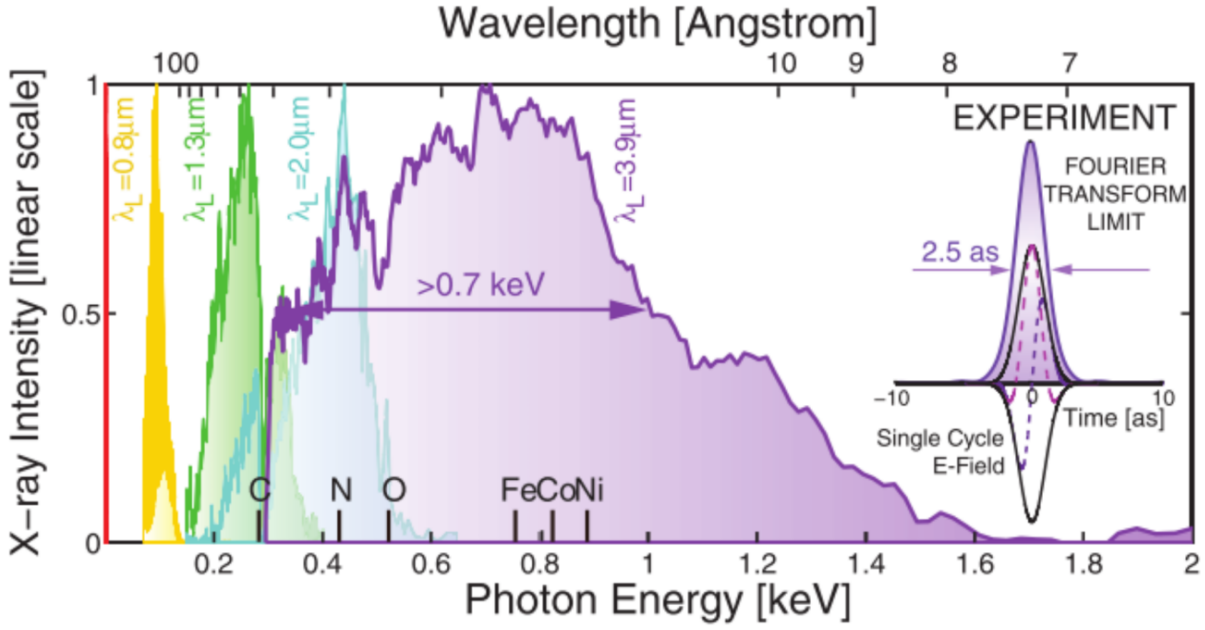

Figure 3.9: **Supercontinuum high harmonics generated from different driving laser wavelengths**. Experimental data of supercontinous harmonics generated with different driving laser wavelengths. Some harmonics were generated with photon energy > 1.3 keV. Figure adapted from Ref. [116].

3.3.2.2 Phase matching

While the single-atom picture and three step model are useful for understanding the physical process behind high harmonic generation, it is also crucial to understand the coherent buildup of many photons. Without coherent buildup, the harmonic beam would be much lower intensity due to destructive interference. Furthermore, a coherent beam is important for the signal to noise ratio of various experiments- particularly diffraction-based experiments.

Spatially coherent buildup of high harmonics is achieved through phase matching, which involves various experimental parameters [115, 120, 127]. In order to achieve coherent buildup, the phase velocity of the driving laser must be matched with that of the harmonics, where the phase velocity, $v_p = \omega/k$. Or, for a harmonic order q and a driving laser with wavenumber k_L,

$$\Delta k = k_q - qk_L. \tag{3.4}$$

This process is phase matched when the quantity $\Delta k = 0$. However, this is not done trivially.

Several system parameters must be taken into account in order to minimize the phase difference between these two fields:

$$\Delta k \approx q \left\{ \frac{u_{11}^2 \lambda_L}{4\pi a^2} - P\Big((1-\eta)\frac{2\pi}{\lambda_L}(\delta n)\Big) + P\Big(N_a r_e \eta \lambda_L\Big) \right\}. \tag{3.5}$$

The first term is the geometric phase term, corresponding the propagation of the driving laser through the waveguide. Here, u_{11}^2 is a constant relating to the propagation mode in the fiber (sometimes called the "mode factor", and in this case, it is the first zero of a Bessel function of the first kind). The quantity a is the inner radius of the waveguide and λ_L is the driving laser wavelength as before.

The second and third terms both depend on the quantity P, the pressure in the waveguide. The second term describes the phase of the neutral atoms, both the contributions from the dispersion and the nonlinear refractive index. Here, η is the ionization fraction, and the quantity δn is the difference in refractive index between the fundamental and harmonic wavelengths.

$$\begin{aligned} \delta n &= n_q - n_L \\ &\approx n_q - (n_0 + n_2) \\ &\approx n_q - (n_0 + \tilde{n_2} I_L) \end{aligned}$$

where n_q is the refractive index of the harmonic light, and and n_L is the refractive index of the fundamental light. The fundamental light's refractive index is taken to have two significant contributions, the linear term n_0 and the first nonlinear term n_2. It is important to notice the relationship between the nonlinear refractive index and the intensity.

The third phase matching term is the free electrons term. Here, N_a is the number density of the atoms at atmospheric pressure, and r_e is the classical electron radius. This term is sometimes called the plasma dispersion term.

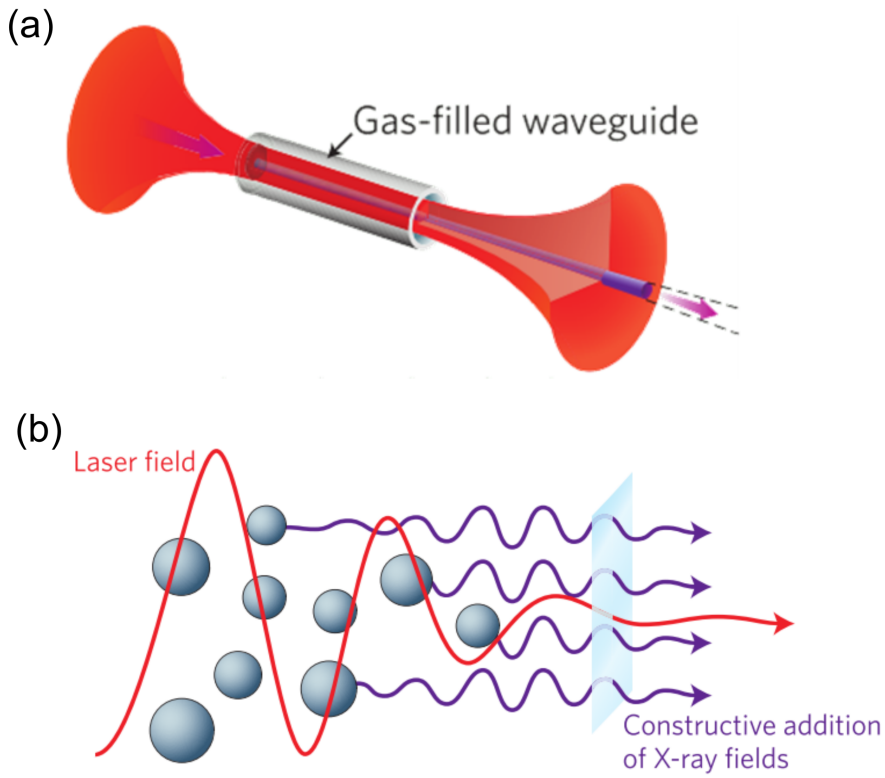

Figure 3.10: **Phase matching inside a waveguide**. (a) Diagram of an IR laser being focused into a waveguide. The driving laser and harmonics are emitted collinearly, but with different divergence angles. (b) Coherent addition of X-ray fields. Figures adapted from Ref. [120].

Typically, noble gases are used to generate high harmonics due to their high ionization energy. The two wavelengths that were generated for the work shown in this thesis are 29 nm (around 42 eV, and the 27^{th} harmonic of 790 nm light) and 13 nm (around 97 eV, and around the 61^{st} harmonic). Usually, around 40 torr of argon is used for generating 29 nm light, and anywhere from 400-800 torr of Helium for 13 nm light. However, other gases can be used to generate these wavelengths, and neon is widely used as well for many wavelengths in between (see Fig. 3.11 [121]). In HHG, only odd harmonics are phase matched due to the inversion symmetry of the gas [120].

The re-absorption of the harmonics in the gas is a challenge. In particular, 13 nm light is readily reabsorbed into helium. The phase matching pressure of helium for 13 nm light is quite high, on the order of an atmosphere. For 750 torr of helium, the absorption length is approximately 1

mm [42], while for argon, the phase matching pressure is around 40 torr, and the absorption length is closer to 5 mm. This may seem like a small difference, but it means that after the active section of the fiber, these gases must be very efficiently pumped out of the system. This is aided by a differential pumping block and a combination of roughing and turbo pumps immediately after the fiber.

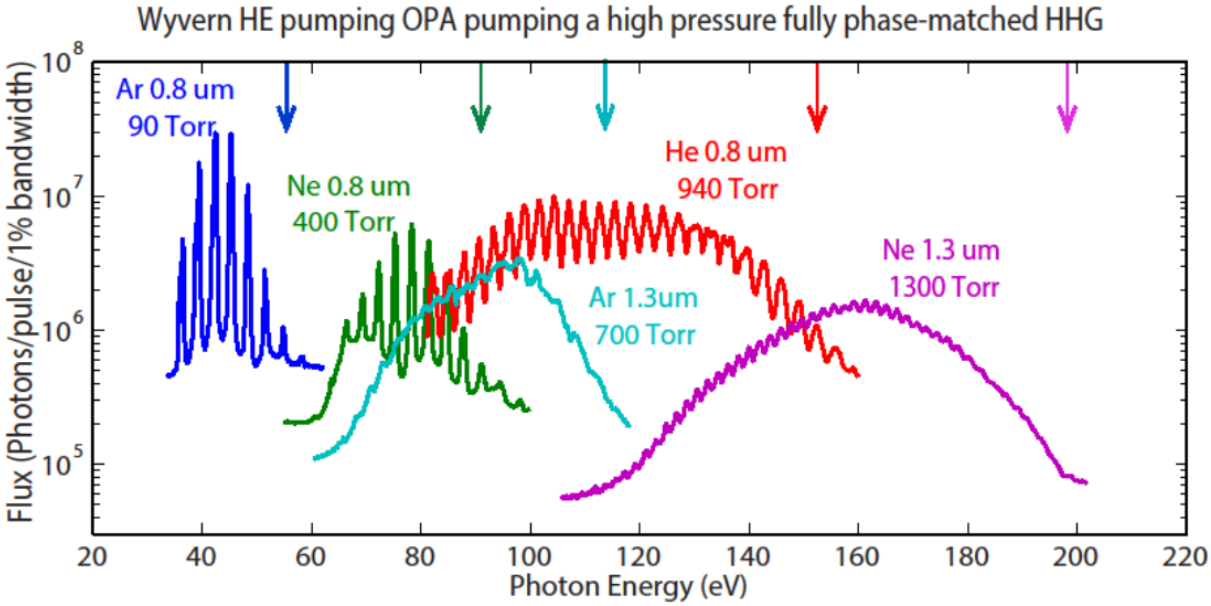

Figure 3.11: **Generation of harmonics from different gases**. Experimental demonstration of phase-matched harmonics in different gases and at different pressure. Figure adapted from Ref. [121].

3.3.2.3 Driving harmonics with a Ti:Sapphire system

As mentioned earlier, the whole process of HHG is dependent upon having a bright, high intensity pulsed laser that can provide a very strong electric field. The work done in this thesis used a near-IR Ti:Sapphire laser system capable of producing 2 mJ, 20 fs pulses at a few (3-5) kHz repetition rate.

To drive the harmonics used for the work done in this thesis, a KMLabs oscillator and amplifier system based on a Ti:Sapphire crystal gain medium were used. HHG is driven by ultrafast

lasers, and laser engineering and stability is advancing rapidly. The laser my colleagues and I used for the work in this thesis is from about 2003, so it was important to understand all the components and how to align it from scratch. More details about the laser system can be found in Appendix B.

3.3.2.4 Characterizing the pulse

The ultrafast pulses emitted by these amplifiers are among the fastest events ever created by humans. Unfortunately, this makes it difficult to measure the pulses. To measure a quantity, it is usually required that the measuring device have finer gradations than the object to be measured.

Fortunately, a technique known as FROG (frequency resolved optical gating), solves this measurement problem. This technique uses the electronic response in a nonlinear medium caused by the pulse as a measurement tool. By sending the pulse through a 50/50 beamsplitter, delaying one of the arms, and recombining them in a SHG crystal to create a second harmonic signal, the FROG technique uses a delay stage to collect second harmonic spectra at different delay times. This information is then fed into an algorithm capable of reconstructing complex pulses in the temporal and spectral domains [128–131].

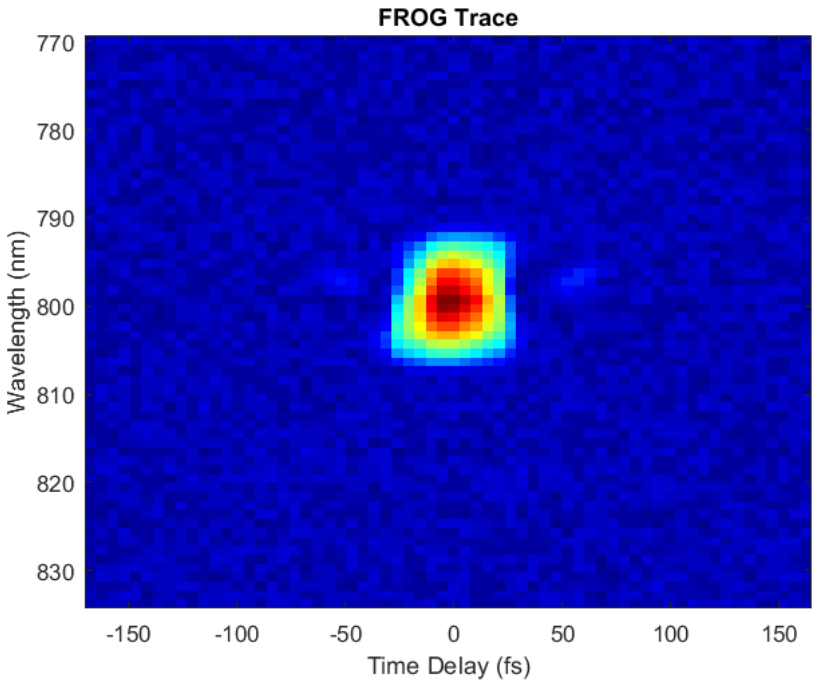

Figure 3.12: **FROG trace**. FROG trace of a 30 fs ultrafast pulse. This measurement was taken on a KMLabs Dragon Amplifier System.

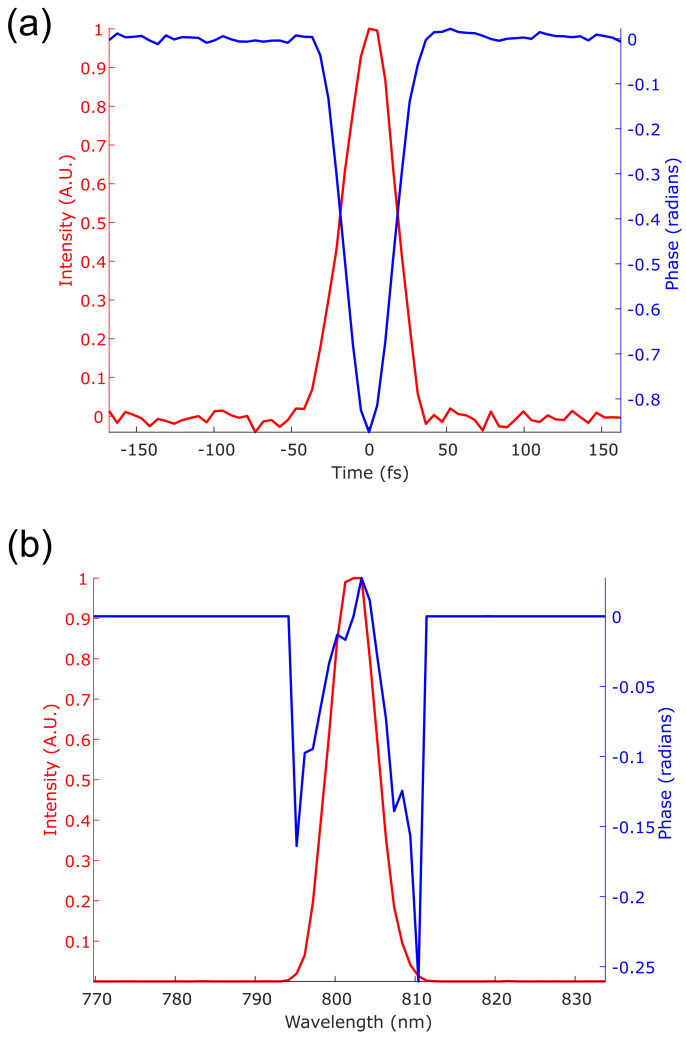

Figure 3.13: **Retrieved temporal and spectral FROG traces**. (a) Pulse retrieved in the temporal domain and (b) spectral domain. Obtained from the same data set shown in Fig. 3.12.

Good pulse characterization is an important diagnostic. Without a pulse shaper (see Appendix B for a description), it would otherwise be quite difficult to determine if the pulse was as short as possible. For instance if there was third-order spectral phase by misaligned gratings, this could cause the high harmonic flux to be low, and without FROG, it would be very difficult to determine what the problem is. Extensions on ultrafast pulse measurement techniques include ptychographic FROG [132] and multiphoton intrapulse interference phase scan (MIIPS) [133, 134].

3.4 Tabletop EUV microscope design

3.4.0.1 Driving laser rejection

In most cases, the driving laser light must be separated out from the harmonics in the system before entering the imaging chamber. The driver is many orders of magnitude more powerful than the harmonic light, so it would burn the optics, sample, and camera. It would also overwhelm the signal to noise ratio of the diffraction.

The beam is reflected (driving laser and harmonics) from two silicon rejecter mirrors, set at Brewster's angle for the IR driving laser, and then passed through two 200 nm-thick filters. For 29 nm experiments, aluminum filters are used along with plain silicon rejecter mirrors, while for 13 nm experiments, ZrO_2-coated or Ru-coated Si rejector mirrors are used, along with zirconium filters.

3.4.1 Focusing and spectral filtering optics

Another important aspect of the beamline design is the EUV multilayer mirrors. These serve to spectrally filter the beam by allowing the unwanted adjacent harmonics to be separated out while reflecting the desired harmonic. For most imaging experiments, it is best to have the beam be as monochromatic as possible.

When generating 29 nm light, Mg:SiC multilayers are typically used, while Mo:Si is used for 13 nm. These mirrors are designed by various collaborators from CXRO and other facilities [42].

Some configurations use two near-normal incidence mirrors, where the second one is curved to focus the beam, in a z-fold geometry. Other experiments use 45° mirrors in conjunction with an ellipsoidal focusing mirror.

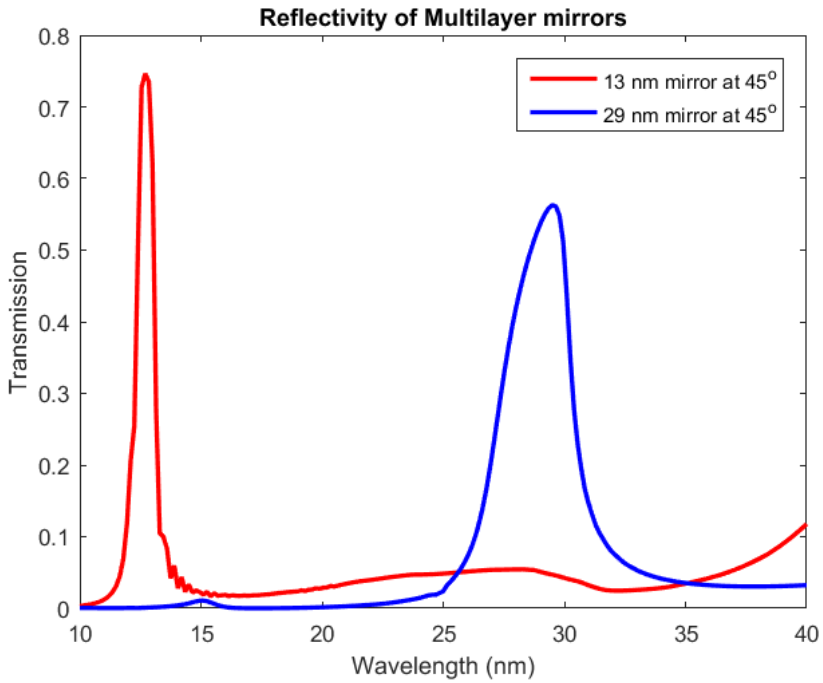

Figure 3.14: **Reflectivity curves of multilayer mirrors for different wavelengths**. Data and designs from [135] and [42].

The ellipsoidal mirror is a glancing-incidence Ni-coated mirror that images a point very far away (such as the exit of the waveguide) and focuses it to a significantly demagnified spot. For the work shown, the mirrors used had a 100 - 150 cm object distance and a 10 cm image distance, providing demagnifications of 10× and 15× respectively.

3.4.2 Detection

Many different modern cameras are sensitive to X-ray and EUV light. Two different cameras are used for different experiments in the work done in this thesis; both with CCDs with back-thinned silicon chips and 2048 x 2048 pixels arrays. One is an Andor iKon-L, which has 13.5 μm square pixels, and bolts onto the outside of the vacuum chamber. The other is a PI-MTE with 13

μm square pixels, and it is vacuum compatible and can go inside the chamber.

Both of these detectors experience various sources of noise, which can be a problem when recording an image– particularly at high spatial frequencies which have lower signal. The primary sources of noise are photon shot noise (sometimes called signal noise), thermal noise (sometimes called dark noise), and readout noise, caused by the analog to digital conversion. The photon shot noise depends upon the number of photons incident on the pixel and the quantum efficiency at that wavelength. The readout noise is higher for faster readout rates, so this can be reduced by reading out at a slower rate– typically 1 MHz. Thermal noise can be decreased by cooling the CCD, generally cool to about $-60°$C using a peltier. The shape of the noise is dominated by the shot noise, which can be modeled by a Gaussian. Typically, along with cooling and a slower readout rate, the data is post-processed by thresholding, which is done by subtracting a constant background.

Chapter 4

Ptychographic Imaging of Extended Samples in a Reflection Geometry

4.1 Introduction

Ideally, a microscope ought to be suitable for a variety of samples. While transmission imaging of pinhole-type samples using isolated-object CDI (ioCDI) has been incredibly valuable and is still appropriate for some samples, many nanoscale electronic devices are in need of a metrology that can image thick, reflective objects. However, reflection imaging presents a number of challenges, particularly at high NA. Binary pinhole-type samples block any stray light so long as they are reasonably overfilled by the beam. Reflection samples are often non-trivially reflective everywhere, and therefore the isolation constraint in ioCDI will generally not be satisfied.

An early solution to the isolation constraint was known as keyhole CDI [78]. Here, the illumination constraint is imposed on the beam rather than on the sample, allowing an extended object to be imaged. Although promising results have been obtained with this technique [77], it requires strong knowledge of the beam- and is helped immensely by high phase curvature. For a Gaussian beam, the phase curvature is highest further away from the focus, but the beam is bigger there as well (see Appendix A for more information). Hence it becomes inconvenient to satisfy both of these requirements.

Ptychography CDI has become the tool of choice for many applications in imaging extended samples. This chapter shows the work done in imaging extended, reflective objects at high NA using a tabletop high harmonic source.

In this chapter, I describe work conducted with my colleagues to obtain the first high-NA

tabletop reflection-mode image with EUV light, and subsequently pushing that work to even higher NA with 2λ resolution, and finally multicolor hyperspectral EUV imaging. I will also describe the fabrication technique of a test sample I made using nanolithography. I discuss in detail calculations related to height maps, obtained from the reconstructed phase, and how to treat them for a few different cases.

4.2 Nanofabrication of a test sample

In order to achieve a first demonstration of any technique, in this case high-NA reflection imaging, it is helpful to start with a well-known, well-characterized test sample. A sample was fabricated in-house using electron beam lithography to expose a polymethylmethacralayte (PMMA) resist spun on top of a silicon wafer. The resist was then developed in a 1:3 solution of methyl-isobutyl-ketone:isopropanol. The sample was then coated with approximately 30 nm of titanium, and lift-off was performed in an acetone bath. The pattern used was one of the pre-loaded lithography patterns from the Nanometer Pattern Generating System (NPGS) software, and is comprised of easily recognizable, micron-scale shapes. Steps from the fabrication process are shown in Figure 4.1

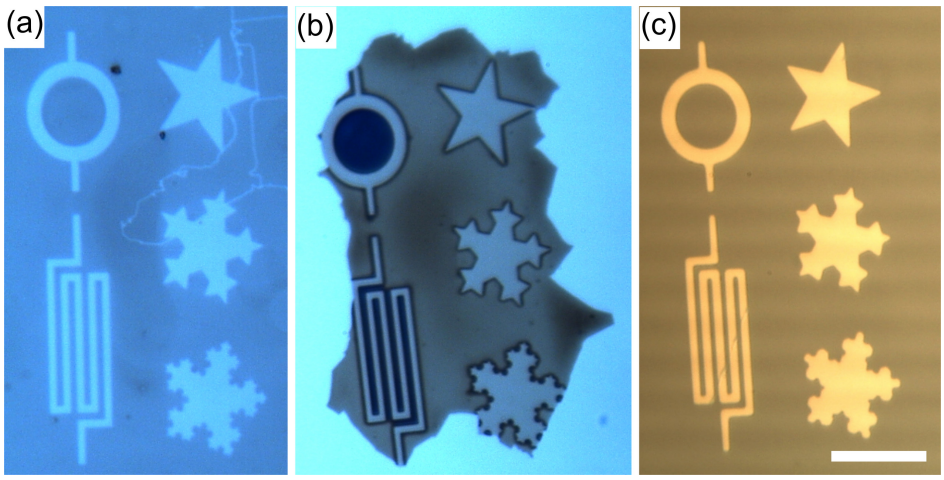

Figure 4.1: **Nanofabrication of titanium on silicon sample**. Optical microscope images of nanofabrication steps of the test sample. (a) Sample after electron beam exposure and development. In this instance, the shapes were inadvertently patterned over part of a map of the United States. (b) After being coated with titanium, acetone liftoff had been partially achieved. More sonication in an acetone bath was required. (c) Finished fabrication, with titanium shapes on silicon. The scale bar is approximate and shared among all 3 images, and is about 15μm.

4.3 First demonstration of reflection-mode EUV imaging on a tabletop

This section is adapted from Seaberg et al. [39].

The initial tabletop HHG demonstration of reflection imaging was done in 2014 by Seaberg et al. [39]. Limited results in reflection had previously been obtained in the EUV/X-ray at large-scale facilities, but were limited to isolated objects [136, 137], reflective masks at normal incidence [138], or low NA [139].

The tabletop demonstration was achieved using a z-fold mirror geometry, shown in Figure 4.2. The two mirrors in the fold are both wavelength-selecting EUV multilayer mirrors. The first is flat while the second is curved to focus the beam onto the sample. An aperture is used as well to help place a hard edge on the beam, which aides in the ptychography reconstruction.

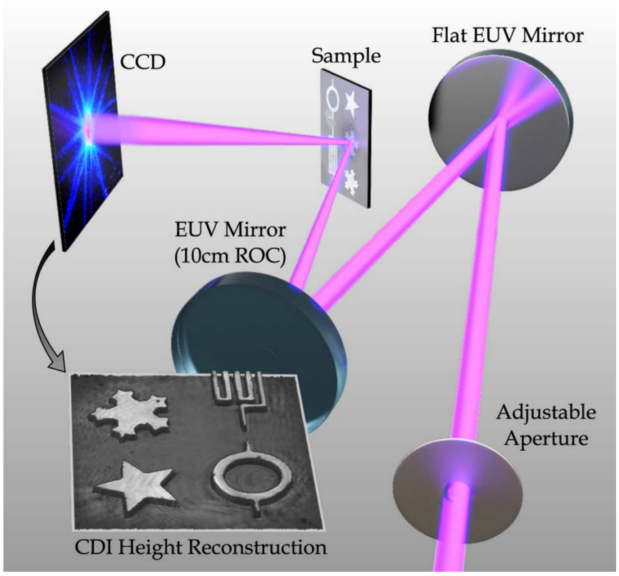

Figure 4.2: **Reflection imaging with a z-fold**. Experimental schematic of reflection imaging with on-axis z-fold optics. Also shown is the ptychographic reconstruction of the height map. Figure adapted from Ref. [39].

The results, reconstructed from collecting 90 scan positions with an effective NA of 0.1, are robust and consistent with the known pattern, as well as the SEM (Fig. 4.3) and AFM (Fig. 4.4).

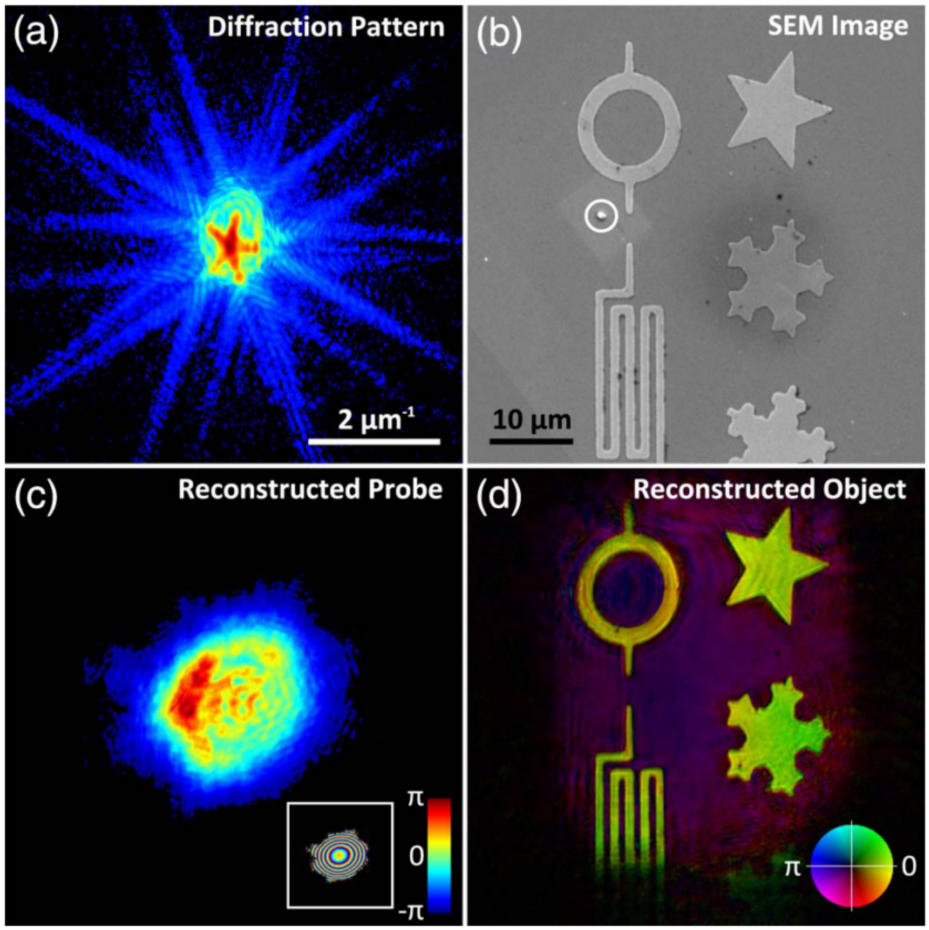

Figure 4.3: **Ptychographic imaging in reflection mode**. Results of reflection mode reconstruction. (a) A diffraction pattern from the ptychography scan. (b) SEM image of the sample, highlighting debris introduced after imaging. Burned-on hydrocarbon squares caused by the SEM are visible as well. (c) Reconstructed probe amplitude, with an inset showing the probe phase. (d) Reconstructed object, where brightness represents the amplitude and the hue represents the phase. Figure adapted from Ref. [39].

4.4 Height Maps

The topography of the sample can be further investigated by generating a height map. This involves decoupling the two contributions to the reconstructed phase; the geometric phase and the material (or "Fresnel") phase. The geometric phase is the phase offset caused by the wave traveling different path lengths due to height variations in the sample. Complex transmissivities or reflectivities will have phase terms, which indicate the phase lag caused by a material. The Fresnel

phase refers to this quantity.

The reconstructed height map is compared to an AFM image of the sample in Fig. 4.4.

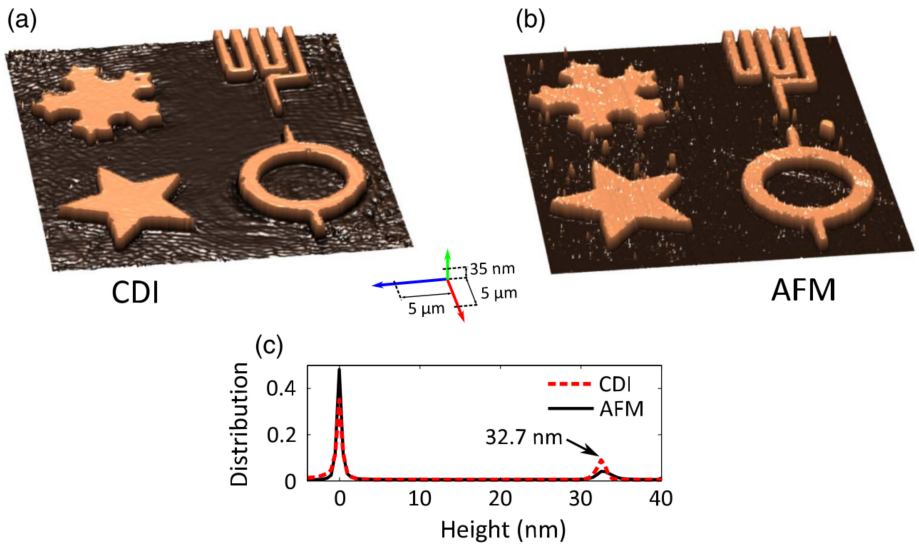

Figure 4.4: **Comparison of CDI and AFM height maps**. (a) Height map based on ptychographic phase and (b) AFM. Three dimensional scale bar is shown as well. (c) Histogram of heights based on the CDI reconstruction and AFM, showing excellent agreement. Figure adapted from Ref. [39].

It can be seen from this case that nm-scale precision is possible, though it does involve some a-priori knowledge of the sample composition and is potentially improved by secondary measurements, such as ellipsometric measurements. The general formula for a height map is relatively simple, and depends on the contributing phases;

$$\phi_{total} = \phi_{geometric} + \phi_{Fresnel} \tag{4.1}$$

$$= -2\,k\,h\,cos\theta + \phi_{Fresnel} \tag{4.2}$$

where k is the wavevector equal to $2\pi/\lambda$, h is the height of the feature, θ is the angle of incidence, and ϕ_{total} is the reconstructed CDI phase, which includes both geometric and Fresnel contributions.

Although the following examples are worked through with reflection imaging in mind, the same can be done in transmission imaging, where the phase delay for a normal incidence experiment is simply related to the thickness of the sample and its Fresnel phase.

4.4.1 Decoupling height and material information

A few simple cases, explored here, can be solved analytically. However, for more complicated structures, numerical techniques are necessary. This is discussed in Chapter 5.

4.4.1.1 Thick monolayer at a step

First, consider the simple case where there is a geometrical step composed of a different material than the substrate and the ambient material (assumed to be vacuum). These materials have the indeces of refractions n_1, n_2, and n_3 as shown.

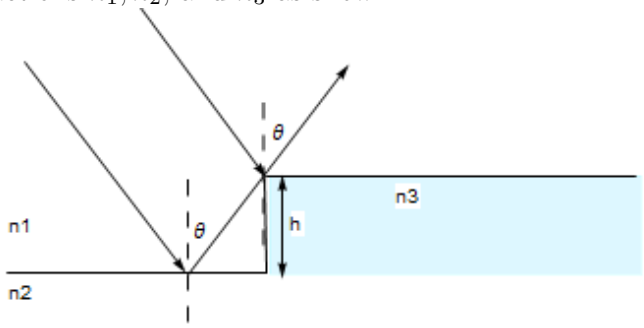

Taking θ to be the angle of incidence, and the subscript F to indicate the Fresnel contribution, the phase change acquired will be following:

$$\phi_{feature} = \phi_{n_3,F}$$

$$\phi_{substrate} = \phi_{n_2,F} + 2\,h\,cos\theta$$

This case is relatively straightforward, as there are no thin film effects and it is assumed that the absorption length of the light is much less than the height of the material with refractive index n_3. That is to say, no light makes it through n_3 to the substrate below in this model.

One subtlety of height maps is that the features and substrate (for a binary object) must somehow be separated. For a flat and relatively binary sample– like the one shown in the reconstructions in this chapter– this can be achieved by separating features from substrate via a histogram, like the one in Figure 4.4. Then, the height map is generated with two different Fresnel phases for the two different regions- features and substrates. This process can be more challenging if significant height and material variations are present.

4.4.1.2 Thin monolayer case

Next, the case of a thin film is considered. This case is different from the step in that the layer (material with index n_2 in the diagram below) is now thin enough that a non-trivial amount of light penetrates through, some of which reflects off the substrate below. This is important, as many materials grow thin native oxide layers, or are composed of multiple distinct, semi-transparent layers. The full derivation for this case can be found in Ref. [8]. It is considerably more complicated than the thick step case treated above because thin film interference effects now must be considered.

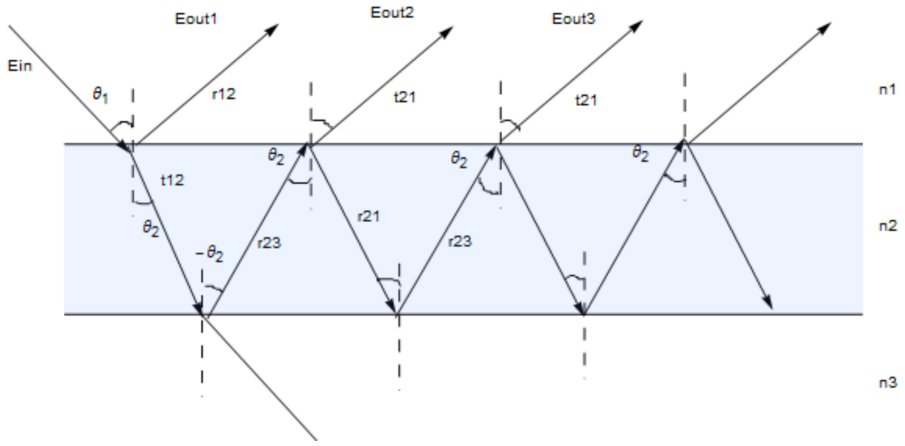

Taking the reflectivity coefficient to be r_{12} when a wave in material 1 encounters a surface of material 2, incidence angles on the interior of a material ξ to be θ_ξ, and input electric field to have magnitude 1, the complex reflectivity coefficient is,

$$r_{total} = \frac{r_{12} + r_{23}e^{2\,i\,k_0\,n_2\,h\,cos\theta}}{1 + r_{12}r_{23}e^{2\,i\,k_0\,n_2\,h\,cos\theta}} \tag{4.3}$$

This result is obtained by considering the reflections as a series and finding the limit. Equation 4.3 is not easily decoupled into real and imaginary parts, and therefore calculations are best done numerically. Adding more layers quickly becomes more complicated, and is best done numerically as well.

4.4.1.3 Different monolayers on different substrates

For two different monolayers on two materials, the two above cases can be combined. This is the case of the titanium on silicon pattern, as both of these materials grow native oxide layers.

The overall geometric height change can be calculated, but there are too many unknowns if the thickness of the two oxide layers are also unknown. Values of thicknesses for native oxide layers can often be found in the literature, and techniques such as ellipsometry can determine thickness as well.

Now, the most accurate model for the titanium stars sample is considered. This is the case of the different monolayers and substrates on either side of a step.

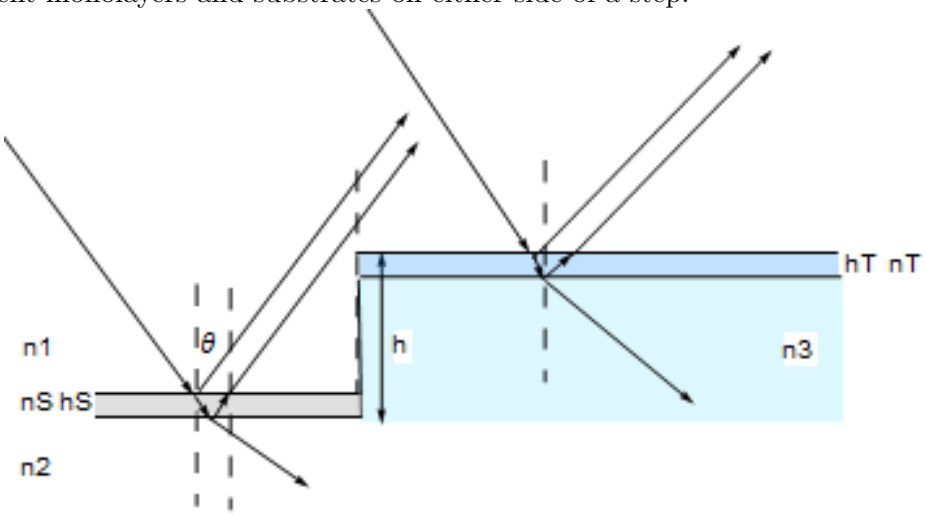

The titanium stars sample is deceptively simple, as the titanium and silicon both grow native oxide layers. While considering these materials to just be titanium and silicon still yields fairly accurate results, additional corrections by accounting for the oxide layers improves agreement with the AFM measurement [39, 40]. The detailed comparison of these measurements is discussed later on in this chapter.

In principle, the complex reflection coefficient of an arbitrarily complicated stack of layers can be obtained by using numerical propagation and directly solving Maxwell's equations inside the stack. This has been achieved by using IMD software [140] and by direcly solving Maxwell's equations in the stack [141] and can be easily incorporated into data gathered with other methods [53]. This technique will be discussed further in Chapter 5.

4.5 Reflection imaging with high NA

This section is adapted from Zhang et al. [40].

As an extension to the reflection work shown in Fig. 4.3, higher resolution can be obtained by moving to an off-axis focusing geometry. This facilitates much higher numerical aperture by allowing the sample to be much closer to the detector. It also eliminates experimental difficulties around z-fold geometries such as the sample cutting the beam, and astigmatism introduced by using the focusing mirrors slightly off-normal incidence.

The ellipsoidal focusing optic is also excellent because within the EUV range it is chromatically agnostic, and can be used to focus a broad range of wavelengths. The schematic of the high-NA microscope is shown below in Figure 4.5. As discussed in chapter 1, tilted plane correction (TPC) [38] is particularly important at high NA, as higher spatial frequencies will be more distorted.

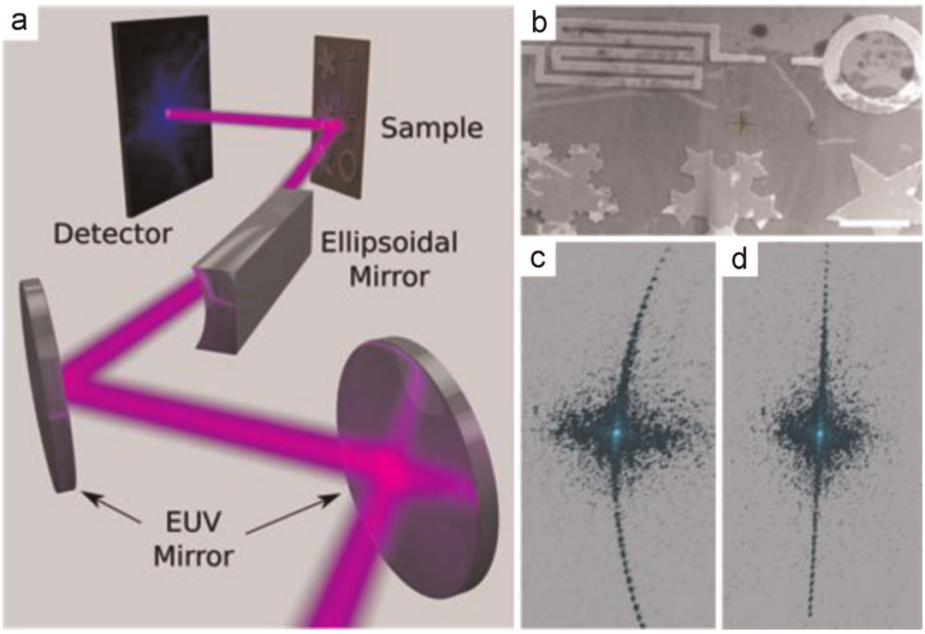

Figure 4.5: **Schematic of high NA reflection imaging** (a) Schematic of the microscope, including two EUV multilayer mirrors, an off-axis ellipsoidal focusing mirror, and the sample set at 50.5°. (b) SEM image of the sample. The scale bar represents 10 μm. (c) Diffraction pattern before TPC and (d) after. Figure adapted from Ref. [40].

The ellipsoidal mirror focuses the light off axis at a highly grazing angle of 5^o. This allows the sample to move closer to the detector, and results in a higher resolution image. Furthermore,

the diffraction curvature is very apparent at high numerical aperture, particularly in a strongly diffracting sample. The effective NA for this experiment was 0.4.

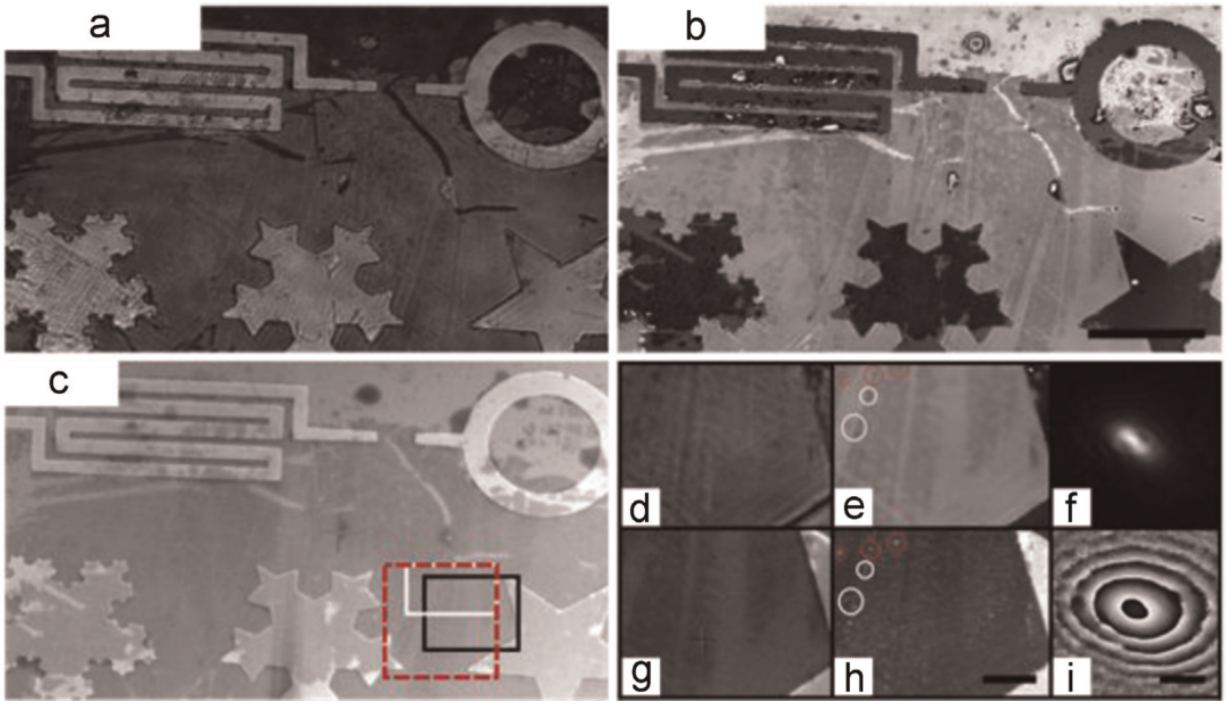

Figure 4.6: **Reconstruction of high-NA reflection image**. Ptychographic reconstruction compared to SEM and AFM measurements. (a) Ptychography CDI amplitude and (b) phase. (c) SEM image, showing a black box zoomed in and shown in (d). (d) Amplitude of zoomed in region and (e) phase. (g) High resolution SEM of zoomed-in region and (h) AFM of same region. (f) Shows the amplitude and (i) the phase of the probe. The scale bar in (b) is 10 μm and the scale bar in (h) is 1 μm. Figure adapted from Ref. [40].

The resolution was characterized using multiple methods, shown in Figure 4.7. The transverse resolution was found to be 38 and 76 nm in the vertical and horizontal directions, respectively. The discrepancy is due to the distortion caused by conical diffraction. Because the sample was at an angle horizontally but not vertically, the resolution in that direction is worse.

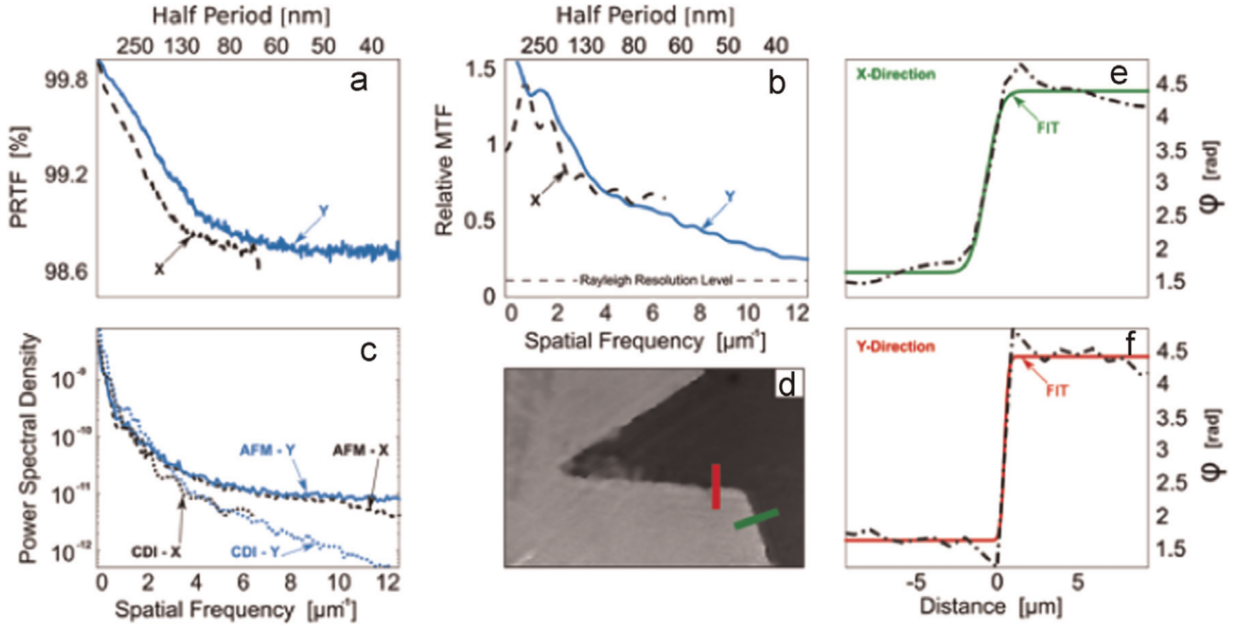

Figure 4.7: **Transverse resolution characterization**. (a) Phase retrieval transfer function (PRTF). (b) Relative modulation transfer function (MTF) between the AFM measurement and the retrieved phase. (c) Power spectral densities in each direction for the AFM and CDI. (d) Locations of 10%-90% knife edge test. (e) Knife edge test in the x-direction, along with its error function compliment (ERFC) fit. (f) Knife edge test in the y-direction with its ERFC fit. Figure adapted from Ref. [40].

The resolution characterization is discussed in further detail in Ref. [40]. The transverse resolution is very high, but it turns out that the axial resolution is even better. The axial resolution is related to the reconstructed phase– as well as the known material of the sample, as discussed in the previous section.

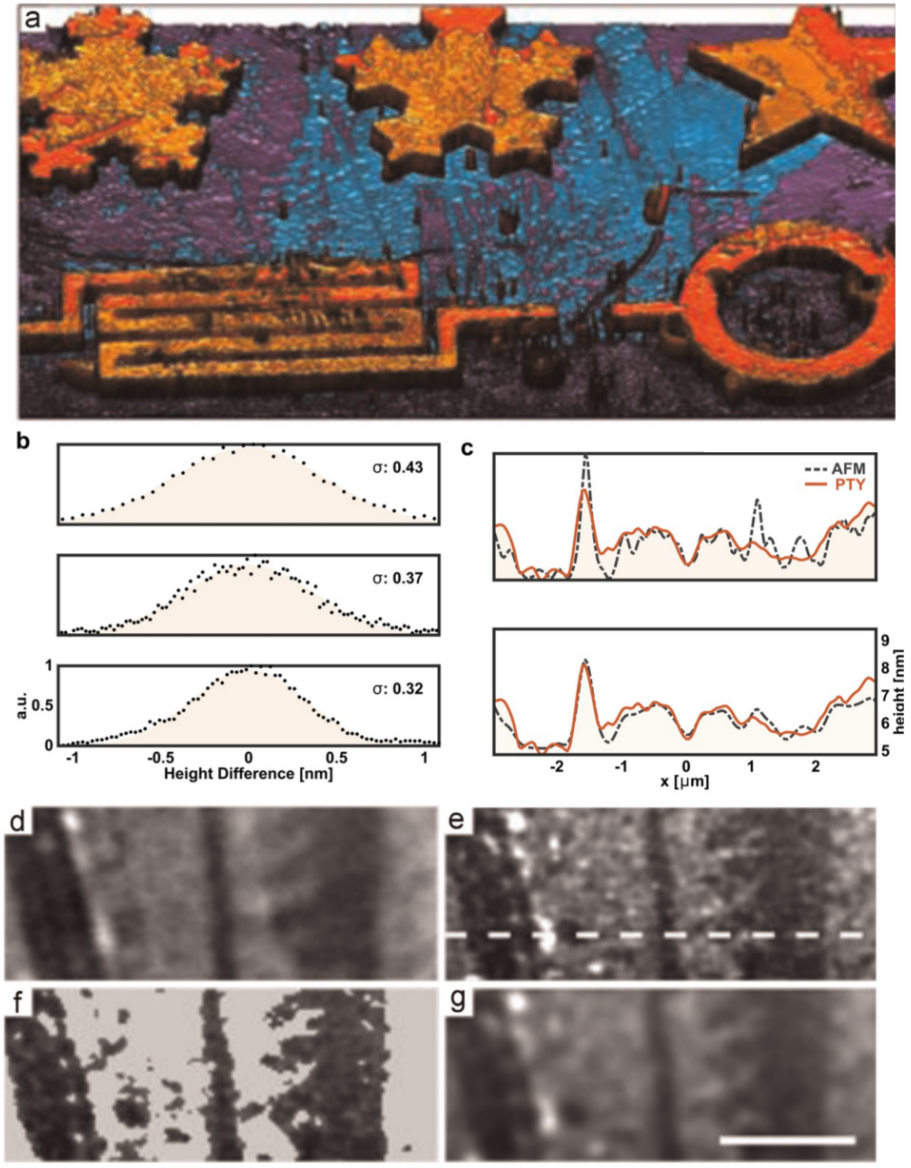

Figure 4.8: **Height map and axial resolution from high-NA data**. (a) Height map constructed from high-NA data. (b) Histograms of differences in height measurement between AFM and ptychography CDI. The top histogram contains no filtering (comparing (d) and (e), while the middle one has values outside the area of interest removed (comparing (d) and (f)). The bottom histogram shows differences after the AFM data has been smoothed with a Gaussian point spread function (PSF) (comparing (d) and (g)). (c) Height profiles taken along the white dashed line shown in (e). The top lineouts compare (d) and (e) while the bottom lineouts compare (d) and (g). (d) Ptychographic height map. (e) Unfiltered AFM. (f) Histogram filtered AFM. (g) PSF-Filtered AFM. Scale bar is shared by (d)-(g) and is 2 μm. Figure adapted from Ref. [40].

The reconstructed height shown in [40] agrees with the AFM measurement within 0.6 nm

after smoothing (to within 95% confidence), and is not limited by the numerical aperture of the system, but rather the sensitivity of the phase- which is determined by the bit-depth of the camera and the signal to noise in the diffraction, as well as errors in other quantities such as the wavelength and sample-detector distance. The height map also accounts for native oxide layer growth, which was measured with an ellipsometer to be 3.0 nm of native SiO_2 on the substrate. Ellipsometry was not tractable on the small titanium features, so there was taken to be 2.9 nm of TiO_2 on the features based on values from the literature [142, 143].

4.6 Extensions to ptychography

Part of why ptychography is so powerful stems from the fact that there is so much information redundancy in the data. Indeed, this is powerful enough to perform a blind deconvolution between the object and probe, but many other extensions are possible.

4.6.1 Multi-mode ptychography

Interestingly, mutually incoherent modes can be parsed out in ptychography under certain conditions. This technique is known as ptychographic information multiplexing (PIM) [87, 144]. One application of this is with different colors. This multiplexing is of interest in the EUV because there is such high spectral sensitivity that even a few adjacent harmonics can provide exquisite material sensitivity. Furthermore, multilayer mirrors often leak through more than one harmonic, and the multicolor algorithm can be used to filter out unwanted neighboring harmonics.

Color is not the only source of mutual incoherence by which ptychography can be multiplexed. The use of ptychographic multiplexing to image multiple fields of view has been demonstrated with different colors and polarizations [60] and with multiple spatially separated probes [85].

4.6.1.1 Multicolor EUV ptychography

This section is adapted from Zhang et al. [145].

Color multiplexing in the EUV is interesting for resolving material information and improving

image fidelity. Even with as few as 3-4 adjacent harmonics, differences in reflectivity can be discerned.

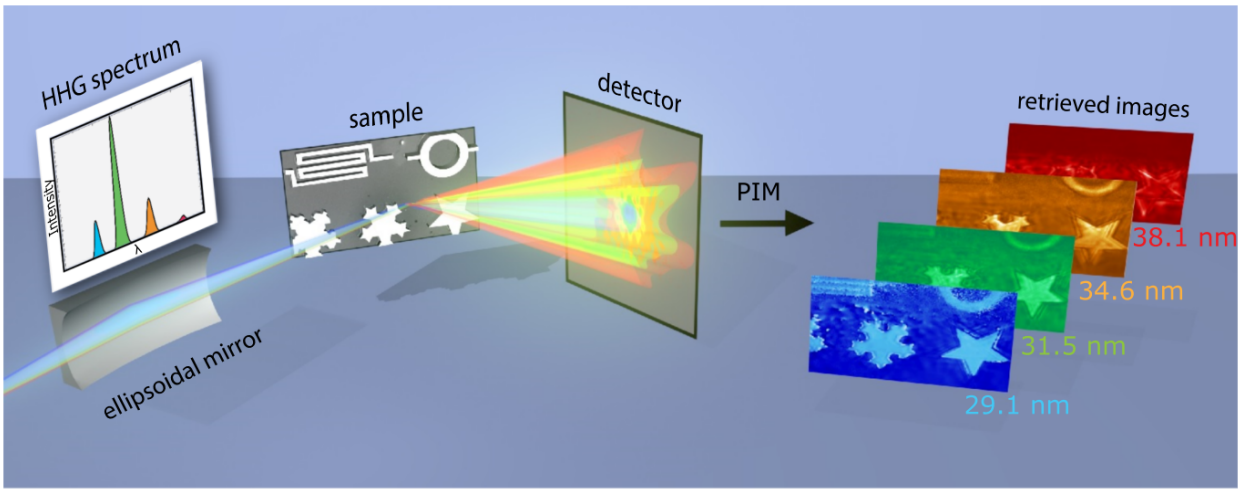

Figure 4.9: **Setup of hyperspectral reflection imaging**. Multiple wavelengths illuminate and are scattered from the sample. Objects and probes are then simultaneously reconstructed at different wavelengths. Figure adapted from Ref. [145].

Since the nickel-coated ellipsoidal focusing mirror does not spectrally filter or introduce chromatic aberrations, it is an excellent choice for focusing multiple colors at once. By replacing one EUV multilayer mirror with a broader bandwidth reflectivity mirror, such as gold or silicon, more harmonics are allowed to get through the system.

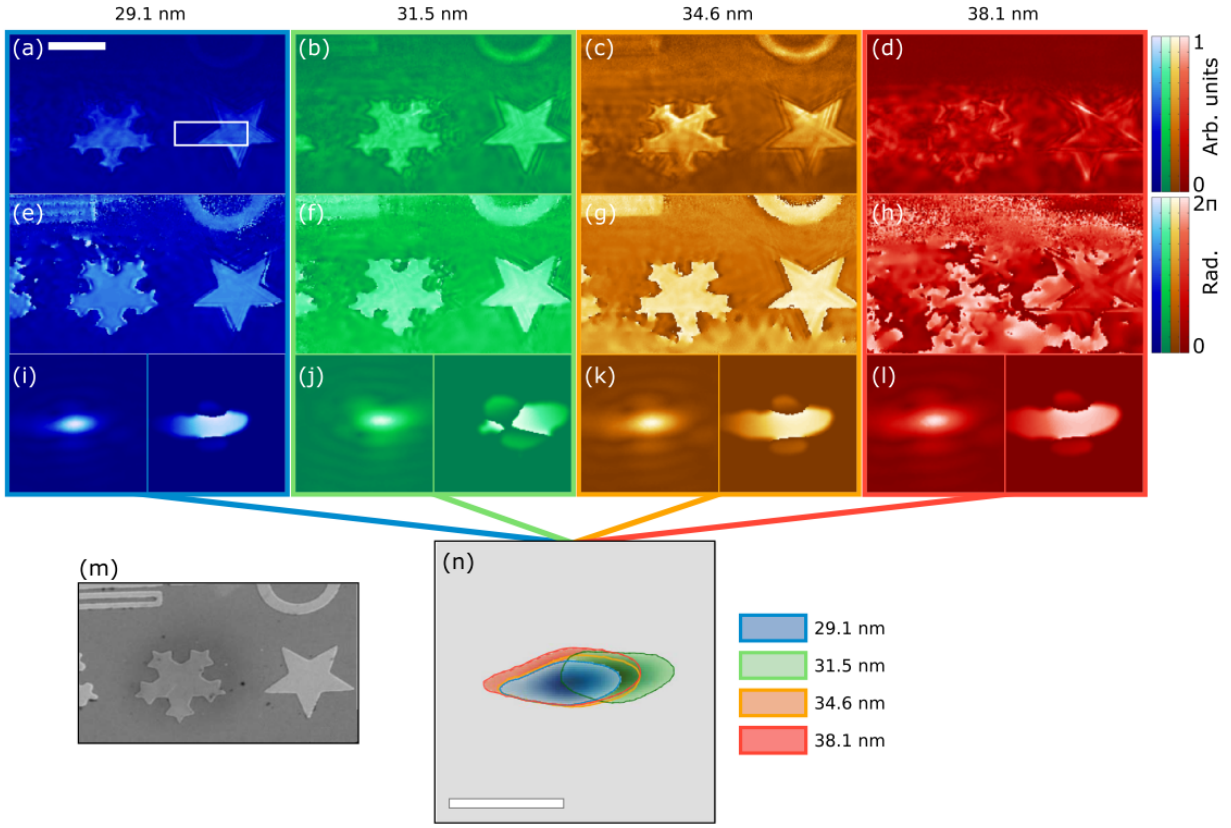

Figure 4.10: **Multicolor reconstructions in the EUV**. The top row (a)-(d) shows the reconstructed amplitudes and the second row (e)-(h) displays the reconstructed phases. The third row (i)-(l) show the reconstructed probes corresponding to each color, with normalized amplitude on the left and phase on the right. (m) SEM image of the sample for comparison. All images of the object share the same scale bar shown in (a) of 10 μm. The white rectangle in (a) shows the region analyzed in Figure 4.11. (n) Shows all of the probes together. They do not overlap perfectly. Scale bar is 10 μm. Figure adapted from Ref. [145].

These different reconstructions can be understood in terms of relative reflectivity between the features and substrate. By exploring what the reflectivity ratio is expected to be at different wavelengths (using the known sample composition from Refs. [39, 40]), the experimental result can be compared to the theoretically expected ratio of reflectivities, shown in Fig. 4.11. Only three of the reconstructed objects with the highest signal to noise are compared here.

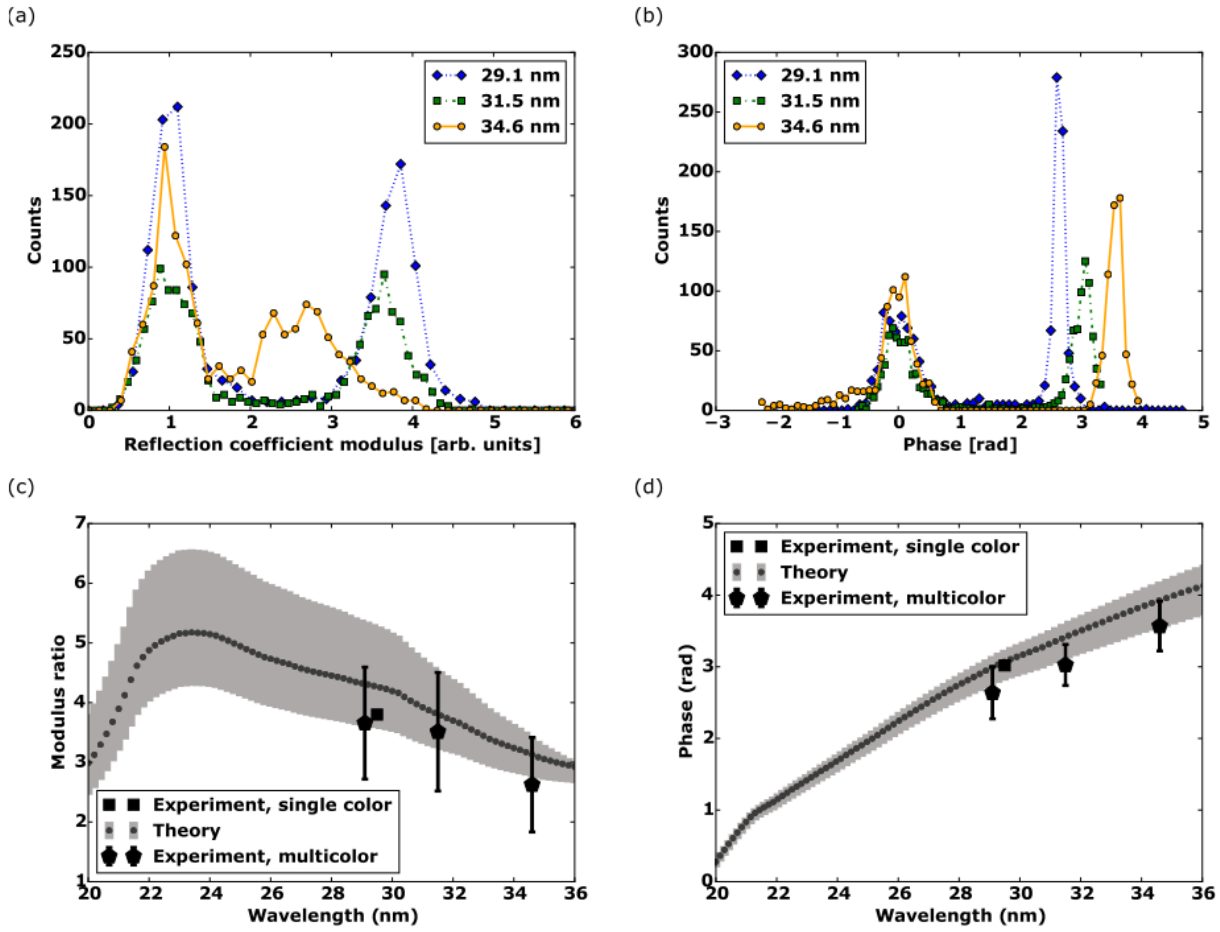

Figure 4.11: **Contrast ratio analysis in EUV hyperspectral imaging**. Contrast between sample features and substrate at different wavelengths, corresponding to white rectangle shown in Fig. 4.10. (a) Normalized histogram of reflectivity values. (b) Histogram of phase values. (c) Theoretical and experimental values for the ratio of reflectivities between the titanium features and silicon substrate. (d) Theoretical and experimental phase difference between the features and substrate. Figure adapted from Ref. [145].

4.7 Conclusions

The work shown in this chapter demonstrates tabletop reflection-mode imaging at high NA and with arbitrary angle of incidence. This technique is incredibly important for materials and interface science, as well as semiconductor fabrication metrology and inspection. Incorporating TPC is crucial to high NA imaging, and will allow incredibly high resolution as HHG sources are developed at shorter and shorter wavelengths.

The work shown in the next chapter extends reflection mode imaging to include a real-world industrial sample with a complex chemical composition, and uses the sensitivity of EUV to analyze that chemical composition.

Chapter 5

Quantitative Ptychographic Imaging of Material Properties

5.1 Introduction

This chapter discusses recent developments in quantitative imaging with ptychography CDI. In particular, I describe two new approaches that can return chemically-sensitive, spatially-resolved physical reflectivity or transmissivity. One approach uses reflection imaging to sensitively detect the composition of features buried beneath an optically-thick aluminum layer, described in Shanblatt et al. [53]. The second approach describes using a direct measurement of the undiffracted beam to strongly constrain the probe, which enables reconstruction of periodic objects at high resolution, and decreases the number of iterations necessary for algorithmic convergence, described in Gardner et al. [86].

5.2 Absolute versus relative quantitative information

Computational imaging is generally always quantitative in some way. However, translating quantitative information into physically meaningful information is not always trivial. In CDI, the diffraction patterns are typically normalized during pre-processing. This results in the reconstructed amplitude being quantitative in terms of the *relative* transmissivities or reflectivities, but not in the *absolute* transmissivities or reflectivities. For instance, a reconstruction may show features with a reflectivity of 250% and a substrate of reflectivity 120%. While the ratio of these reconstructed relativities will be physically correct, the actual numbers themselves are clearly non-physical. For instance, the analysis shown in Fig 4.11 utilizes the ratio of reflectivities between the features

and substrate, because at that time quantitative CDI with absolute reflectivities had not yet been demonstrated.

In the EUV spectral range, transmissivity and reflectivity vary quite rapidly with wavelength as well as angle in the case of reflectivity, and therefore measuring these properties gives extraordinary chemical specificity. This chapter details recent work expanding ptychography CDI to do quantitative imaging of physical properties, which opens the door to exquisitely sensitive metrology of complicated, thick samples. The two related but distinct methods used to obtain absolute reflectivity and transmissivity information are Reconstructed Absolute Ptychographic Transmissivity/Reflectivity (RAPTR), first demonstrated in Ref. [53], and Modulus Enforced Probe (MEP), first demonstrated in Ref. [86]. RAPTR uses the total amount of counts available on the camera to normalize the ptychography iteration at each step, so that the reconstructed probe is in units of counts and the values on the amplitude of the reconstruction range between 0 and 1. MEP uses a direct measurement of the beam to improve the guess for the probe at every iteration, and by keeping the beam measurement in units of counts, automatically returns an object with amplitude ranging from 0 to 1, as well as a significantly faster converging probe guess.

5.3 Quantitative imaging of buried layers

This section is adapted from Shanblatt et al. [53].

5.3.1 Introduction and motivation

Probing and imaging reactions at interfaces buried beneath visibly opaque materials is critical for nanoscience and nanotechnology. In order to understand and optimize advanced functional nanomaterials for next-generation energy and nanoelectronic devices, it is important to determine the physical size and nature of interfaces, if they degrade over time, and how heat, charge, and spins move through different interfacial morphologies. However, most imaging modalities cannot be used for nondestructive, subsurface (> 50 nm) imaging [30]. Visible microscopy and atomic force microscopy (AFM) only image the surfaces of metallic samples. Back- scattered electron (BSE),

scanning electron microscopy (SEM), and secondary electron SEM with secondary electrons generated from backscattered electrons (SE-II) can image buried features using high electron energies to provide increased penetration depth [146]. However, these approaches also have limitations of decreased spatial resolution [147], charging of insulating samples, sample damage, and hydrocarbon buildup [29]. Furthermore, SEM often produces a complicated mixture of morphology and compositional information, making quantitative image analysis difficult. Moreover, for BSE-SEM, achieving elemental contrast for neighboring elements is often difficult because BSE efficiency is proportional to the natural logarithm of the atomic number [148].

Various specialized imaging techniques have been employed for probing buried interfaces. Mode-synthesizing AFM and scanning near-field ultrasound holography can detect subsurface structures [149, 150]. However, these techniques are not easily extended to dynamic imaging, which requires a fast imaging modality. Three-dimensional structures have also been probed using large-scale synchrotron X-ray diffraction microscopy in a transmission geometry [61, 151].

Short wavelength extreme ultraviolet (EUV) and soft X-ray beams have unique potential for imaging reactions at buried interfaces because they can penetrate visibly opaque materials, provide chemically specific contrast, and also image nanoscale features. In particular, by combining coherent beams from either high harmonic generation (HHG) [152] or X-ray free electron lasers (XFELs) [153] with coherent diffractive imaging (CDI) [3, 57–59, 154], it is now possible to achieve spatial resolutions that are comparable to the illuminating wavelength in the X-ray region for the first time [39,40]. Accordingly, CDI has found a range of applications in transmission and reflection geometries [137–139] to investigate nanoscale strain [155, 156], semiconductor structures [138], and for biological imaging [75, 76, 157, 158]. Because no optical elements are needed between the sample and detector, coherent diffractive imaging is the most photon-efficient form of imaging and can be nondestructive with no charging effects or resolution loss with depth [159]. Moreover, the contrast mechanisms in EUV CDI are relatively straightforward and intrinsically high: amplitude images exhibit high sensitivity to material composition, while phase images are exquisitely sensitive sensitive to both material composition and topography.

The work in this section demonstrates noninvasive, nondestructive imaging of the evolution of buried interfaces and reactions that occur at these interfaces using tabletop EUV CDI. Copper nanostructures inlaid in SiO_2 are coated with 100 nm of aluminum, which is opaque to visible light and thick enough that neither visible microscopy nor atomic force microscopy can image the buried interface. Short wavelength high harmonic beams can penetrate the aluminum layer, yielding high-contrast images of the buried metallic and insulating structures. Quantitative analysis shows that EUV light can not only detect but is extremely sensitive to multiple oxide layer formation as well as material interdiffusion that occurs at the $Al-Cu$ and $Al-SiO_2$ boundaries deep within the nanostructure at the few nanometers level. The presence of interdiffusion at the metal–metal interface is buried using destructive Auger electron spectroscopy (AES) sputter depth profiling.

Key to this new ability to nondestructively image buried interfaces is the use of ptychographic CDI, [73, 81, 160, 161], described in Chapter 2, which uses redundant information from multiple diffraction patterns recorded with overlapping fields of view to robustly reconstruct both the amplitude and phase of an object. Ptychographic CDI [81] has been implemented in a high-NA reflection geometry using HHG illumination [39, 40, 162] with the amplitude of the reconstructed images yielding the relative reflectivity (or transmissivity) between different regions of a sample. The results presented here required a modification of ptychography that returns absolute reflectivities simply by measuring the flux of the beam. This new approach called reconstructed absolute phase-diverse transmissivity/reflectivity CDI (RAPTR-CDI), allows nondestructive detection of the formation and evolution of interfacial diffusion and oxidation layers at the $Al-Cu$ and $Al-SiO_2$ boundaries.

5.3.2 Experiment

The experimental setup is illustrated in Figure 5.1. As described in Chapter 3 and Appendix B, bright, phase-matched, fully spatially coherent high harmonic beams [115, 117, 120, 152], were generated by focusing a Ti:sapphire laser beam (23 fs, 1.5 mJ, 785 nm pulses at 5 kHz) into a 5 cm long waveguide filled with argon gas at 49 Torr [120, 152]. Harmonics around the 27^{th} order

(29.1 nm) were reflected from two superpolished silicon substrates set at Brewster's angle to reflect the HHG beam while rejecting the residual laser light. Two 200 nm-thick Al filters were used to block any remaining fundamental laser light. The HHG beam was then passed through an iris to induce a hard edge on the beam incident on the sample. Two narrow-bandwidth multilayer mirrors set at 12° and 47.7° and with a bandpass of ≈ 1 nm were used to select the 29.1 nm harmonic light. An ellipsoidal mirror focused the HHG beam to a 16 μm diameter spot, which was incident on the sample at 57.8° from the normal. A 2048×2048 Princeton Instruments (PI-MTE) CCD, placed a distance of 3.85 cm downstream of the sample and normal to the undiffracted beam, was used to collect the light diffracted from the sample.

The two samples (provided by SEMATECH) imaged were cleaved from a damascene-style wafer consisting of copper structures inlaid in SiO_2 [161]. The copper structures were deposited by physical vapor deposition and patterned using I-line resist with a Canon GS22 followed by electroplating to reach a total height of 750 nm. Subsequently, 500 nm of SiO_2 was deposited using tetraethyl orthosilicate (TEOS).

The wafer was polished flat using chemical mechanical planarization (CMP). After exposure to atmospheric conditions for 14 months, repeating patterned cells were cleaved such that essentially identical areas of interest would be present on two samples. One sample was then coated with 100 nm of aluminum using an Edwards Cryo 304 electron-gun physical vapor deposition system, while the other was left uncoated for comparison. For both samples, the object and probe were computationally reconstructed using a combination of ptychography algorithms. The diffraction patterns were interpolated onto a linear spatial frequency grid using tilted plane correction [38,163] and then reconstructed with RAPTR-CDI, including position correction [82]. The multilayer mirrors allowed small amounts of adjacent harmonics to leak through, broadening the total fractional bandwidth of the illumination and degrading the fidelity of the reconstructions. For this reason, the corrected positions were next fed into a multicolor ptychographic information multiplexing algorithm [87], described in Chapter 4. By using this multicolor algorithm, noise due to the presence of adjacent harmonics could be filtered out so that only 29.1 nm light contributed to the reconstructed images.

The multicolor algorithm significantly improved the image fidelity over single color ptychography.

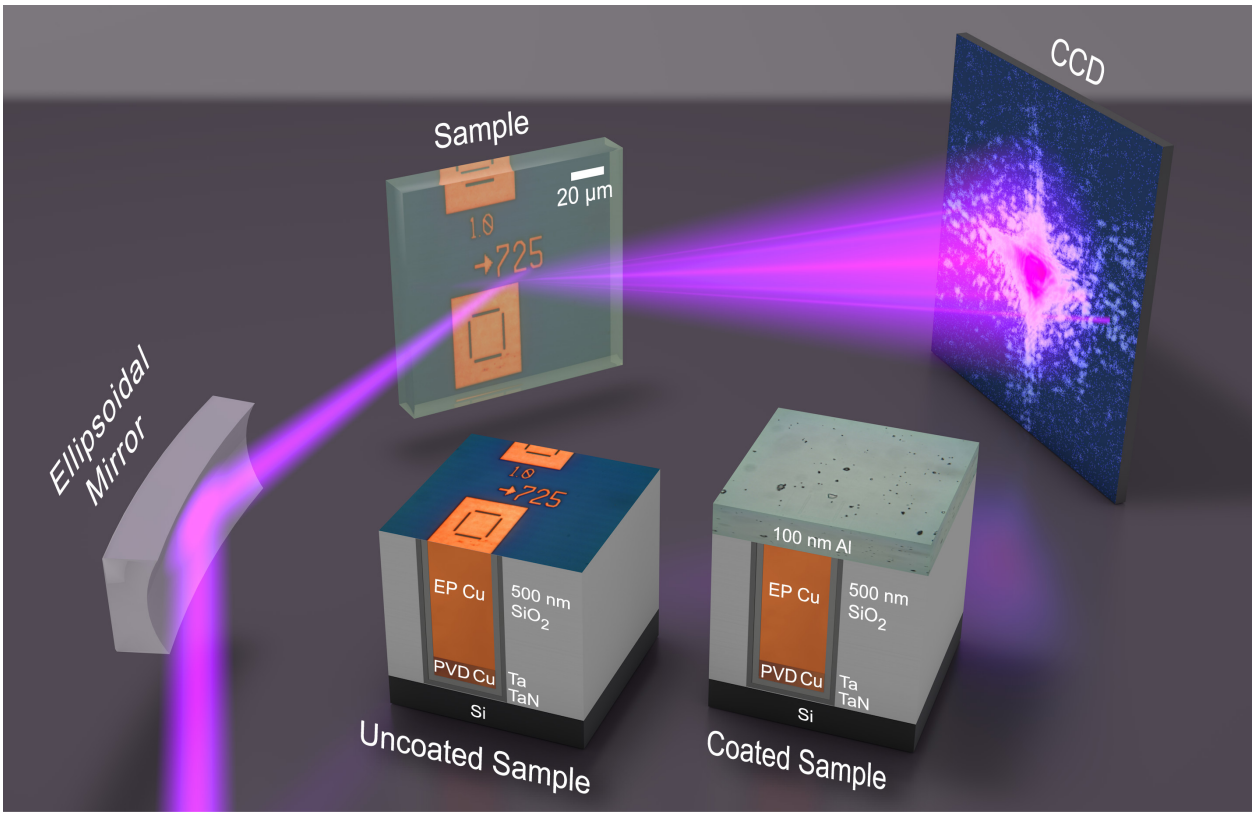

Figure 5.1: **Schematic of RAPTR-CDI**. The inset shows a diagram of the two samples imaged, topped with their visible microscope images. The tantalum was deposited by physical vapor deposition, and the top layer of copper was electroplated. Figure adapted from Ref. [53].

5.3.2.1 Absolute Reflectivity Information

In order to use RAPTR-CDI to characterize the absolute reflectivity of the buried metal-metal and metal-oxide interfaces at 29.1 nm, the flux of the HHG beam was measured before each ptychography scan. Images of the beam reflected from a gold mirror were recorded, and then used the exposure time and reflectivity of gold to calculate the number of available photons incident on the sample in units of detector counts. The reflectivity of the gold mirror was assumed to be 27.9% [42] with the surface roughness assumed to be that of sibling silicon substrates used in Refs. [39, 40]. Then, in RAPTR-CDI the probe is normalized to the measured power in each iteration. The absolute value squared of the complex amplitude of the reconstructed object is

therefore equal to the reflected intensity from the sample at every pixel. Because the sample reflectivity is spatially varying, masks for the features and substrates, as shown in Fig. 5.4 were used to select regions free from contamination. Then, the RAPTR-CDI reconstructions were segmented to allow calculation of the average absolute reflectivities reported in Fig. 5.7. The multicolor reconstructions were scaled such that the mean reflectivity of the masked regions agrees with that of the RAPTR-CDI images. The scaled multicolor reconstructions for both samples are shown in Figure 5.2.

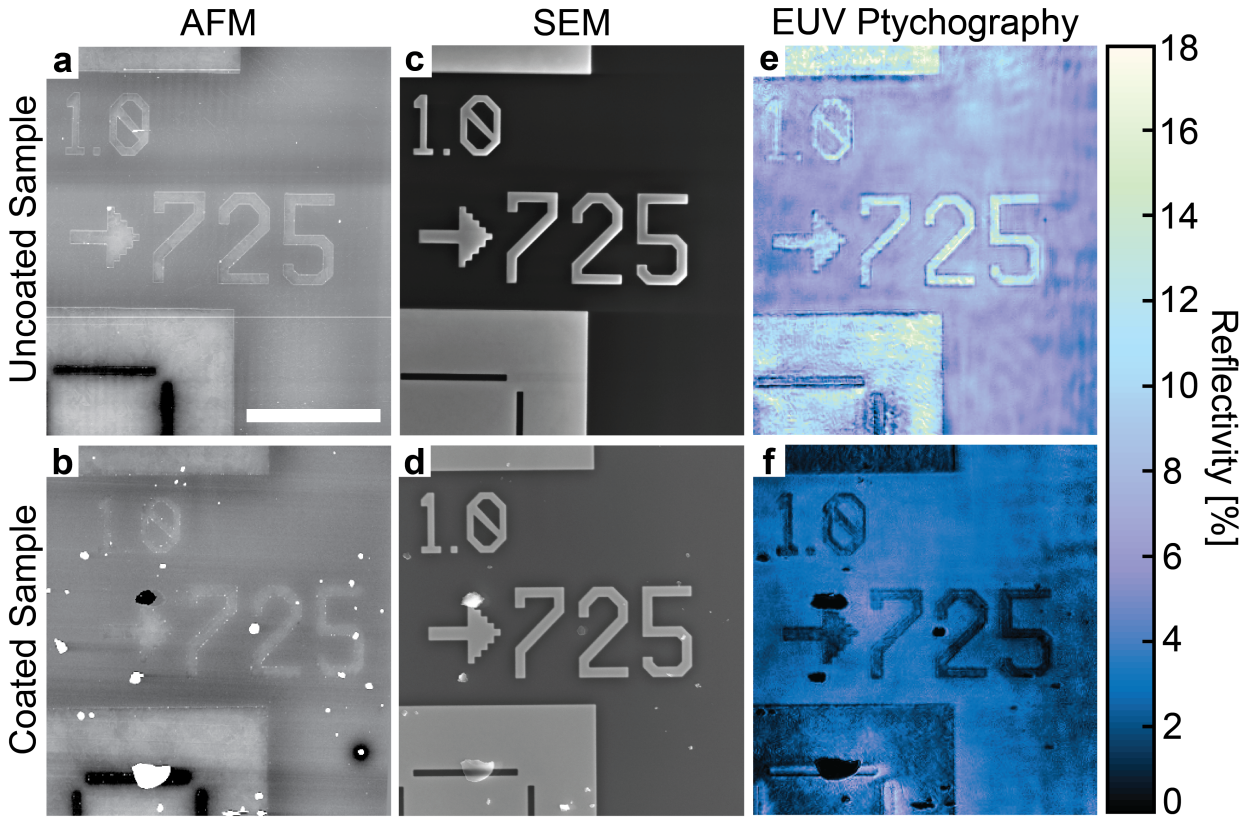

Figure 5.2: **Images of the uncoated and coated samples using different modalities**. Images of the uncoated (top row) and Al-coated sample (bottom row). AFM images with a 20 μm scale bar are shown in (a,b) with black corresponding to 0 nm height and white to 60 nm height. SEM images collected with a secondary electron detector at 18 kV are shown in (c,d). EUV ptychography images obtained with the multicolor refinement algorithm are shown in (e,f). The reconstructions are scaled to show absolute reflectivity based on the mean absolute reflectivity of the features and substrate in the RAPTR-CDI reconstructions. Figure adapted from Ref. [53].

5.3.2.2 Data Acquisition

For both samples, the ptychographic data set consisted of 270 diffraction patterns, collected with 3 μm step sizes between scan positions. A random offset of $\pm 20\%$ of the step size was added to each scan position to prevent periodic artifacts in the reconstructions [163]. The total EUV exposure time for the uncoated sample was 5.8 min, compared with 23.6 min for the aluminum-coated sample, with a total scanned area of 4270 μm^2 each. In future experiments, these exposure times can be reduced significantly ($> 100\times$) using optimized geometries and driving lasers.

5.3.2.3 Ptychographic Reconstructions

Each of the reconstructions were run first using RAPTR-CDI for an initial 50 iterations, with position correction [82] implemented for another 3000 iterations afterwards. The multicolor reconstructions were both run using the wavelengths of the 25^{th}, 27^{th}, and 29^{th} harmonics and for approximately 2000 iterations.

The transverse spatial resolution of the EUV images is limited by the effective numerical aperture (NA) of the imaging system. Because there are no optics between the sample and detector, the NA is determined by the distance from the sample to the detector ($z = 3.85$ cm) and the size of the detector (D). The diffraction patterns were cropped to 512×512 to reduce computation time, so the effective detector size, D_{eff} is $512 \times p$, with pixel size $p = 13.5$ μm square. Therefore, the NA is $D_{eff}/2z = 0.09$ and the diffraction limited resolution is $\lambda/(2NA) = 162$ nm.

The difference between the positions found using the position correction algorithm and the initial recorded positions were used to correctly determine the pixel size of the reconstructed images. This is necessary in general for ptychography CDI because any error in the measurement of the sample to detector distance or angle results in changes in the reconstructed pixel size. To solve for this change in the x and y directions, the difference between the corrected positions and the initial positions was fit to a plane. In particular, the scale factor necessary to correct the pixel size in the x-direction, a_x is $1/s_x$, where s_x is the slope of the plane fit to the position differences. Then,

$dx \cdot a_x$ is the corrected pixel size with dx being the predicted pixel size in the absence of tilted plane correction and any error in the measured detector-sample distance. It was found that after solving for the correct pixel size the scaling of the EUV reconstructions agreed well with the SEM measurements, whereas without this scaling the reconstructions were stretched by up to 18% in a given direction.

To correct for error in the XY-calibration of the AFM used for comparison to the HHG ptychography reconstructions, the AFM images in Figures 5.2 and 5.7 were scaled in the horizontal and vertical directions so that the transverse dimensions of the number "725" are in agreement with the SEM images shown in Figure 5.2.

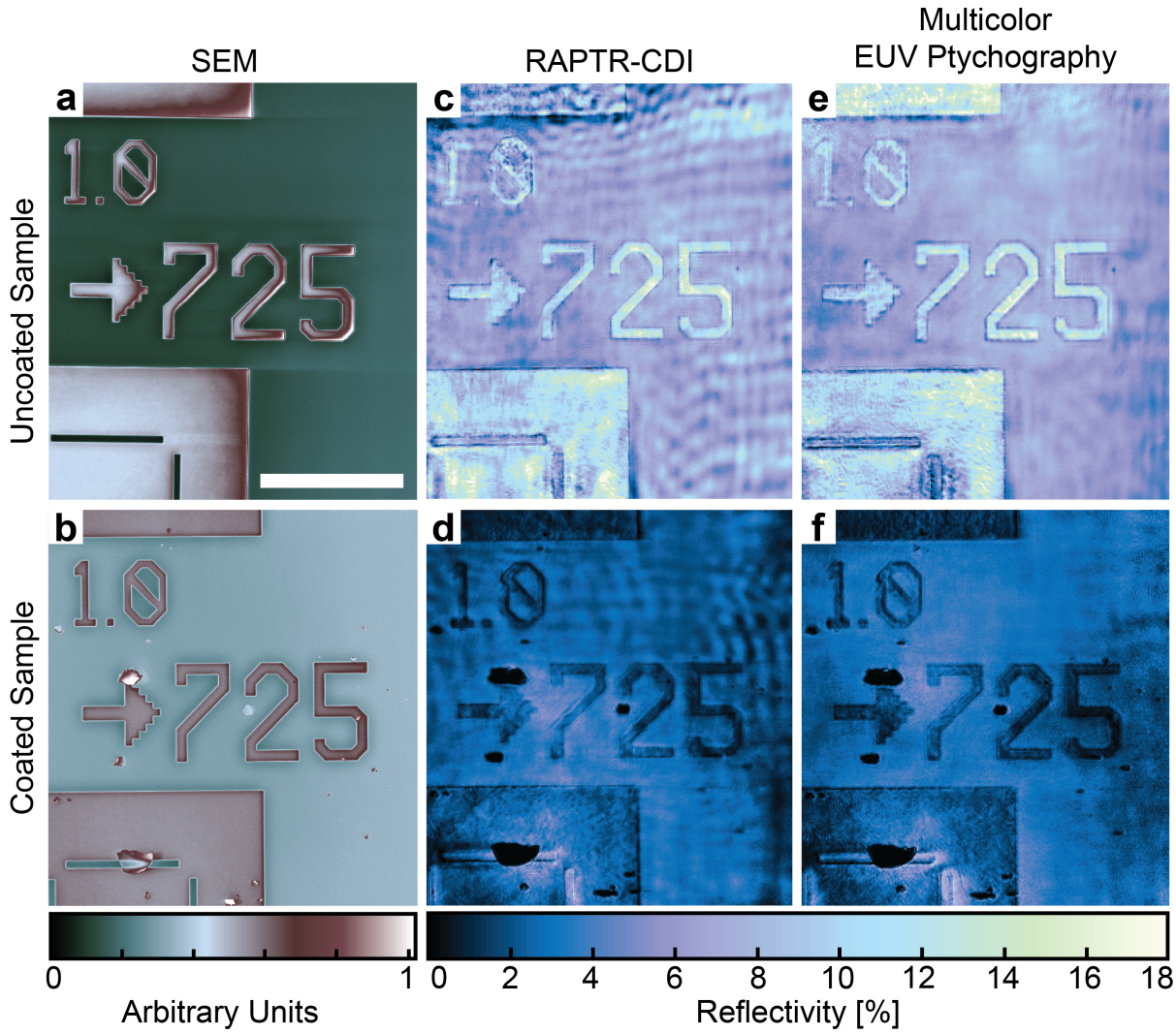

Figure 5.3: **Reconstructions with multi-color algorithm and single-color algorithm compared to SEM**. (a,b) SEM images for comparison. (c,d) RAPTR-CDI reconstructions, which return absolute reflectivity, but assume all diffraction is from exactly one harmonic. (e,f) Multicolor ptychography reconstructions demonstrating the enhanced fidelity provided by the multicolor algorithm. Because the multicolor algorithm only returns relative reflectivity, the reconstructions have been scaled such that their average reflectivity agrees with that of the RAPTR-CDI reconstructions. Scale bar is shared among all images and is 20 μm. Figure adapted from Ref. [53].

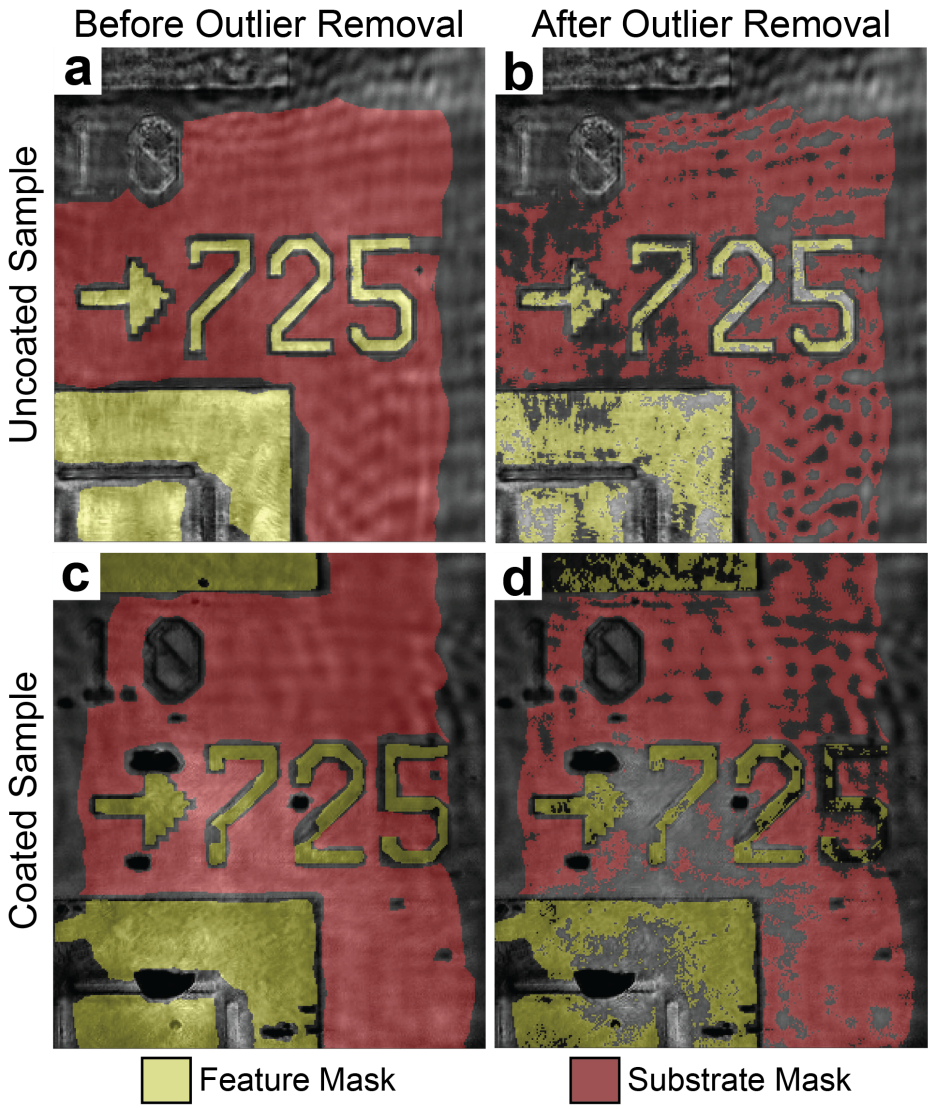

Figure 5.4: **Masks used to calculate the feature and substrate reflectivities**. Masks used to calculate the average feature reflectivity (yellow) and substrate reflectivity (red) for the uncoated (b) and coated (d) sample are shown in the right column. Masks (b) and (d) were generated from masks (a) and (c) by excluding points further than one standard deviation from the mean reflectivity of the included areas. Masks (a) and (c) were made using the intelligent scissors algorithm [164]. Masks (b) and (d) were used to scale the multicolor reconstructions so that their average reflectivity matches the RAPTR-CDI reconstructions [164]. Figure adapted from Ref. [53].

5.3.3 Chemically-specific imaging of buried interfaces

To highlight the extreme sensitivity of EUV light to interfacial reactions and chemical composition, the multicolor CDI amplitude images (which have been normalized to the measured RAPTR-CDI reflectivities) are compared to visible microscopy (Figure 5.1) as well as secondary electron SEM and AFM (Figure 5.2). The SEM (FEI Nova NanoSEM 630) with an Everhart-Thornley secondary electron detector and an accelerating voltage of 18 kV shows contrast on both samples (Figure 5.2c,d). The contrast on the coated sample is due to a combination of morphology on the surface of the aluminum as well as the chemical difference between the underlying features and substrate. This elemental contrast is detectable because the Everhart-Thornley detector also captures SE-II electrons generated from backscattered electrons reflected from the underlying structure [29]. This means that the coated SEM image includes a complex mixture of height and material information that is not easily decoupled.

The AFM (Digital Instruments MMAFM-2) only shows surface topography. The coated features are visible on the top surface because aluminum deposition is slow (0.5 nm, or approximately two atomic layers, per second), causing each layer to acquire the underlying topography. However, the AFMs accuracy in the vicinity of surface contamination is significantly degraded due to the much higher aspect ratio of the contamination than the nearly flat features. The EUV ptychography amplitude reconstruction (Figure 5.2) is the only image that definitively visualizes the buried interfaces, as confirmed by the amplitude contrast between the copper features and substrate. Indeed, if the EUV nanoscope were only imaging the top surface of the aluminum, then the absolute reflectivity image in Figure 5.2 would appear featureless and the reconstruction would be phase-only. Instead, EUV light penetrates through the Al to reveal the buried structures. Because the penetration depth of Al at 29.1 nm exceeds 400 nm, 80% of the light is transmitted through 100 nm of Al.

5.3.4 Quantitative detection of oxidation and diffusion at buried interfaces

In order to compare the experimental reflectivity measurements to the theoretical calculations, it is revealing to numerically modeled the multilayer stacks representative of both samples, including changes in the stacks resulting from oxidation and interdiffusion at all the interfaces (top and buried). The complex reflectivity of these stacks were then calculated. For these calculations, the methods used were derived from Ref. [141], which solve Maxwell's equations directly in the multilayer stack. These predictions were confirmed with IMD [140], a software program that uses the Fresnel equations to calculate the complex reflectivity for a stack of materials at EUV/X-ray wavelengths [165, 166]. The multilayer stack method and IMD agree to within 0.3% reflected intensity and 5° reflected phase, which would correspond to a 0.38 nm height difference in a height map (see Figure 5.7).

The four distinct areas, coated features, coated substrate, uncoated features, and uncoated substrate, are modeled as multilayer stacks with values for surface roughness, oxide layer thickness, composition, and interdiffusivity informed by AFM and AES, as discussed below. Modeling the propagation of light through these stacks returns a complex reflectivity coefficient. It is verified that the intensity matches our measured reflectivity, while the phase produces height maps consistent with the AFM, shown in Figure 4. Therefore, the modeled stacks have three constraints; the AES data, the reconstructed intensity, and the reconstructed phase.

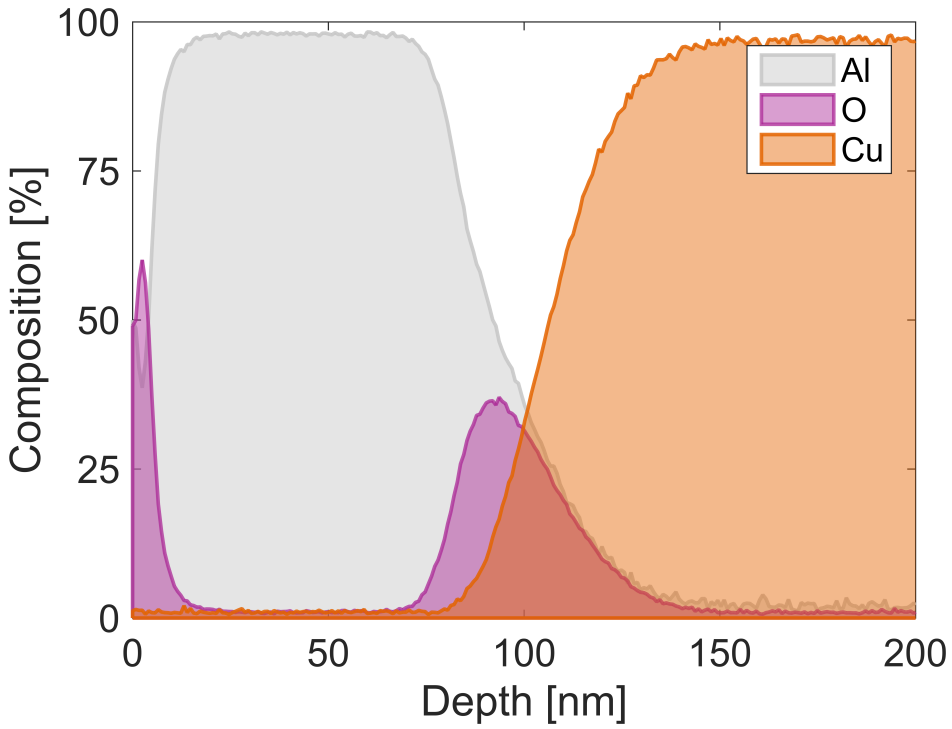

Figure 5.5: **Result of Auger electron spectroscopy sputter depth profiling on coated sample features**. Figure adapted from Ref. [53].

The results for the experimental versus modeled coated sample feature reflectivity are shown in Figure 5.8. Initially, a simple model was used consisting of 100 nm of aluminum deposited on the same stacks used for the uncoated sample. This model predicted that $R_{features} = 5.6\%$ and $R_{substrate} = 3.8\%$. However, these values are significantly higher than both of our experimental measurements (which were $R_{features} = 2.0\%$ and $R_{substrate} = 2.7\%$). Furthermore, the reconstruction displays a contrast inversion in the coated sample image, in which the coated Cu features are less reflective than the coated substrate, whereas they were more reflective in the uncoated sample (Fig. 5.2e,f) and in the simple model for the coated sample. Adding an Al_2O_3 layer on top of the aluminum layer could not resolve this contrast inversion, nor could assuming that the aluminum scavenged oxygen from the copper oxides to form Al_2O_3 at the interface, which is an energetically favorable reaction because $2Al + 3CuO \rightarrow Al_2O_3 + 3Cu$ corresponds to $\Delta_f H^\circ = 1207.52 kJ/mol$ [167].

The unexpected observation of this relative contrast inversion led to the hypothesis that diffusion occurred at the Al-Cu boundary, forming an interdiffusion layer that decreased the re-

flectivity at the interface (Fig. 5.7) [168]. The presence of this diffusion layer on the coated features was confirmed using AES sputter depth profiling, a destructive technique that requires ion sputtering through the sample to obtain Auger electron spectra at every relevant depth [169] (Figure 5.5). This technique revealed a 40 nm diffusive region at the interface. In the feature regions, calculations were performed for stoichiometrically plausible percent compositions for Al, Cu, Al_2O_3, CuO, and Cu_2O from the elemental composition provided by the AES at each depth.

Two diffusive models were tested, one in which Al_2O_3 is the only oxide at the Al-Cu interface and one in which there is a mixture of Al_2O_3, CuO, and Cu_2O at the interface. The model that assumes aluminum captures all of the oxygen from the copper oxides at the boundary fits well with the measured reflectivity (Fig. 5.7). For the coated substrate (Fig. 5.2e), the initial stack used was the same one as in the full model of the coated features for the top 50 nm of the sample (including a 3 nm diffusive Al_2O_3 layer at the surface), followed by an abrupt $Al - SiO_2$ interface at a depth corresponding to 100 nm of deposited Al. However, this resulted in a reflectivity twice as bright as was observe experimentally. This discrepancy was resolved by incorporating 26.5 nm of Al_2O_3 at the $Al - SiO_2$ interface with diffusion modeled by convolving the depth profile with a Gaussian of full width 6 nm. Because this Al_2O_3 layer corresponds to aluminum scavenging oxygen from SiO_2, the corresponding amount of liberated silicon in a layer below the Al_2O_3 was incorporated into the model. This modification produced agreement between the experimental reflectivity (2.66%) and the model (2.57%). It was intractable to experimentally confirm the presence of the diffusive Al_2O_3 layer at the interface because SiO_2 is non-conductive, preventing a reliable AES depth profile. However, there is experimental evidence in the literature indicating that aluminum can scavenge oxygen from SiO_2 when deposited via e-beam evaporation [170, 171].

To investigate how sensitive the reflectivity in the EUV spectral range is to interdiffusion of layers, the final coated sample stacks were modeled with the same amount of material as in the full model but without any diffusion (Fig. 3c,d). The theoretical reflectivities of these diffusionless models are shown by the red crosshatched bars in Fig. 5.7. The dramatic disagreement

with the measurements based on the reconstructions indicate that RAPTR- CDI is highly sensitive to diffusion. The final diffusive reflectivity models (green-striped bars) are compared to the experimentally measured reflectivities (gray bars) in Fig. 5.7. The uncertainty in the experimental measurement includes uncertainty in the gold mirror reflectivity and the standard deviation from the mean reflectivity due to spatial variation in the reconstructed reflectivity.

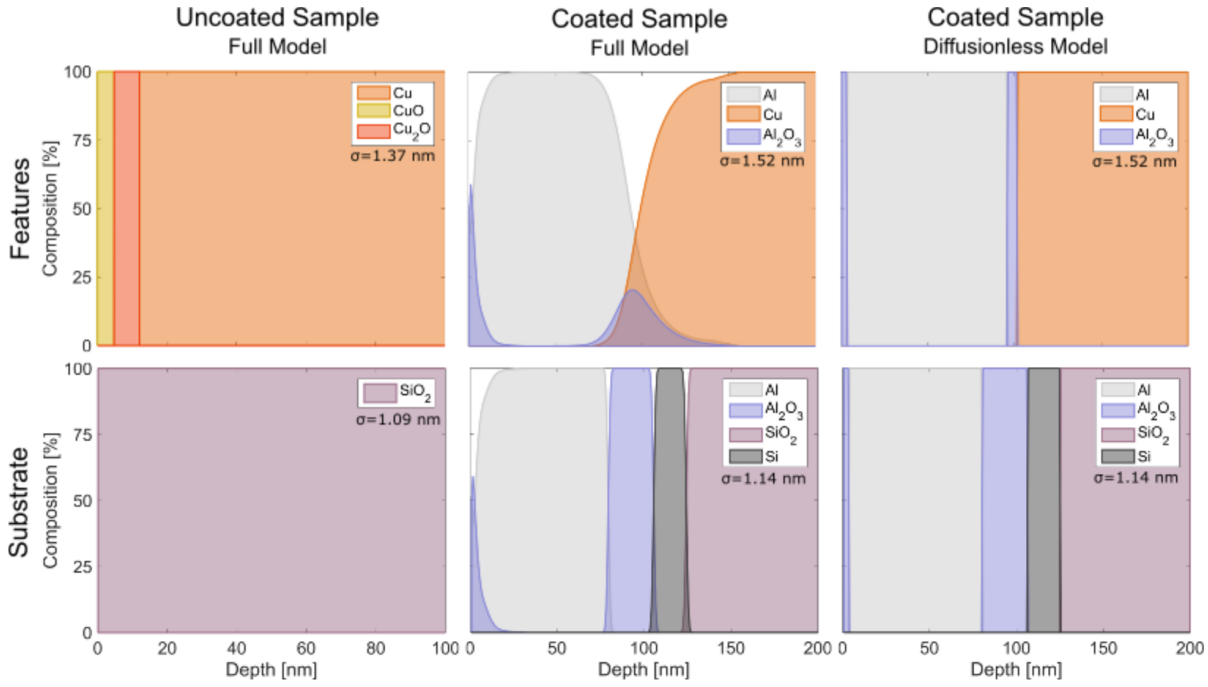

Figure 5.6: **Depth profiles used to model sample reflectivities**. Stacks used to model the reflectivity of different parts of the samples and their surface roughnesses. The top row shows the stacks corresponding to the features, and the bottom row shows stacks corresponding to the substrate. The full model for the features includes significant diffusion. Neglecting this diffusion (shown in the third column) predicts reflectivity values highly inconsistent with the experimental values for the reflectivities. Figure adapted from Ref. [53].

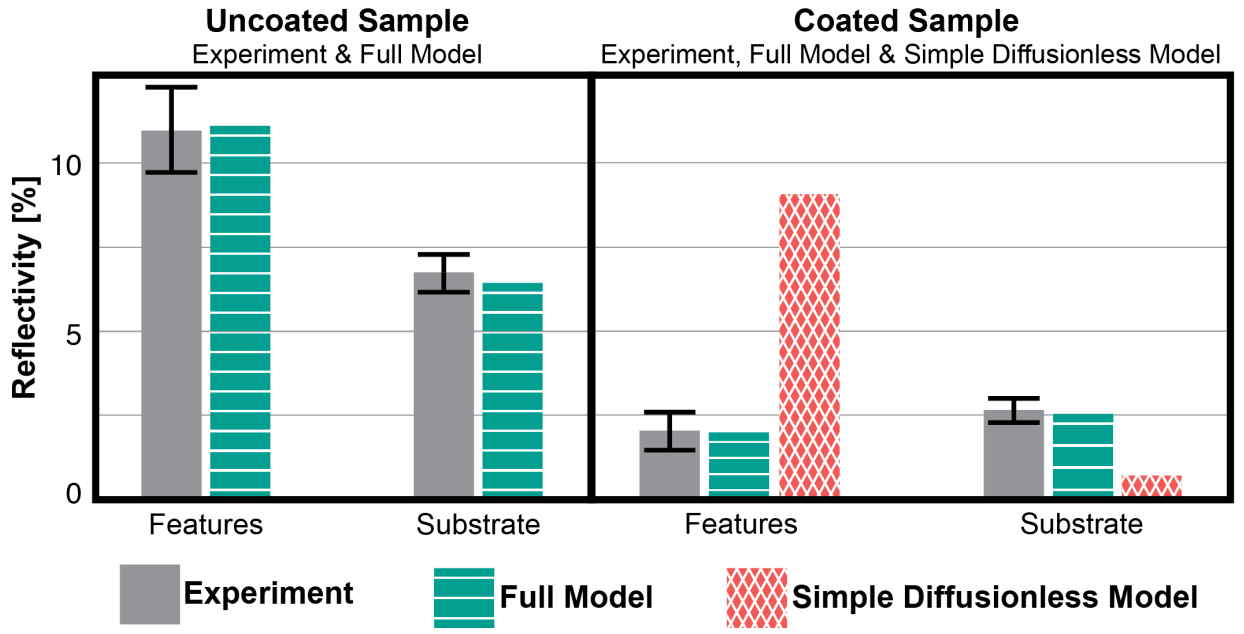

Figure 5.7: **Experimental versus modeled reflectivities**. Experimentally measured reflectivities compared to modeled reflectivities for the uncoated and Al-coated samples. For the coated sample, the green bars represent predictions by a model that includes diffusion, and the red bars represent predictions by a model with the same material quantities as those in the full model, but with no diffusion. Because the primary sources of uncertainty in these calculations arise from the oxide layer thicknesses, which are intrinsically difficult to quantify, error bars are omitted from the model results. Figure adapted from Ref. [53].

In the case of the uncoated sample, it was estimated that the copper features form a native oxide bilayer upon exposure to the atmosphere consisting of 4.8 nm CuO atop 7.4 nm Cu_2O, based on a study of copper oxide growth at ambient temperatures indicating a ratio of $0.65 = \mathrm{dCuO/dCu_2O}$ [172]. The model is displayed in Fig. 5.8. The total oxide thickness was calculated by assuming that the sample was polished flat during chemical mechanical planarization and the average feature height measured by the AFM is all due to oxide growth. This total thickness agrees with the amount of oxide indicated by the AES measurement of the coated features. In the uncoated sample model, the substrate is SiO_2 alone (Fig. 5.8). These relatively simple modeled stacks for the uncoated sample lead to agreement with the measured reflectivity of the uncoated sample (Fig. 5.8), providing a good check that the RAPTR algorithm produces accurate and reliable results.

5.3.4.1 Uncoated and Coated Sample Reflectivity Model Calculation

It is possible that a small amount of interdiffusion may occur between the copper and its oxide layers, but it was found that modeling diffusion by convolving the depth profile with a Gaussian having up to a 5 nm standard deviation did not significantly alter the theoretical reflectivity or phase.

	Features (%)	Substrate (%)
Experiment	10.97 ± 1.26	6.77 ± 0.61
Model	11.10	6.45

Table 5.1: **Reflectivity values of the uncoated sample**. Experimentally reconstructed mean reflectivity values (%) compared to modeled reflectivities of features and substrate on the uncoated sample. The error shown is the standard deviation from the mean of the reconstructed reflectivity in the masked regions.

	Features (%)	Substrate (%)
Experiment	2.04 ± 0.56	2.66 ± 0.35
Model	1.99	2.57

Table 5.2: **Reflectivity values of the coated sample**. Experimentally reconstructed mean reflectivity values (%) compared to modeled reflectivities of features and substrate on the coated sample. The error shown is the standard deviation from the mean of the reconstructed reflectivity in the masked regions.

5.3.5 High-resolution surface topography from phase reconstructions

In addition to the chemical composition discernible from the amplitude of the reconstructions (Fig. 5.2), the phase of the reconstructions contains both material and height information. By subtracting the phase of the complex reflectivity predicted by the modeled feature and substrate stacks from the reconstructed phase images, it is possible to generate height maps showing the surface topography of the samples, as described in Chapter 4 [39, 173]. In the case of the coated sample, the phase of the exit surface wave accounts for phase changes within the stack, and the height map therefore shows the top surface topography as opposed to the buried surface. These height maps are compared to AFM height maps in Figure 5.8. There is good agreement between

the height maps generated from ptychography and AFM, validating the RAPTR-CDI method for imaging buried nanostructures.

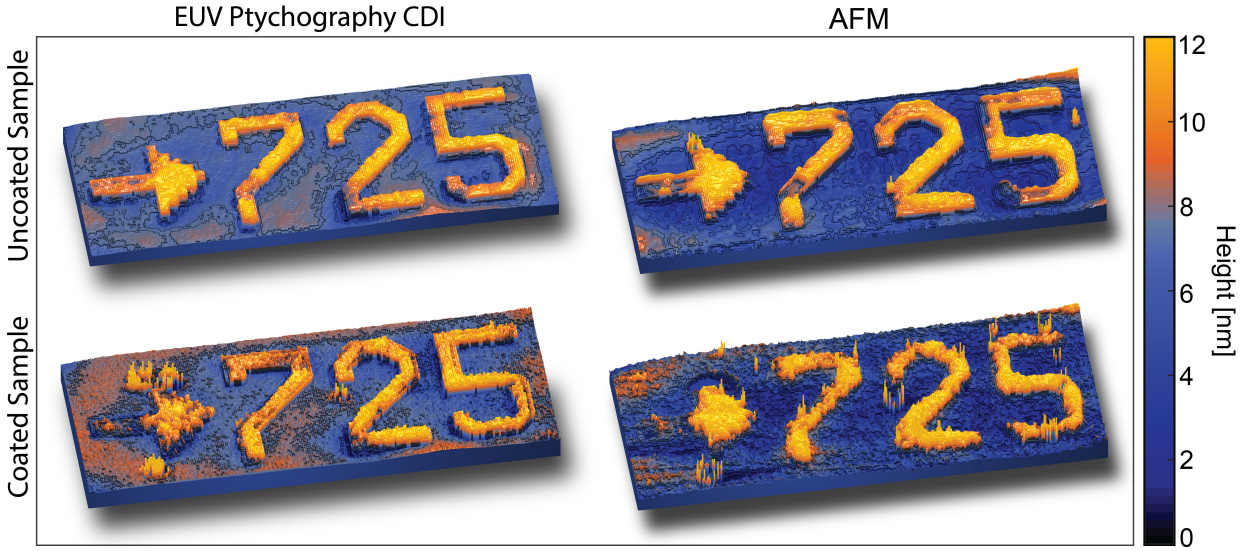

Figure 5.8: **Height maps for uncoated and coated samples based on ptychography CDI and AFM**. Height maps for the uncoated and Al-coated samples. Both the coated EUV and AFM images show high aspect-ratio artifacts where debris is located on the surface of the sample. Figure adapted from Ref. [53].

In the case of the uncoated sample, the model predicts the Fresnel phase shift due to the features is $-96°$, while the phase change from the substrate is $-65°$. In the case of the coated sample, the phase change from the features is $-92°$, while the phase change from the substrate is $-43°$. For plotting purposes, the AFM images have been smoothed with a Gaussian filter with full width equal to the EUV microscope's pixel size in the case of the coated sample and twice the EUV pixel size in the case of the uncoated sample (to remove a one pixel artifact in the image around the letters). Without smoothing, the AFM images appear noisy because the feature heights are similar to the surface roughness of the sample. Images were flattened using a 5^{th} order polynomial surface fit to decrease substrate height variations and make the feature heights more easily comparable. Binary masks used to assign Fresnel phases in the CDI reconstructions were generated using the intelligent scissors algorithm [164].

5.3.6 Conclusions

This work demonstrates a unique and powerful capability for quantitatively imaging the evolution of buried interfaces at the nanometer-level, with chemically specific contrast, through metal and oxide layers that are opaque to visible light, AFM, and SE-I SEM. This allows the nondestructive detection of the the evolution of interfacial diffusion and multiple oxidation layers between the aluminum coating and the buried copper structures and SiO_2 substrate. The findings are also validated using AFM, SEM, Auger electron spectroscopy, and values from the literature [172]. This work required the development of a new technique called RAPTR-CDI, which is a modified ptychography algorithm that yields absolute reflectivities or transmissivities by normalizing the probe at every iteration to the correct measured flux incident on the sample. This enables exquisite sensitivity to multiple interfaces simultaneously, even those buried deep within the sample.

5.4 Transmission imaging of periodic objects

This section is adapted from Gardner et al. [86].

5.4.1 Introduction

As is discussed in Chapter 1, the wavelength of an image is limited only by the system's numerical aperture. However, collecting diffracted light at a high numerical aperture is often difficult due to experimental and computational challenges. The work shown in this section demonstrates the highest wavelength-to-resolution ratio of any full-field CDI-based microscope image of an extended sample. This work also shows significantly increased fidelity of using CDI to image a nearly-periodic sample, which has previously been challenging due to the lack of diversity in a periodic sample's diffraction patterns [160, 174, 175]. This was achieved using an algorithmic improvement known as modulus enforced probe (MEP), which involves taking an additional measurement of the un-diffracted beam. MEP strongly constrains the probe, and therefore greatly helps with reconstructing periodic samples, and with reconstructing non-periodic samples as well. Furthermore, because the beam is measured directly on to the camera, the absolute transmissivity of the sample is retrieved, as in the case in RAPTR-CDI [53].

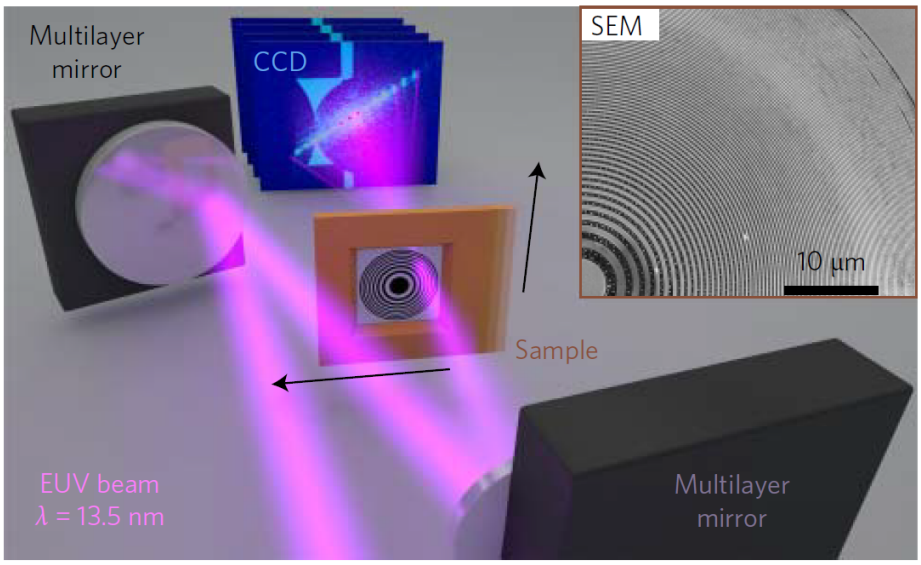

Figure 5.9: **CDI microscopy with modulus enforced probe**. Multilayer mirrors are used to select 13.5 nm light from a high harmonic source and focus it onto a sample. The scattered light is collected on a CCD. The inset shows an SEM image of the sample, which is a zone plate. Figure adapted from Ref. [86].

5.4.2 Experiment

The set up discussed in Chapter 3 and Appendix B was used to generate 13 nm light. The femtosecond 800 nm laser was focused into a helium-filled waveguide at around 1 atm of pressure (KMLabs XUUS 4.0). The light was reflected off of two Brewster-angle mirrors (Si coated with ZrO_2) followed by one 600-nm-thick Zr filter. A harmonic of wavelength of 13.5 ± 0.2nm was selected and focused onto the sample by a pair of Si/Mo multilayer mirrors, as shown in Fig. 5.9.

The sample used was a zone plate, and consisted of 150-nm-thick polymethylmethacrylate (PMMA) rings on a 50 nm silicon nitride window, was placed at the focus of the EUV beam. It was scanned in an array of 11×11 positions, separated by 0.88 ± 0.176 μm. The diffraction patterns were collected on a CCD 2.26 cm away from the sample. This diffracted light was detected at a nominal NA of 0.54. Here, the diffraction limited resolution is 12.5 nm.

5.4.3 Implementation of MEP

Although MEP can be achieved by using an image of the undiffracted beam, it can also be implemented by thresholding and then isolating the DC of the diffracted light. This approach was used in this work.

During the probe-update step of ptychography, the guess for the probe is propagated to the detector, and its amplitude is replaced with the measured probe amplitude, but the phase is kept. It is then propagated back to the sample plane. This is essentially the same method as the amplitude constraint step in CDI (discussed in Chapter 2), and can be implemented with error reduction, or other techniques such as RAAR or HIO [57]. The diagram of the algorithm is shown in Fig. 5.10.

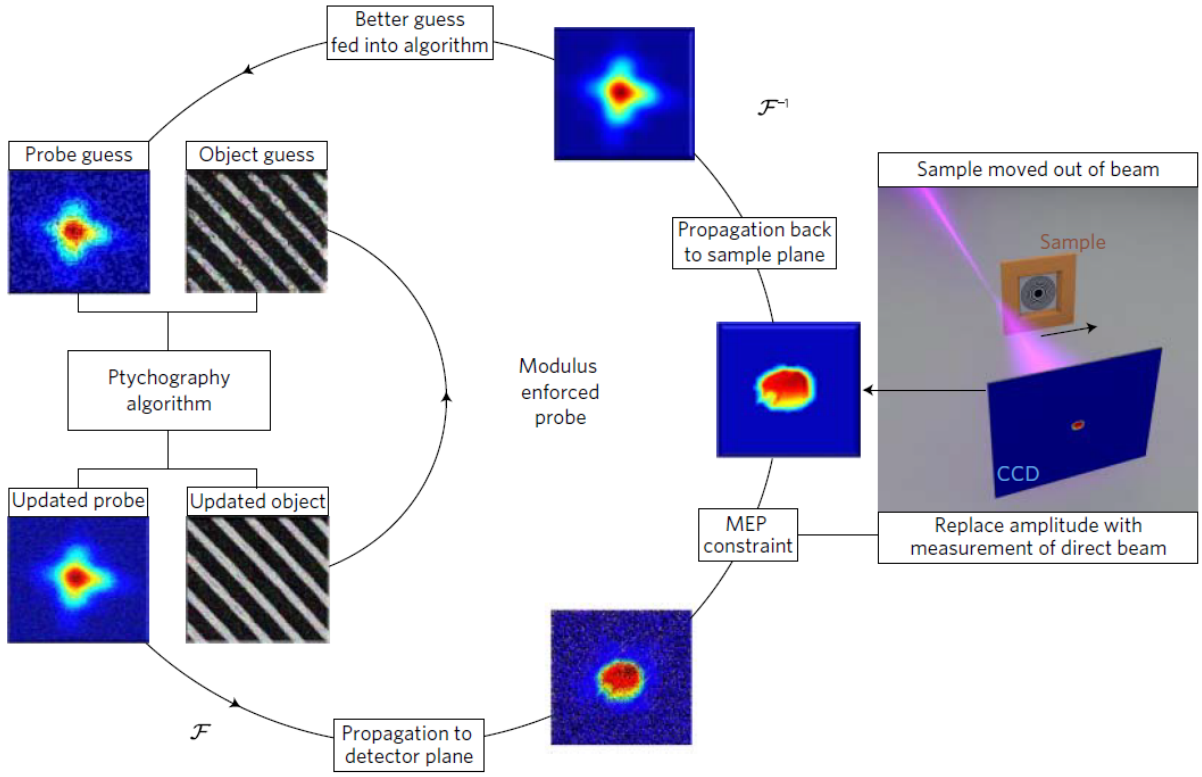

Figure 5.10: **Diagram of MEP ptychography**. Schematic of the ptychography algorithm with the added MEP constraint. First, a guess for the object and probe is constrained in Fourier space by the measured diffraction pattern. The updated probe is then constrained in Fourier space by the undiffracted beam data. The new probe is used in the next iteration, providing rapid improvement in algorithm convergence. Figure adapted from Ref. [86].

Using this methodology, ultra-high NA images of the nearly-periodic zone plate were reconstructed. These images are shown in Figs. 5.11 and 5.12.

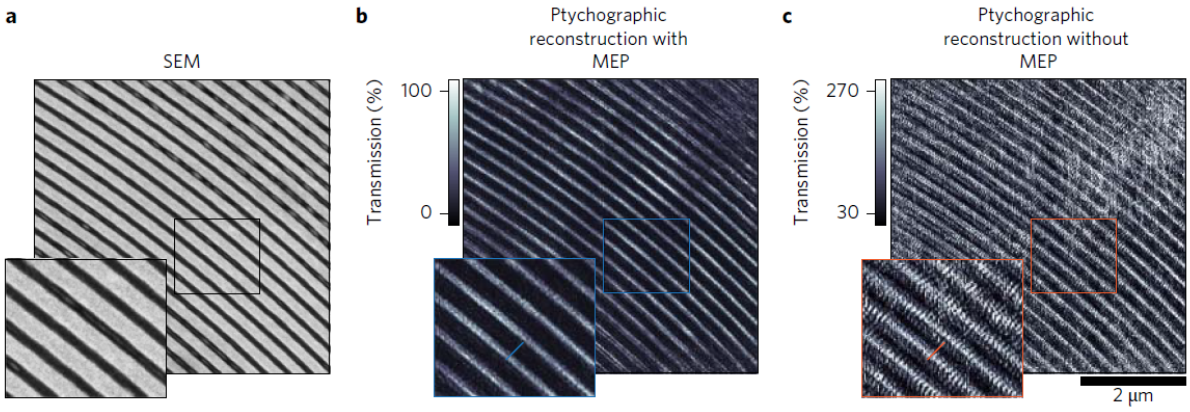

Figure 5.11: **Sub-wavelength full-field imaging of a zone plate**. (a) SEM image of the zone plate. (b) Ptychographic reconstructed amplitude, with the MEP constraint. The scale shows absolute transmissivity. (c) Ptychographic reconstructed amplitude without the MEP constraint. The scale is arbitrary, and the resolution and image quality are clearly not as good. The scale bar in (c) is shared among all images. Figure adapted from Ref. [86].

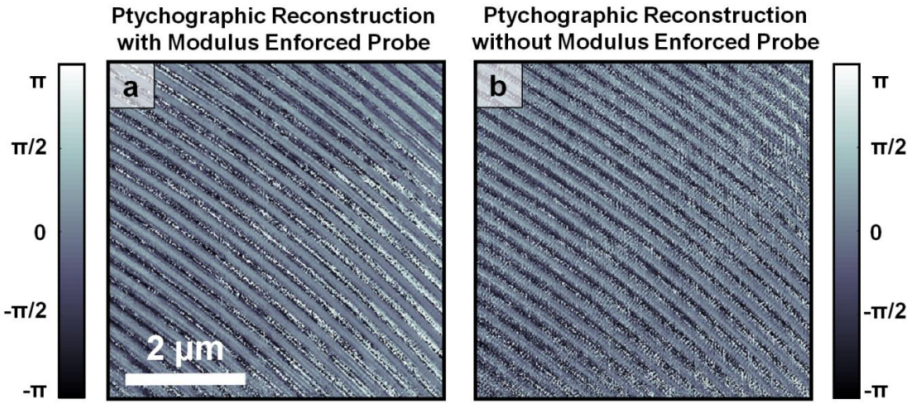

Figure 5.12: **Reconstructed phases of a zone plate with and without MEP**. Reconstructed ptychographic phases corresponding to the reconstructions shown in above. (a) Shows the reconstructed phase with MEP, and (b) shows the phase without MEP. Figure adapted from Ref. [86].

While the rings in a Fresnel zone plate are radially dependent (1/r), the reconstructed area shown in Figures 5.11 and 5.12 is 5.65×5.65 μm, while the zone plate has a radius of 40 μm. This means the field of view imaged is very close to being periodic. Ptychography's trouble with periodic

samples is very evident in the reconstructions that did not use MEP, and show up as noise and ringing artifacts in the reconstruction.

The insets in Figure 5.11 are zoomed in regions, showing eight PMMA zones of ≈ 110 nm separated by ≈ 90 nm. These regions of interest are compared via a 10%-90% lineout in Figure 5.13.

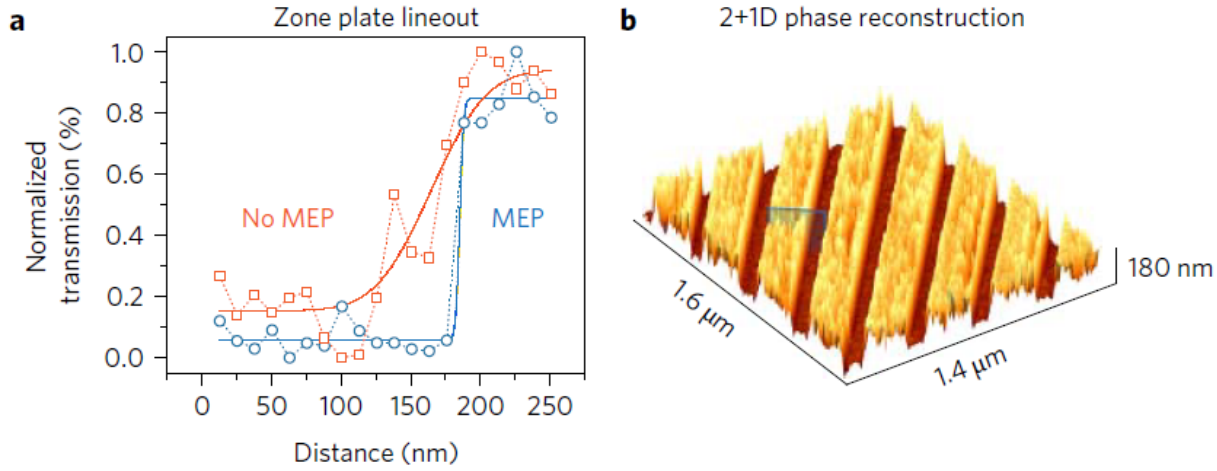

Figure 5.13: **Lineout of zone plate and height map**. (a) Lineout of a feature on the zone plate with MEP (blue) and without MEP (red). The boxes and circles represent the data, and the solid lines are fits of error functions. The lineout with MEP supports 12.6 nm resolution by the 10-90% knife-edge test. (b) Height map of the zone plate, with the vertical axis scaled by 0.2. The blue line shows where the lineout from (a) was taken. Figure adapted from Ref. [86].

As is evident from Figure 5.13, the MEP constraint enables much higher, diffraction-limited spatial resolution of a periodic object. This is because it decreases the cross-talk between the probe and object, and results in more fully deconvolved functions. The continuous, smooth probe shown in Figure 5.14(a)-(b) is clearly a more accurate physical representation of the probe. Furthermore, MEP constrains the total power in the exit surface wave, which does not allow power to oscillate between the probe and object during reconstruction. This results both in more stable reconstructions, and absolute physical transmissivity. Finally, the MEP constraint vastly improves convergence speed of the algorithm, particularly in the presence of a poor initial probe guess.

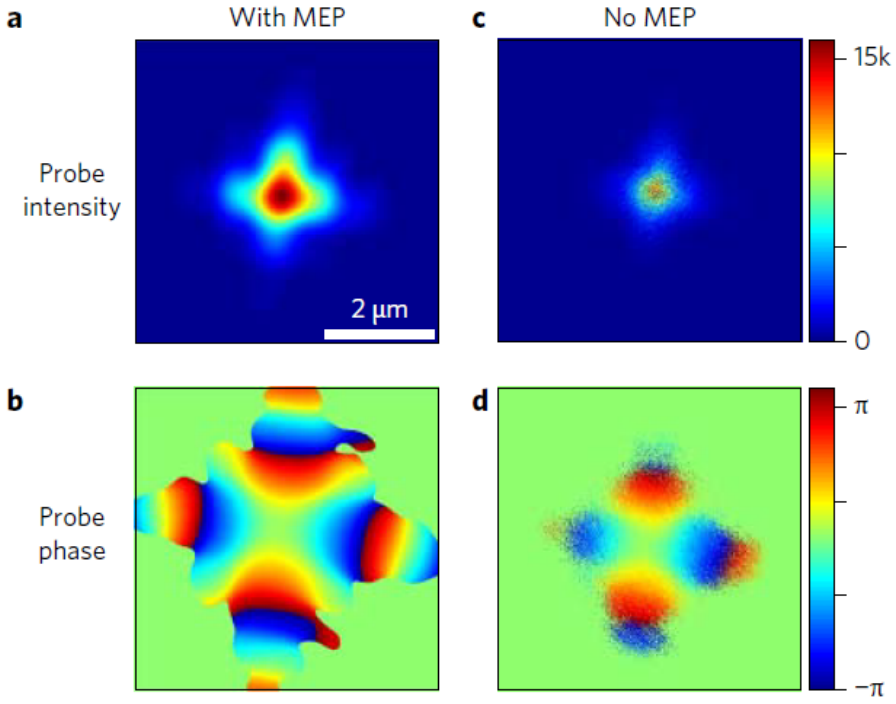

Figure 5.14: **Probes with and without MEP**. (a) Intensity and (b) phase of the probe with the MEP constraint, showing a smooth and continuous probe. The scale bar on the right is in counts measured on the detector. (c) and (d) show the amplitude and phase of the probe without MEP, and clearly is lower fidelity. The scale bar shown in (a) is shared among all panels. Figure adapted from Ref. [86].

5.4.4 Conclusions

This work shows a breakthrough in imaging periodic samples with a CDI microscope. It further demonstrates sub-wavelength imaging; a first for an EUV CDI microscope. Imaging at this resolution is important for the development of next-generation semiconductors and nano-engineered systems.

5.5 Outlook and impacts

Quantitative imaging with physical values remains difficult due to the required calibration of available illumination and a-priori knowledge of the sample composition. The new techniques of EUV RAPTR CDI and MEP CDI represent a path forward to retrieving physically meaningful

quantitative information while imaging with high-resolution, amplitude and phase contrast, and chemical-specificity.

There is great potential for future benefit in nanometrology and materials science using these techniques. For instance, this work can be extended by imaging interfacial charge, energy, and spin transport, examining the effect of increased temperature on interlayer diffusion, and using a comb of harmonics spanning an absorption edge to simultaneously image through multiple layers. Studying these physical properties will aid in the design of next-generation energy-efficient photovoltaics, thermoelectrics, and nanoelectronic devices. RAPTR-CDI also opens the door to fully quantitative material characterization combined with EUV imaging, that is, imaging reflectometry, by performing angle-resolved measurements with the sample placed on a tilt stage. This would allow for highly sensitive metrology of thick samples inaccessible to visible ellipsometry.

These techniques could further be extended to perform high-throughput buried layer imaging of periodic samples by using multiple EUV beams to achieve a wide field of view [60, 87], and MEP can significantly benefit established CDI techniques such as upsampling [87, 176]. This technique is also beneficial to imaging thick samples in 3D [177, 178], as is discussed in detail in Chapter 6.

In the future, this technique coupled with the fast temporal resolution of high harmonics can be harnessed for imaging dynamically functioning interfaces [179]. The improved algorithmic convergence speed enabled by MEP will be of immense help toward real-time imaging.

Chapter 6

CDI in Three Dimensions

Thus far, all of the images shown in this thesis has been two-dimensional. Though some of the samples have had multiple layers of interest, the reconstruction technique itself fundamentally assumes a projection of the sample. While many samples are validly represented under this kind of approximation, thick samples, particularly those that have variation along the third dimension, are not. An entire class of biological, high-aspect ratio semiconductor, and other types of samples have interesting information in three dimensions.

The most well-known three dimensional imaging technique is X-ray tomography. It has been in widespread use in medicine for many years, and has become indispensable for many diagnostic and therapeutic tools [180, 181]. However, tomography typically only recovers amplitude information, as the sources used are incoherent. It also often requires a high dose of ionization radiation, making it unsuitable for certain types of radiation-sensitive samples.

Recently, EUV/X-ray CDI microscopy methods have been extended to three dimensions. These techniques often use illumination with high penetrating power, and by using coherent diffraction techniques are capable of retrieving the phase of the sample. Generally, there are four techniques currently in use which use some combination of isolated object CDI (ioCDI), tomography, and ptychography. I discuss these techniques in detail, and demonstrate first-of-its-kind preliminary results of three-dimensional imaging with our tabletop EUV microscope.

6.1 Introduction and approximations

The Born approximation and Ewald sphere discussion from Chapter 1 are very relevant to the material presented in this chapter. In addition, a few more approximations and theorems will be discussed.

6.1.1 Projection approximation and multiple scattering

The projection approximation states that a sample's output exit surface wave (ESW) will be equal to the input wave times a two-dimensional transmissivity (or reflectivity) function $t(x, y)$ (or $r(x, y)$), which are allowed to be complex:

$$E_{ESW}(x, y) = E_{in}(x, y) \cdot t(x, y). \tag{6.1}$$

In this approximation, the sample is treated as infinitely thin. While many samples can reasonably satisfy this approximation, for instance if there is no diversity in the sample along the optical axis and the diffraction of light within the sample is negligible. However, the need to satisfy this approximation inevitably limits the study of thick, real-world samples.

Another issue arises for imaging thick samples: multiple scattering events. Two-dimensional CDI and ptychography do not treat propagation and multiple scattering within the sample, and while high energy hard X-ray photons may penetrate a sample without diffracting significantly, multiple scattering becomes more important for longer-wavelength EUV light.

6.1.2 Fourier slice theorem

Central to two-dimensional CDI is the Fourier slice theorem, which states that for a sample under the projection approximation, the 3D Fourier transform is identical at every slice through the k_0 axis. By collecting 2D diffraction data, the assumption is that the data would look the same if it were produced by any infinitesimal slice within the sample. Thus, by collecting 2D diffraction data, the object's full 3D Fourier transform could be built in diffraction space slice by slice.

6.1.3 Probe-object factorization

In ptychography, another central assumption is that probe-object factorization is preserved. That is, if the sample were taken out of the way, the probe should not significantly diffract between the start and end of the sample's extent. This limits sample thickness to much, much less than the Rayleigh range of the beam, depending upon the type of beam (Gaussian, Bessel, etc.) and its phase (quadratic, hyperbolic, topologically charged, etc.).

In Ref. [45], the approximation is derived that the validity for a thickness of a sample under probe-object factorization is

$$T \ll \frac{Ra}{\lambda} \tag{6.2}$$

where R is the system's resolution, a is the diameter of the probe, and λ is the illuminating wavelength. For a system with 13 nm illumination, a 5 μm spot size, and an NA of 0.25, (order-of-magnitude typical parameters for work done in this thesis), this limits the sample thickness to 10 μm. A calculation done in Ref. [182] based on Ewald sphere constructions suggest that the thickness limit should instead be

$$T \leq \frac{R^2}{\lambda} \tag{6.3}$$

which for the system discussed above limits the sample thickness to about 100 nm, which is quite thin.

This suggests that an important obstacle to overcome for 3D imaging of thick samples will be to find reconstructions techniques that *do not* require probe-object factorization to be satisfied. Probe-object factorization is also an important consideration when imaging objects in 2D.

6.2 Approaches for imaging in 3D with diffractive EUV/X-ray microscopy

Three dimensional imaging is an important subject to many areas of science. Diffraction-based 3D techniques have been demonstrated since the early 2000's, and methods have used extensions of ioCDI as well as ptychographic methods. Non-phase retrieval techniques are important as

well, such as diffraction tomography, where filtered back projection is replaced by back propagation [183] and STXM tomography [184], as well as techniques demonstrated with an SEM [185,186].

6.2.1 Bragg CDI and symmetry-based approaches

Bragg CDI, which uses diffraction from a crystal lattice, has been demonstrated in 3D on gold nanocrystals [68]. Recently, an ioCDI experiment that utilized crystal symmetry to gain 3D diffraction information was able to obtain a high-resolution 3D reconstruction from a single shot [187]. Another technique, 3D Bragg projection ptychography, was able to measure strain in a semiconductor structure [188] and crystal lattice distortions in a nanoelectronic device [189].

6.2.2 Isolated object-based methods

Isolated object CDI algorithms can be extended to three dimensions using a number of methods. While these methods do suffer from the limitations arising from the isolation requirement, they do all have the advantage of requiring less data acquisition. This in turn makes them good options for high-throughput or near-real-time imaging, as well as for samples that are damaged by significant amounts of radiation.

6.2.2.1 Ankylography

Ankylography is a method of 3D imaging capable of reconstructing an image from a single diffraction pattern. By interpolating the diffraction pattern onto an Ewald sphere in 3D Fourier space and letting the algorihm solve for the missing data, objects have been successfully reconstructed [52, 190]. However, the objects imaged were fairly thin and reasonably valid under the projection approximation, so concerns were raised about the thickness of objects which could be reconstructed with this method, as well as the uniqueness of the solution [191]. More recently, ankylography, which is inherently sparse, has been successfully used to determine molecular structure with a sparsity-based algorithm [192]. A significant advantage of ankylography is that it has the potential to be used for single-shot imaging, which is of critical importance for imaging biological

specimens that may be damaged by radiation.

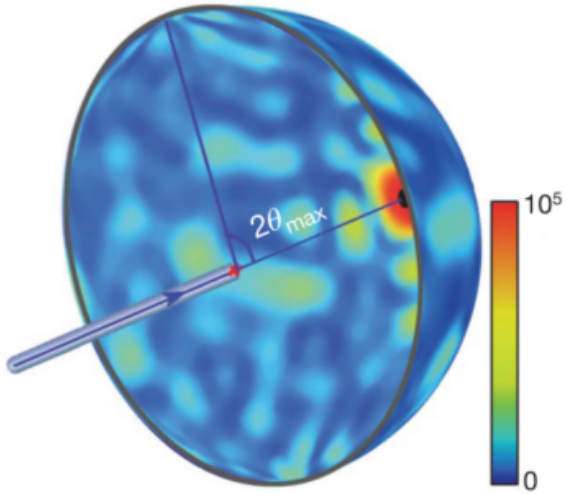

Figure 6.1: **Schematic of Ewald sphere diffraction used for ankylography**. Schematic showing Ewald sphere diffraction for ankylography. Light is scattered off an object at the center and diffracts outward to the shape of the Ewald sphere for a given NA. Figure adapted from Ref. [190].

6.2.2.2 Three-dimensional ioCDI

A method somewhat similar to ankylography, but that uses many diffraction patterns, is 3D ioCDI. The Fourier slice theorem states that the Fourier transform of a 2D projection of a 3D object in real space is equal to a slice through the 3D Fourier transform of that same object. Therefore, by rotating the sample and collecting many diffraction patterns, more of the 3D Fourier transform cube can be filled in, and less missing data needs to be solved for algorithmically. In some cases, the diffraction patterns are interpolated onto the Ewald sphere- depending on the wavelength and numerical aperture of the experiment. This technique was first demonstrated with test samples by Miao et al. in 2002 [193] and Chapman et al. in 2006 [70], and was later used to image human chromosomes [194]. It has also been used to image a giant mimivirus [195] and frozen yeast cells [61].

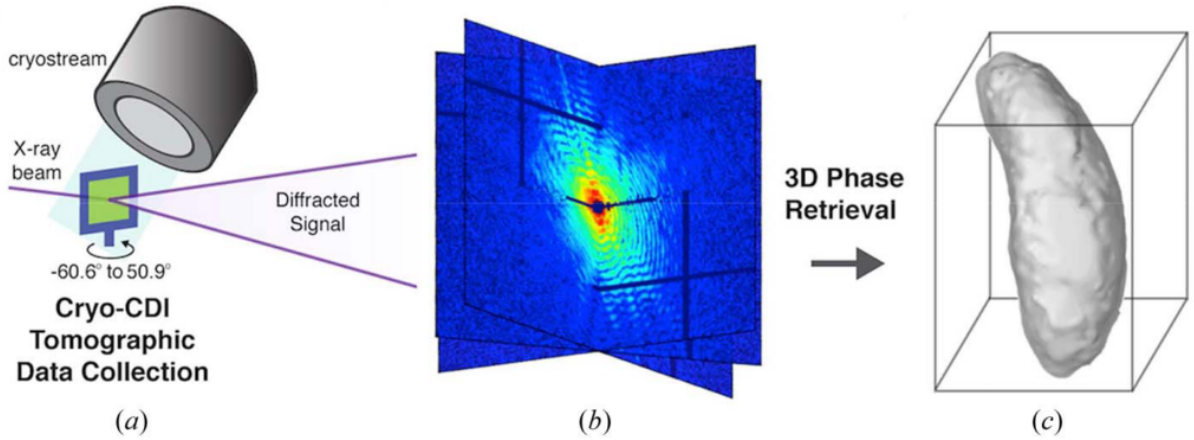

Figure 6.2: **Schematic of 3D ioCDI**. Schematic showing steps between data acquisition, phase retrieval, and reconstruction. Figure adapted from Ref. [61].

While this method is good for dose reduction, it does not have the information redundancy of ptychography- making it somewhat less robust, in addition to the limitation of needing an isolated sample. However, for samples that are properly isolated, it has proven to yield high-resolution, high-fidelity images.

6.2.2.3 Tomographic ioCDI

Like 3D ioCDI, tomographic ioCDI involves taking diffraction patterns of an isolated object at different angles. The difference in algorithms is that 2D phase retrieval is run individually on these diffraction patterns, resulting in complex reconstructions of the object's projection at different angles. These projections are then combined tomographically, using techniques such as equally sloped tomography (EST) [196], filtered back projection (FBP), or other tomographic reconstruction methods.

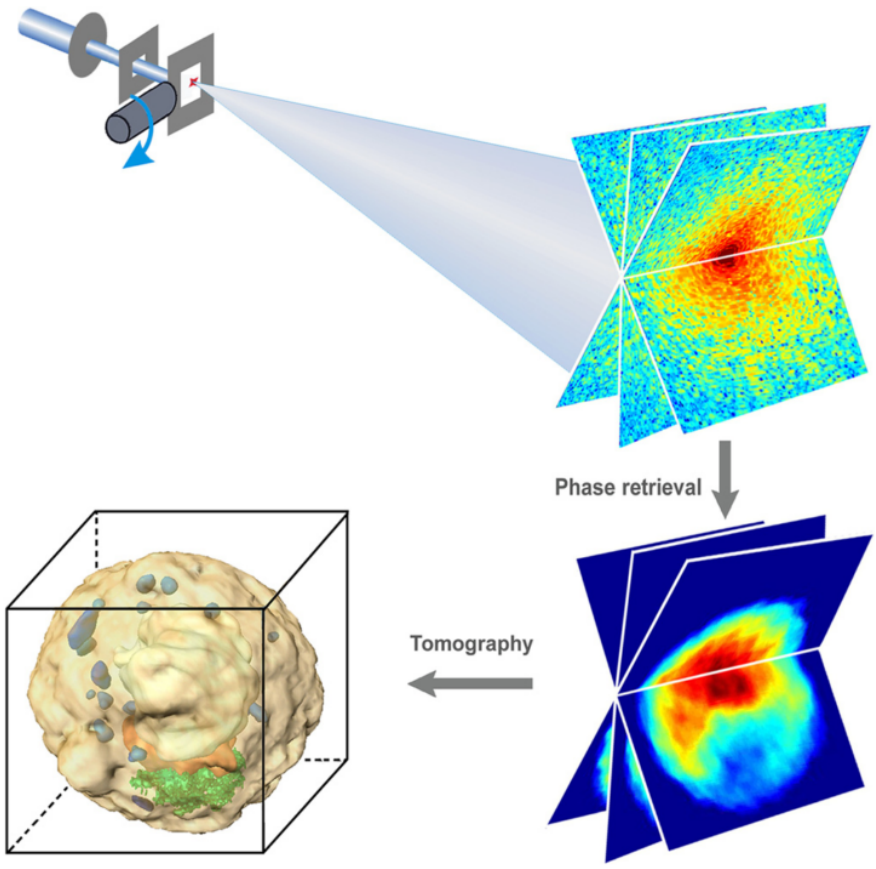

Figure 6.3: **Schematic of CDI tomography**. Schematic showing steps between data acquisition, phase retrieval, and reconstruction. Figure adapted from Ref. [74].

Using light from facility sources, high-resolution 3D images of adenocarcinoma cells [197] and crygenically frozen yeast spores have been obtained [74]. It is often difficult in these types of experimental geometries to measure enough angles to perform FBP tomography, so EST, which better handles a smaller number of angles, is often used in these cases. Algorithms improving alignment and reconstruction of phase projections [198] have also led to algorithmic improvements that account for ambiguities due to phase unwrapping. Tomographic ioCDI has been used in hybrid imaging techniques as well; portions of mammalian cells have been imaged in combination with optical fluorescence microscopy [199].

Much like 3D ioCDI, this technique is relatively low-dose, but suffers from limitations due to the isolated sample requirements.

6.2.3 Ptychography-based methods

As ptychography has grown increasingly popular in recent years, it has been applied to a wide variety of 3D problems. These techniques tend to be very robust, as they utilize the information redundancy available in ptychography– but generally require more flux and therefore higher doses than other methods.

6.2.3.1 Ptychographic tomography

Ptychographic tomography (sometimes called ptycho-tomography) is likely the most robust, though it is also the most photon-intensive technique. This technique involves taking full ptychography scans at many different angles of rotation of a sample, and combining the projections with tomographic methods. Unlike tomographic ioCDI, this method readily accommodates extended samples.

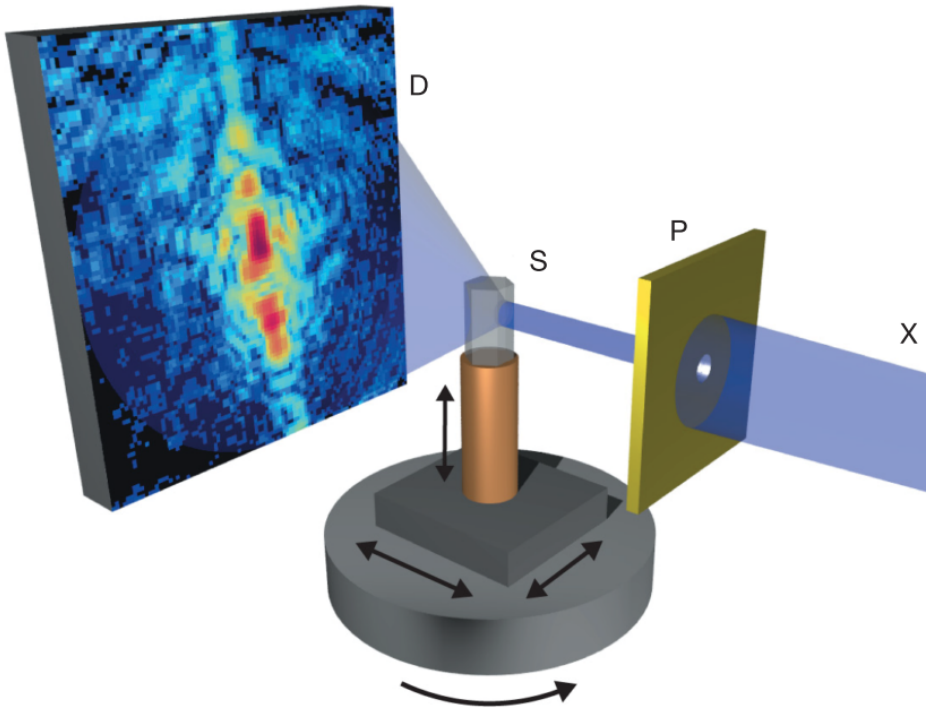

Figure 6.4: **Schematic of ptychographic tomography**. The set-up includes X-rays (X) impinging on pinhole (P), scattering from a sample (S), which is mounted on a 3D stage on top of a rotation stage, after which the scatter is collected on a detector (D). Figure adapted from Ref. [200].

Ptycho-tomography has been employed successfully in facility-scale sources to image a variety of samples such as inner bone structures [200], nanoporous glass [201], cells inside a capillary [202, 203], and cryogenically-cooled cells [204]. More recently, this technique has been used to image a cobalt-coated Buckyball-like scaffold, with elementally-specific contrast gained from reconstructing tomograms at and below the cobalt K-edge [205]. High-resolution, elementally-specific 3D imaging has also been done on a 3D integrated circuit [206]. Hybrd techniques have also been established that are capable of obtaining high-resolution interior tomograms on a region of interest within a larger sample [207]. Extensions of near-field ptychography– which allows imaging of strongly absorbing samples– to this technique have been realized [208].

6.2.4 Three-dimensional multislice ptychography

The redundant information in ptychography has been utilized in various ways beyond reconstruction robustness. Ptychographic deconvolutions have been extended to retrieve images with different mutually incoherent modes [53, 60, 85, 87, 145], correct for errors in positions, wavelength, and sample-detector distance [82], and allow for super-resolution imaging [88], and upsampling of undersampled data [87].

Another use of ptychography's rich information redundancy has been realized with a technique known as multislice ptychography (or "3PIE") [177, 178], a technique which propagates the exit surface wave axially and solves for the object at various slices. A significant advantage of this technique is that it does not require any additional measurements such as rotating the sample, meaning that a traditional ptychographic data set can be used with the algorithm. The multislice ptychography algorithm is described next, following along from Maiden et al. 2012 [177]:

As in traditional ptychography, at a given position j, the spatial object $O_j(\mathbf{r})$ and probe $P(\mathbf{r} - \mathbf{R}_j)$ are multiplied together to form the exit surface wave (ESW) $\psi_j(\mathbf{r})$. For clarity, the description here will omit the subscript j (except for the amplitude constraint), but it is implicitly assumed that each sub-iteration is for a single ptychographic position.

Now, at each plane k, with N planes total, there exists an input surface wave $\psi_{i,k}(\mathbf{r})$, an

object function $O_k(\mathbf{r})$, and an exit surface wave $\psi_{e,k}(\mathbf{r}) = \psi_{i,k}(\mathbf{r}) \cdot O_k(\mathbf{r})$. Planes are separated by distances Δz_k.

The first input surface wave is the probe. So the first exit surface wave is simply formed by

$$\psi_{e,1}(\mathbf{r}) = O_1(\mathbf{r}) \cdot P(\mathbf{r} - \mathbf{R}_j) \tag{6.4}$$

where $P(\mathbf{r} - \mathbf{R}_j)$ represents the probe function shifted to the particular position $\mathbf{R}_j$.

Next, the exit surface wave is propagated to slice 2 (or slice $k+1$ in general), using the spectrum of plane waves propagator $\mathscr{P}$ by the plane separation distance Δz_k, in this case Δz_1.

$$\psi_{i,2}(\mathbf{r}) = \mathscr{P}_{\Delta z_1}\big\{\psi_{e,1}(\mathbf{r})\big\}. \tag{6.5}$$

As before, this input surface wave is multiplied by the object at that plane to from the exit surface wave at that plane,

$$\psi_{e,2} = O_2(\mathbf{r}) \cdot \psi_{i,2}(\mathbf{r}) \tag{6.6}$$

and so on until the ESW at the final plane, $\psi_{e,N}(\mathbf{r})$ has been obtained. The amplitude constraint, requiring that the amplitude of the final ESW's Fourier transform be equal to the experimentally measured amplitude $\sqrt{I_j(\mathbf{u})}$ for this particular position j, is then applied to the diffraction pattern at the detector plane,

$$\Psi_j(\mathbf{u}) = \mathscr{F}\big\{\psi_{e,N}(\mathbf{r})\big\} \tag{6.7}$$

$$= A_j(\mathbf{u})e^{\phi_j(\mathbf{u})} \tag{6.8}$$

$$\Psi'_j(\mathbf{u}) = \sqrt{I_j(\mathbf{u})}e^{i\phi_j(\mathbf{u})} \tag{6.9}$$

$$\psi'_{e,N}(\mathbf{r}) = \mathscr{F}^{-1}\big\{\Psi'(\mathbf{u})\big\}. \tag{6.10}$$

Next, the wave must be back-propagated and updated. To update the wave and object at the planes, the quantity $\Delta\psi_k$ is needed. It is defined as,

$$\Delta\psi_k = \psi'_{e,k}(\mathbf{r}) - \psi_{e,k}(\mathbf{r}). \tag{6.11}$$

The plane closest to the detector, plane N, is now updated as such,

$$O'_N(\mathbf{r}) = O_N(\mathbf{r}) + \alpha \frac{\psi^*_{i,N}(\mathbf{r})}{|\psi_{i,N}(\mathbf{r})|^2_{max}} \Delta\psi_N(\mathbf{r}) \tag{6.12}$$

$$\psi'_{i,N}(\mathbf{r}) = \psi_N(\mathbf{r}) + \alpha \frac{O^*_N(\mathbf{r})}{|O_N(\mathbf{r})|^2_{max}} \Delta\psi_N(\mathbf{r}) \tag{6.13}$$

where α is a weighting factor, typically set to 1. Next, the updated input surface wave at the final plane is back-propagated to get to plane $N-1$,

$$\psi'_{e,N-1} = \mathscr{P}_{-\Delta z_{N-1}}\{\psi'_{i,N}(\mathbf{r})\}. \tag{6.14}$$

To update the next interior input surface waves and object slices, Eqns. 6.12 and 6.13 are used at the $N-1$ slice,

$$O'_{N-1}(\mathbf{r}) = O_{N-1}(\mathbf{r}) + \alpha \frac{\psi^*_{i,N-1}(\mathbf{r})}{|\psi_{i,N-1}(\mathbf{r})|^2_{max}} \Delta\psi_{N-1}(\mathbf{r}) \tag{6.15}$$

$$\psi'_{i,N-1}(\mathbf{r}) = \psi_{i,N-1}(\mathbf{r}) + \alpha \frac{O^*_{N-1}(\mathbf{r})}{|O_{N-1}(\mathbf{r})|^2_{max}} \Delta\psi_{N-1}(\mathbf{r}) \tag{6.16}$$

this process is continued until the first slice is reached. Now the first slice of the object and probe are updated as follows,

$$O'_1(\mathbf{r}) = O_1(\mathbf{r}) + \alpha \frac{P^*(\mathbf{r}-\mathbf{R}_j)}{|P(\mathbf{r}-\mathbf{R}_j)|^2_{max}} \Delta\psi_1(\mathbf{r}) \tag{6.17}$$

$$P'(\mathbf{r}-\mathbf{R}_j) = P(\mathbf{r}-\mathbf{R}_j) + \alpha \frac{O^*_1(\mathbf{r})}{|O_1(\mathbf{r})|^2_{max}} \Delta\psi_1(\mathbf{r}). \tag{6.18}$$

Then, the guesses for the object and probe are set such that $O_k(\mathbf{r}) = O'_k(\mathbf{r})$ for each plane and $P(\mathbf{r}) = P'(\mathbf{r})$. At this point, the MEP constraint can be applied if desired.

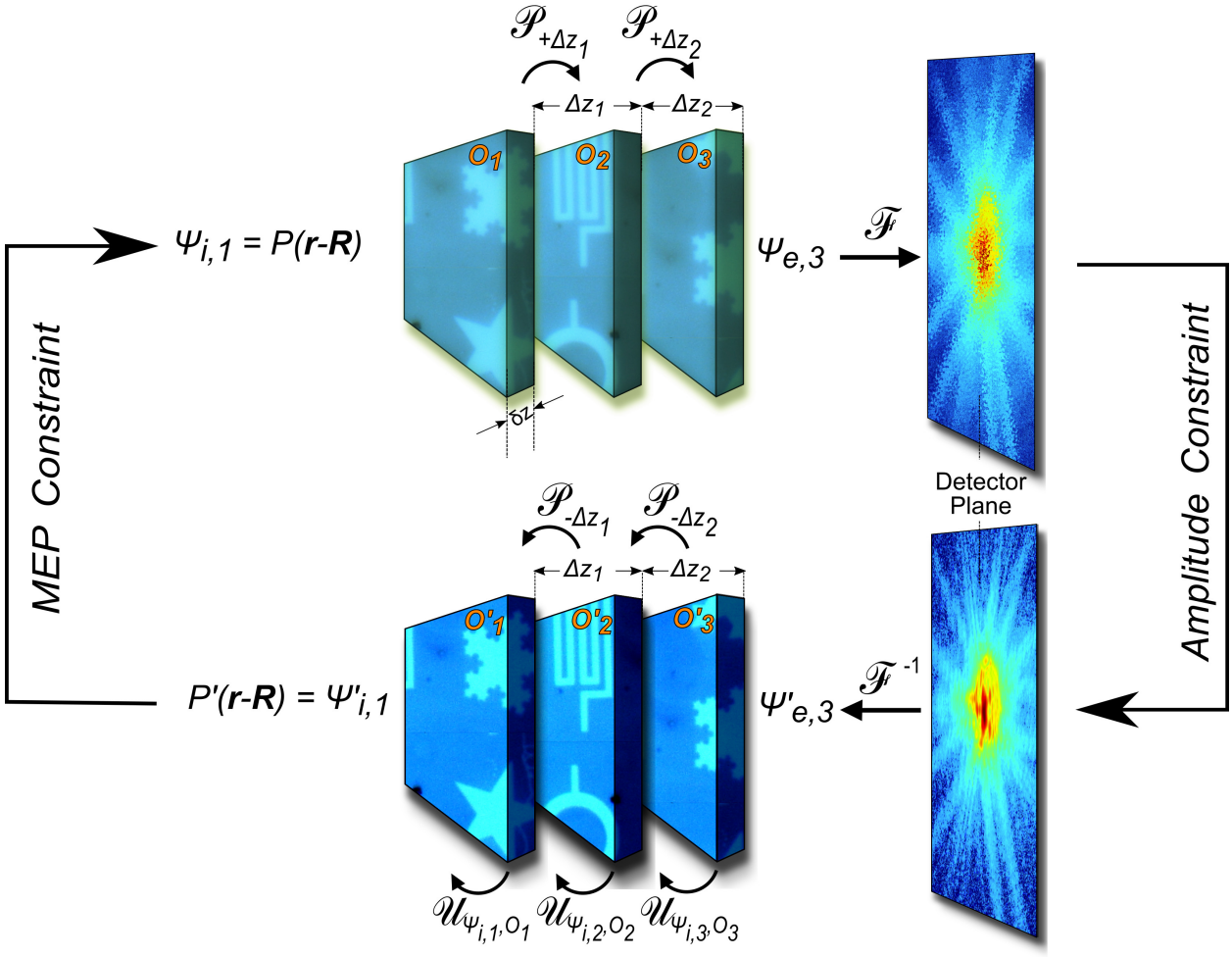

Figure 6.5: **Schematic of multislice ptychography**. Schematic of the multislice ptychography algorithm, showing the propagation $\mathscr{P}_{\Delta z_k}$ between slices and input surface wave and object updates $\mathscr{U}_{\psi_k,O_k}$ and constraints. The algorithm does not take into account the infinitesimal slice width δz, and therefore it should be small enough to be within the projection approximation.

Multislice ptychography has been successfully demonstrated in the visible range with biological samples [177,178]. It has also been applied the hard X-ray range with a synchrotron [209], but this approach was limited to two thin, independent samples separated by a large gap. Shimomura et al. [210] demonstrated a combination of multislice ptychography and precession ptychography. Precession is a technique often used in Bragg CDI and crystallography where a tilt series of diffraction patterns is collected. For certain objects and experimental conditions, the rotations can be approximated as shifts between the slices. The combination of tilt angles and multislice ptychog-

raphy allows more diversity in the set of scans due to the tilt angle, which shifts and rotates the collected solid angle of the Ewald sphere [210].

More recently, Tsai et al. [182] demonstrated extensions to multislice ptychography that can solve for an unknown object thickness, and showed that smaller step sizes increase the depth of field. They show that using a maximum-likelihood approach results in better image fidelity than the traditional approach for certain slice thicknesses.

A particular advantage of multislice ptychography is that it does not need probe-object factorization to be satisfied over the entire sample, and it readily accounts for multiple scattering events. By propagating the wave in between slices (which is a mixture of probe and object information), and multiplying by the next slice, the wave is free to change as it propagates and encounters other scatterers. Only each individual slice of the object needs to satisfy the probe-object factorization.

There are limits to this technique as well. Any section of the sample that is completely absorbing will block the wave directly in front of it, and lead to a loss of information. This is a potential problem for projection-based techniques as well, but can be mitigated by taking data at multiple angles or selecting an appropriate wavelength that is less absorbing.

6.2.4.1 Simulation of multislice ptychography

To illustrate the importance of multislice ptychography for thick samples, a simulation is shown consisting of three distinct slices. Fig. 6.6 shows a simulated object with three distinct slices (panels (a)-(c)), forming a semi-transparent sandwich that the incident probe propagates through. Panels (d)-(f), which are reconstructed using the multislice ptychography algorithm, both show high fidelity and good separation of the slices. Panel (g) shows the reconstruction with the traditional ptychography algorithm. Not only are the three slices superimposed on each other, the fidelity is degraded and they appear out of focus. Clearly, for objects of a certain thickness, multislice ptychography is crucial not only for separating different planes along the optical axis, but also for retrieving a high-fidelity image.

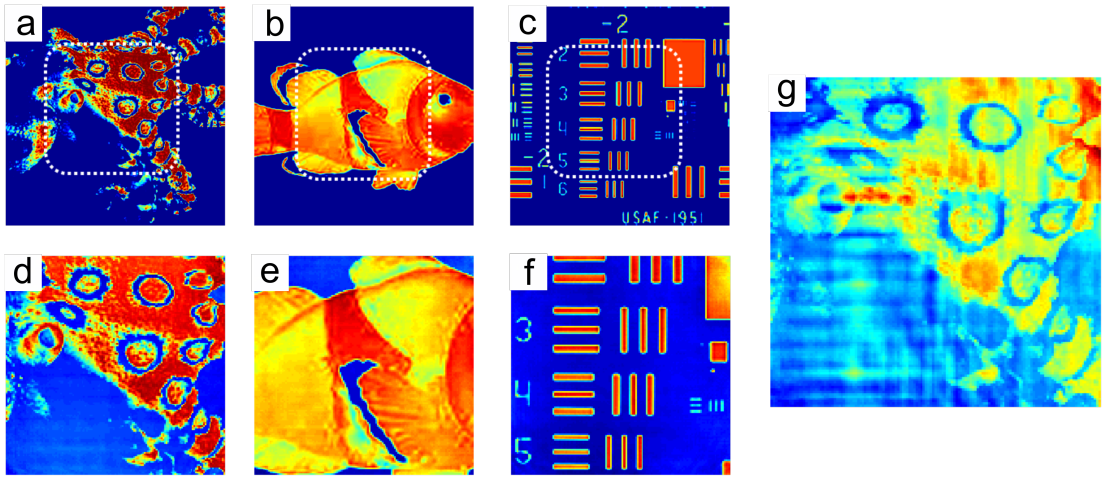

Figure 6.6: **Simulation of multislice ptychography versus traditional ptychography**. (a)-(c) Show the three slices of the simulated object's amplitude, with the white dashes indicating the field-of-view of the simulated scan. (d)-(f) Show the reconstruction of each of the slices using the multislice ptychography algorithm, while (g) shows the reconstruction of the *same data set* done with traditional 2D ptychography.

6.3 Three-dimensional multislice ptychography using a tabletop coherent EUV source

Finally, this section discusses recent work that has been done using multislice ptychography with the EUV tabletop microscope discussed in this thesis. As of the time of writing, this work is being prepared for publication [211].

6.3.1 Imaging functional materials with tabletop EUV

In order to demonstrate multislice imaging with a tabletop EUV source, this section shows imaging of functional material samples provided by Professor John Badding and colleagues at Pennsylvania State University.

6.3.1.1 3D imaging of silica opals

The first sample imaged are 120 nm opals, which consist of 120 nm-diameter silica spheres arranged in a self-assembled meta-lattice. The transverse structure is readily observed as hexagonal

close packed, but the samples often contain multiple layers, and the packing in between layers is not easy to observe directly. Furthermore, the inter-layer packing affects the functional properties of the material.

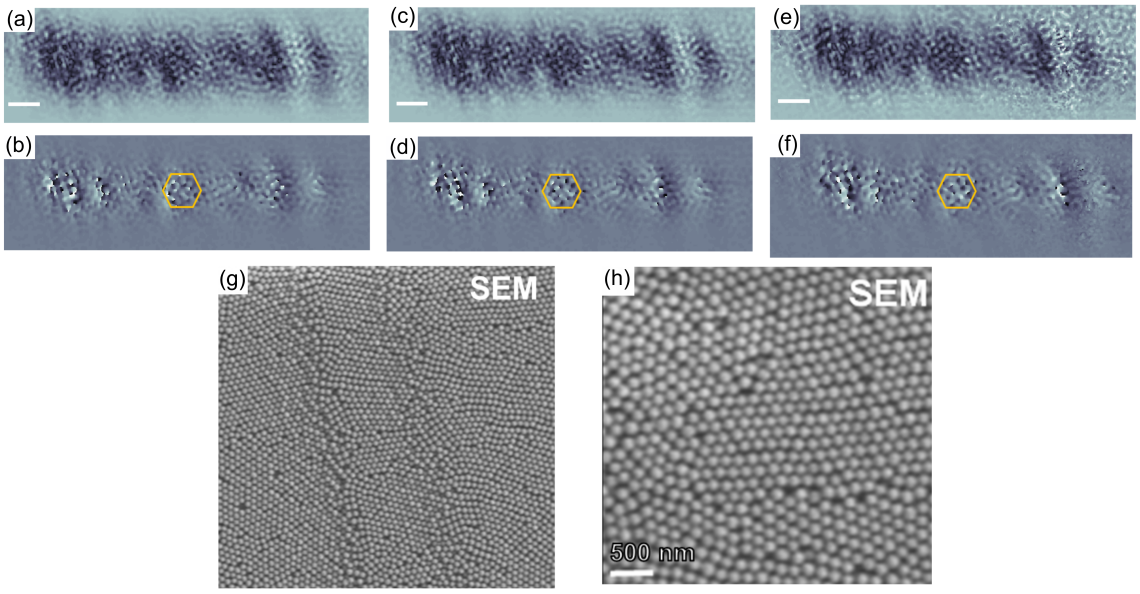

Figure 6.7: **Multislice reconstruction of multi-layered self-assembled opals**. Each slice is 120 nm thick. The top row containing (a),(c),(e) shows the reconstructed amplitude at the first, second, and third slice, while the row containing (b),(d),(f) shows the reconstructed phase. The scale bars on the top row are shared by (a)-(f) and are 500 nm. The yellow hexagons highlight the same area on different slices, and with additional analysis can be used to discern axial packing information. Panels (g) and (h) are representative SEM images that show regions of monolayers and multilayers, but only reveal packing information in the transverse direction.

6.3.1.2 3D imaging of silicon-infiltrated emerald ash borer

The second sample imaged was a silicon-infiltrated emerald ash borer (EAB). The wings of the EAB contain naturally occurring photonic bandgaps, and are of interest for materials engineering. Other body parts of the EAB are of interest as well for studying the silicon infiltration process as well as insect taxonomy. The Si-EAB sample was microtomed to be approximately 1 μm thick.

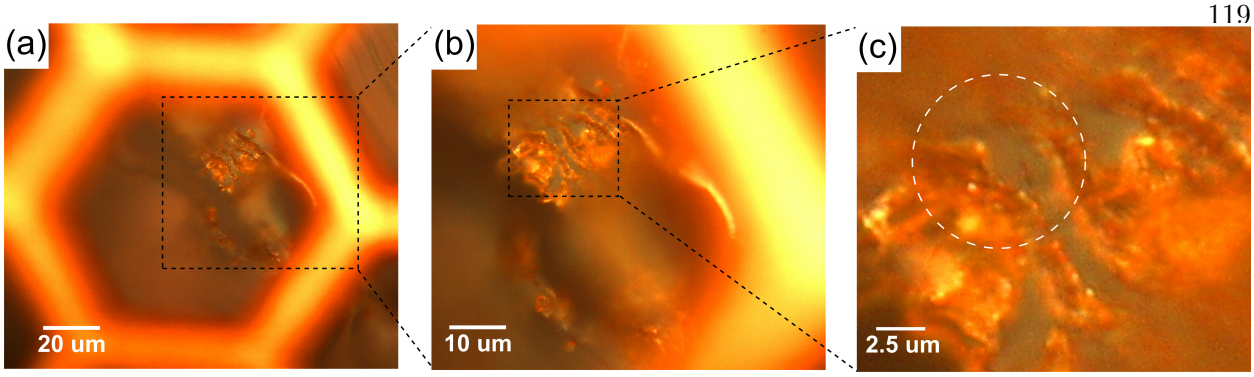

Figure 6.8: **Optical microscope image of Si-infiltrated emerald ash borer**. (a) Large field of view image of the sample. Black dashed box shows the region of interest obtained with a higher NA objective shown in (b). (c) Shows a zoomed-in region of (b), indicated by its black dashed box. The white dashed circle shows the field of view of the ptychography scan. The blurry hexagon, particularly visible in (a), is the TEM-grid on which the sample was mounted.

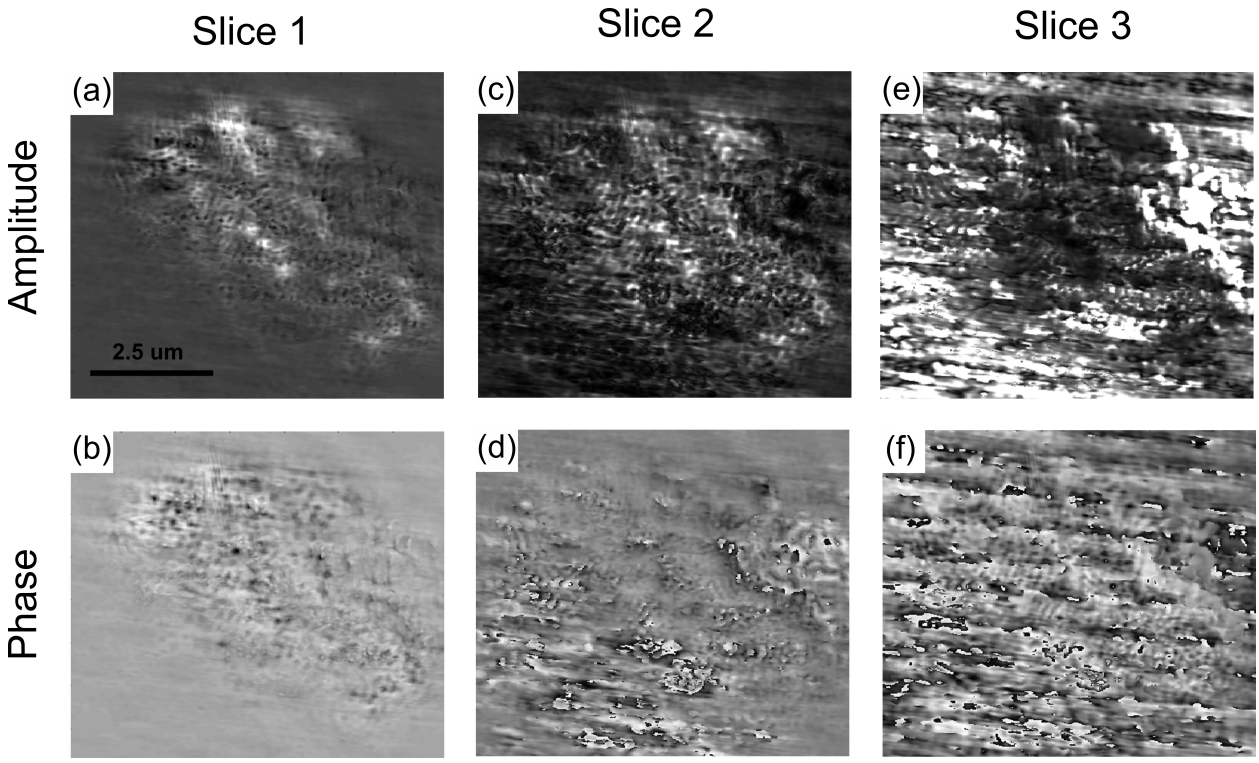

Figure 6.9: **Results of EUV multislice ptychography**. The top row shows the reconstructed amplitude, while the bottom row shows the reconstructed phase. The 2.5 μm scale bar in (a) is shared among all panels. (a) and (b) are the first slice, (c) and (d) are the middle slice, and (e) and (f) are the third slice. Each slice is 333 nm thick.

These results show both large and small-scale structures of the sample that can be seen in the optical microscope image. For instance, the overall shape of the structure, and the small round

structures that appear. The lines appearing on the third slice are consistent with striations visible on parts of the sample, perhaps due to the silicon infiltration process, or a broken piece of EAB wing. These striations are also visible (though slightly out of focus) in the upper right-hand corner of Fig. 6.8(a). Although the reconstructions are qualitatively consistent with the optical microscope image, further algorithmic testing (such as reconstructions with a greater number of slices), along with higher-fidelity images with more established modalities such as TEM, are needed to fully verify the result.

A challenge of imaging samples like this is that they cannot be readily imaged with other tabletop modalities. They cannot be imaged in an SEM in 3D, nor can they be imaged well in 2D, as they are non-conducting. TEM can image through structures, but they must be very thin. For silicon, the limit for depth imaging in a TEM is about 100 nm. Since these samples are non-trivially thick, imaging them in an optical microscope with high NA results in a short depth-of-focus, so portions of the sample will be blurry. Furthermore, silicon and biological material is fairly absorbing to visible wavelengths, so only the surface can be imaged. These preliminary results are promising, but warrant further analysis and additional proof-of-principle imaging with a well-characterized, simple test sample.

All the images presented in this thesis prior to this chapter imaged with EUV was performed on nano-fabricated samples. The samples were at some point designed and patterned, and were all readily imaged in SEM and AFM. Therefore, they were very well-known and well-characterized– in addition to being valid within the projection approximation. Making the jump to truly three-dimensional samples that were formed under only partially controlled conditions at best is challenging both due to the thick 3D nature of the samples *and* the fact that their structure is highly unknown. However, as ptychography CDI EUV microscopy continues to mature and become more established, imaging highly unknown samples will become more commonplace and widely accepted.

6.4 Conclusions

This chapter discussed the many different EUV/X-ray coherent diffractive imaging techniques that work for thick, three-dimensional samples, as well as presented work in preparation for publication. There are many different techniques suited for different needs, samples, and constraints, but clearly many important imaging tasks require imaging of thick samples. Future work in this regime is discussed in the next chapter.

Chapter 7

Future Outlook

This thesis has described the development of new capabilities for a tabletop EUV microscope. By extending the established technique of ptychography CDI to include reflection mode, quantitative chemically-sensitive, and three-dimensional capabilities, the microscope is more general and widely applicable than ever before.

In addition, work is in progress that takes advantage of the ultrafast nature of the high harmonic pulses. HHG bursts are attosecond-scale, and are automatically synchronized with the near-IR femtosecond pulses that drive them [120]. Therefore, high harmonics are in a uniquely advantageous position to lead in pump-probe dynamic imaging of picosecond or faster dynamics. Near-IR light is an excellent pump for thermal and acoustic dynamics of certain materials [212–214], and the ability to conduct these studies with high-resolution, spatially-resolved, non-periodic samples will be of immense importance for understanding nanoscale heat and phonon dynamics.

EUV/X-ray microscopy stands to answer many questions and solve many scientific and technological challenges. Although much progress has been made laying the groundwork, applications of this technology are only beginning to unfold. This chapter will describe future directions for various projects, including some which are already well underway, to better characterize and understand nano-scale systems by combining different tools and approaches.

7.1 Future directions in tabletop EUV/soft X-ray three-dimensional imaging

Although tabletop EUV three-dimensional is relatively new, many systems can be sensitively imaged with these emerging capabilities. This section explores a few exciting applications for different three-dimensional techniques.

7.1.1 Ptychographic multislice imaging

Many opportunities exist to use multislice ptychography [177, 178] to image thick biological specimens, particularly with shorter wavelengths in the water window [116]. Its potential lies not only in three-dimensional imaging from a single angle, but also in improving two-dimensional imaging and enabling three-dimensional ptychographic-tomography.

A two dimensional object that is not perfectly planar is only two-dimensional insofar as it satisfies the projection approximation. However, even for thin, simple samples, this approximation is not necessarily valid. For instance, even in a macroscopically-thin pinhole type object, if the input wave diffracts through the object it no longer satisfies this approximation. This is usually not a problem, as CDI reconstructs the exit surface wave (which from a convergence perspective need not be identical to the input surface wave times the object's transmission function) but ultimately restricts CDI to unrealistically thin objects. Reflection imaging can often get around this issue, as it is very reasonable to nanostructures that are $\approx$1 wavelength tall, but it is more difficult to fabricate a transmissive object of the same thickness. Therefore, for imaging multilayered reflective samples or thick real-world transmissive samples, it is crucial to utilize image reconstruction techniques that account for diffraction *within* the sample. Multislice ptychography is perfectly suited for this task, particularly for non-pinhole like samples, where the area around the sample is more transmissive than the sample itself– for instance, an absorbing structure, like a cell, mounted on a silicon nitride membrane.

Furthermore, multislice ptychography can potentially be combined with other ptychographic techniques, such as information multiplexed ptychography, and can be used to aid in tomographic

techniques. Tomographic techniques rely on obtaining a reliable projection of a three-dimensional object, but if the light diffracts over the length of the object then the projection will be distorted. Some diffraction tomography techniques have taken this into account [215], and will likely be important for obtaining accurate projections needed for EUV ptycho-tomography. By computationally reconstructing the object for a given projection *at each plane that individually satisfies the projection approximation*, more accurate projections can be obtained, which will lead to higher fidelity tomographic reconstructions [182].

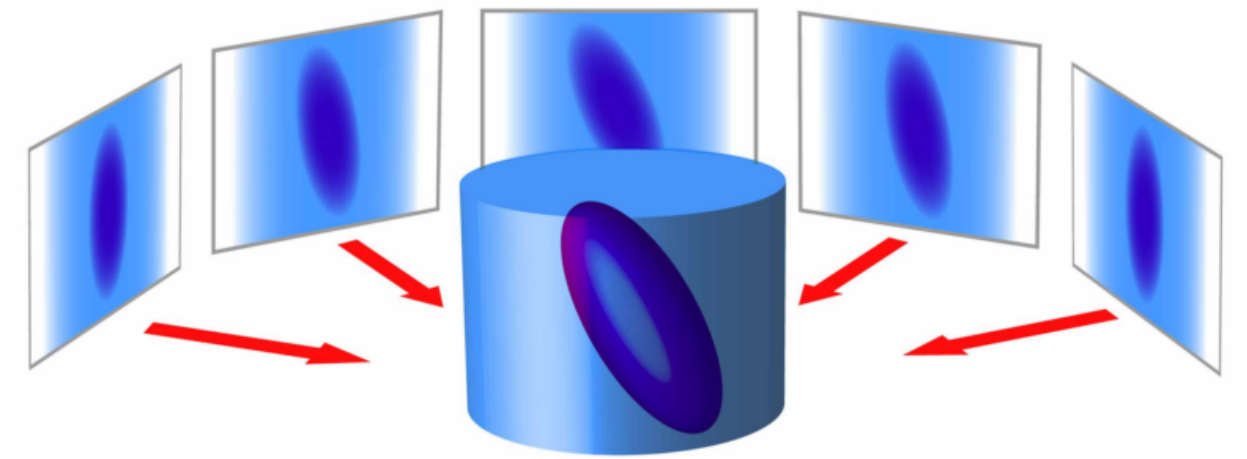

Figure 7.1: **Diagram illustrating the principle of tomography**. Projections of the sample are obtained at various angles, and used together to form a reconstructed three-dimensional image. It is important that the projections used in tomography be accurate. Figure adapted from Ref. [198].

7.1.2 Ptychographic tomography

As harmonic flux and stability improves, an interesting future direction will be to incorporate a rotation stage and pursue ptychographic tomography. This method will allow even more robust three-dimensional reconstructions, but requires more flux. A schematic of a future ptychographic tomography (or ioCDI tomography) setup is shown in Fig. 7.2.

Although it may not be feasible to obtain hundreds of angles of ptychographic images, recent work in equally sloped tomography (EST) has shown promise in providing high-resolution, low-artifact images with fewer slices than traditional back-projection based tomography [74, 196, 216–

218].

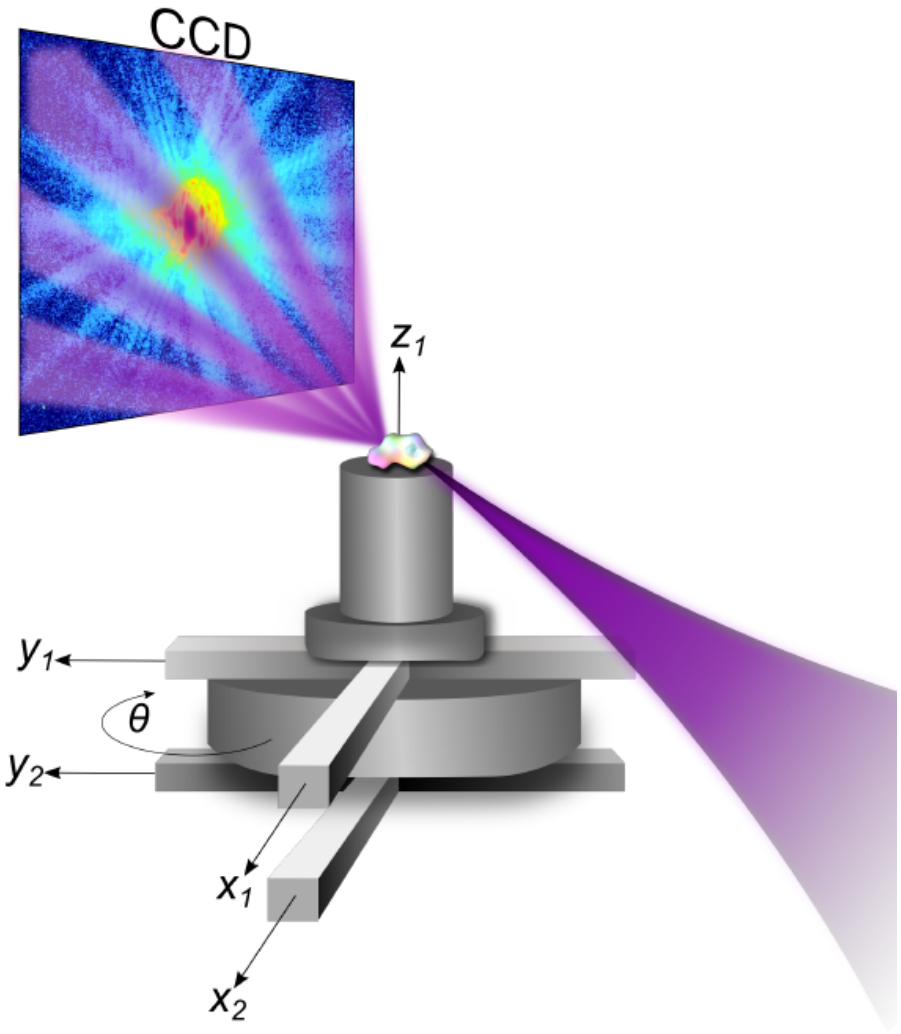

Figure 7.2: **EUV ptychographic tomography setup**. Concept for ptychographic tomography, where stages x_1, y_1, z_1 are used to position the sample with respect to the focus and do the ptychography scan. Rotation stage θ changes the sample angle and is aligned with respect to the center of the sample using stages x_2, y_2.

Another area of interest is using three-dimensional techniques to do tomography in reflection mode. By using multislice propagation together with tomographic techniques, complicated three-dimensional thick samples, such as integrated circuits [206] can be imaged with high sensitivity and high throughput, and will be relieved from single-angle phase imaging issues such as the 2π phase ambiguity.

7.2 Quantitative imaging

Quantitative imaging of physical nanoscale properties stands to bring fourth a new and powerful metrology for studying nanosystems with extraordinary chemical sensitivity. Though the work shown in Chapter 5 was dependent on a-priori knowledge and sample measurements using other modalities, this prior knowledge may not always be necessary if further constraints are placed on the system.

Reflectivity in the EUV is incredibly sensitive not only to wavelength, but also to angle. Incorporating a well-known comb of harmonics or a rotation stage at various angles, and doing multiplexed ptychography or taking ptychographic scans at multiple angles will constrain the system so that the chemical composition, interlayer diffusion, and surface roughness can all be very sensitively modeled, based on the change in complex reflectivity.

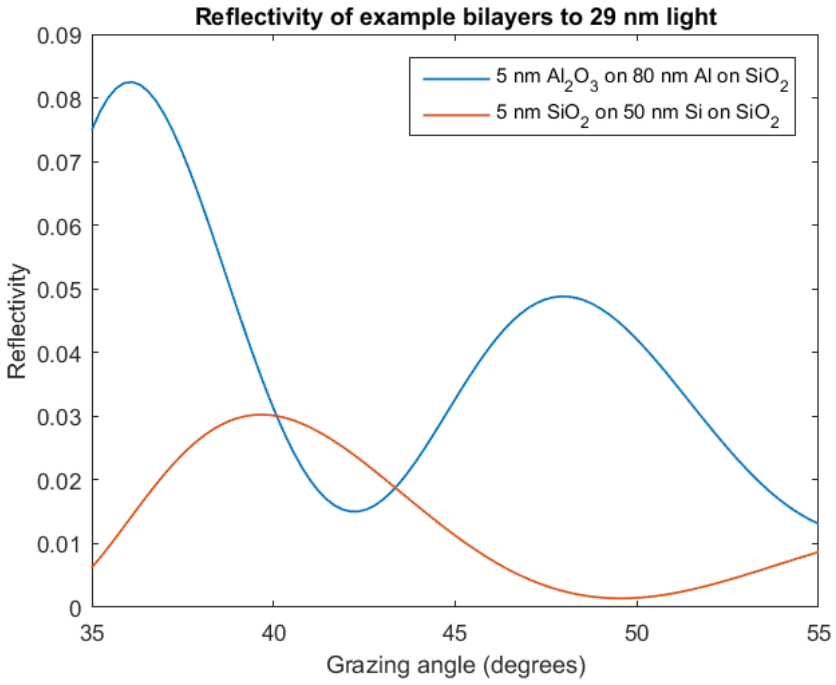

Figure 7.3: **Reflectivity of example bilayers to 29 nm light**. Multilayer stacks are particularly sensitive to reflectivity changes in the EUV over a relatively small range of angles [42].

Although the EUV light will need to be reflective to the substrate and penetrative to the

overlayer, the wide range of absorption edges within the EUV range reachable using high harmonic generation will make it possible to perform quantitative imaging of unknown multilayered nanostructures using a variety of wavelengths and/or angles.

7.2.1 Dynamic imaging

Thermal and acoustic properties of thin films and other materials have been studied extensively and have led to new and interesting insights into heat flow and phonon behavior at the nanoscale [212–214, 219]. However, many of these studies rely on periodic structures' collective diffraction signal and do not fare especially well with aperiodic structures, nor are they spatially resolved.

Much work has been done already on tabletop dynamic imaging, [179, 220] where time-resolved stroboscopic images are taken in a pump-probe geometry using ptychography CDI [81, 163]. Dynamic imaging promises to provide spatially-resolved, high resolution studies of thermal expansion, heat flow, and acoustic wave travel.

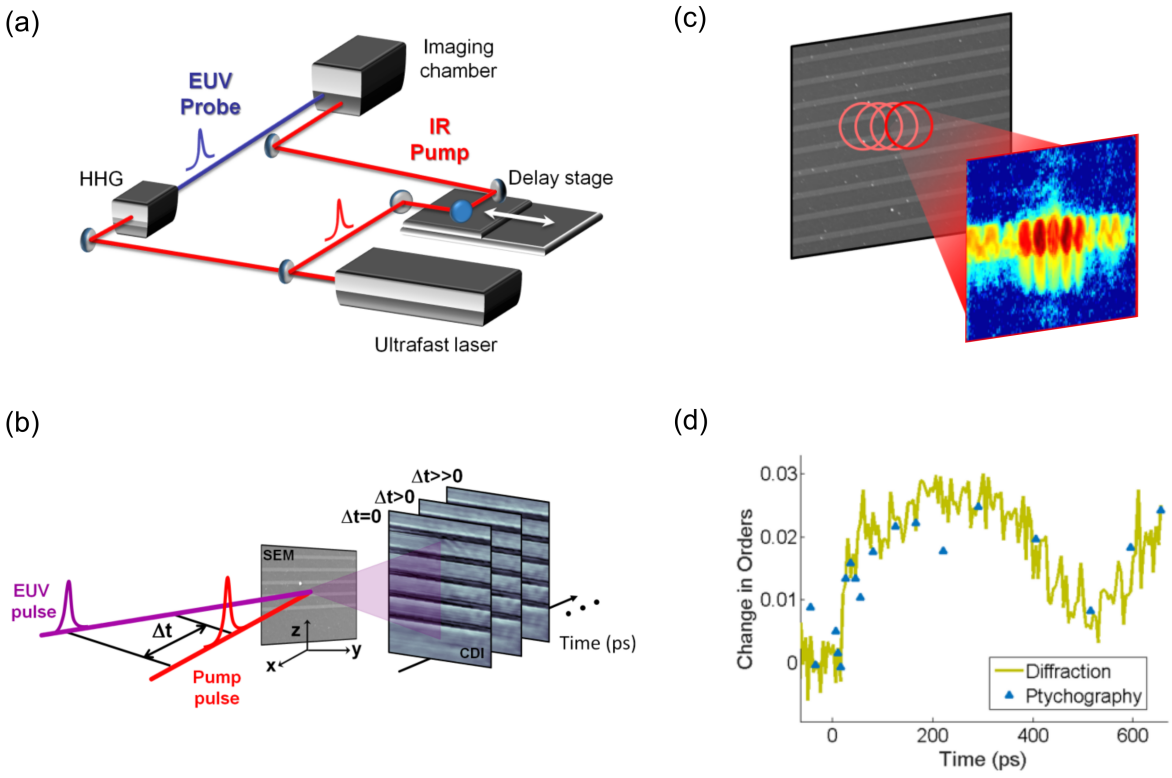

Figure 7.4: **Dynamic pump-probe EUV imaging**. (a) Schematic of pump-probe setup with EUV probe and IR pump. (b) The EUV light is reflected from and the IR pump light is absorbed into the sample. Some IR light is reflected as well, but is blocked by an aluminum filter in front of the camera. Ptychographic images are obtained at every time delay. (c) Ptychography scans are obtained on a sample of nickel lines. (d) The acoustic signal obtained from diffraction alone (yellow line) and from ptychographic reconstruction (blue triangles). Figure adapted from Ref. [220].

Dynamic imaging has been demonstrated not only on repeating lines as in Fig. 7.4(b), but also on an individual 16 μm pillar, shown in Fig. 7.5.

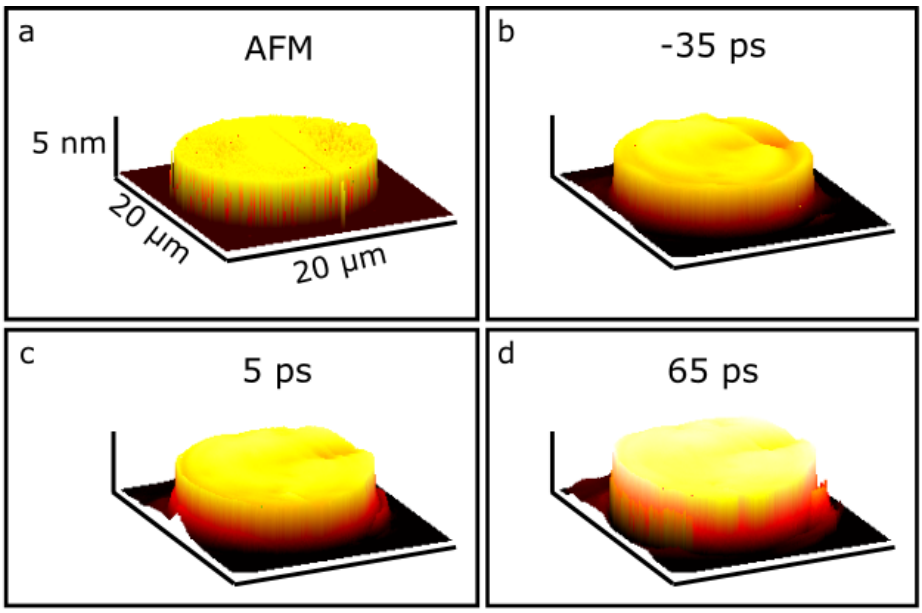

Figure 7.5: **Imaging thermal expansion in a pillar**. (a) AFM image of the nickel pillar and (b)-(d) ptychographic imaging of the pillar shown at different time delays. The pillar can be seen to be expanding and deforming as it is heated. Figure adapted from Ref [220].

In addition to imaging thermal and acoustic modes, this technique can potentially be used to image phase transitions in meta-materials, surface plasmons, and spin dynamics.

7.3 Magnetic imaging

High harmonics are an excellent tool for studying ultrafast magnetic behavior. Ultrafast laser-induced magnetization, spin currents, and demagnetization have all been studied [221, 222], and with new technology allowing the production of circularly polarized harmonics to study X-ray magnetic circular dichrosim (XMCD) [125, 223], spatially-resolved studies using dynamic imaging can potentially reveal new and exciting physics.

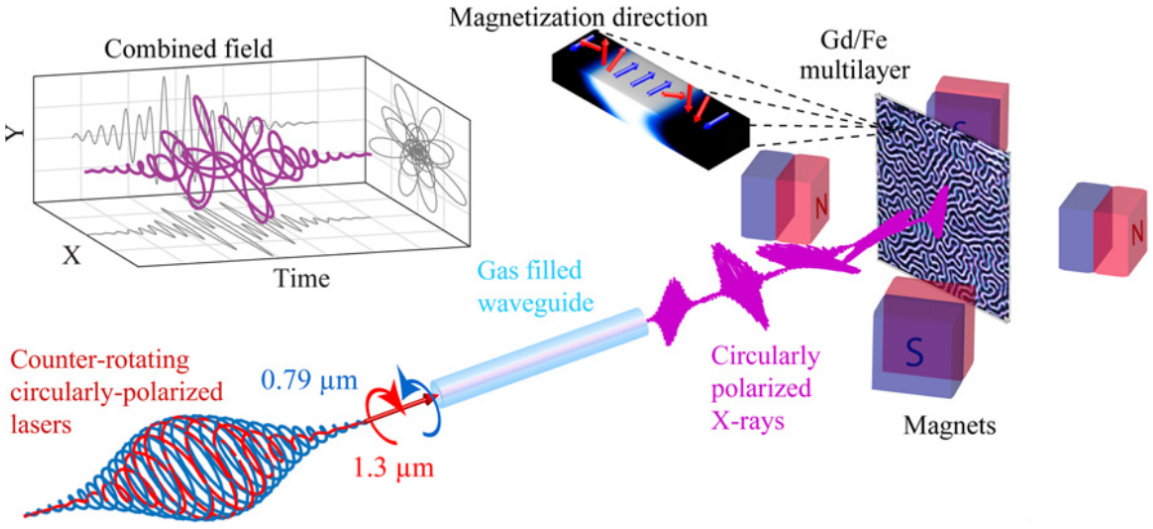

Figure 7.6: **Circularly polarized harmonics to study X-ray magnetic circular dichroism**. Experimental schematic of circularly polarized harmonics being used to investigate a Gd/Fe multilayer in a magnetic field. Figure adapted from Ref. [223].

7.4 Hybrid and real-time imaging

Finally, two exciting but technically challenging possibilities lie in hybrid and real-time imaging. While various ptychography CDI images shown throughout this thesis have been able to demonstrate exquisite transverse and axial resolution, there is still a need for other modalities such as SEM, which has unparalleled spatial resolution for a tabletop device, and AFM, which is capable of making incredibly sensitive height and material measurements. Visible microscopy is also important for quick, wide field-of-view imaging.

For nanometrology and industrial applications, an ideal microscope would combine multiple modalities. For instance, visible microscopes could be used for locating interesting portions of the sample to take high resolution images with using high harmonics or electrons. Ultrafast electron microscopy and electron diffraction have revealed material properties [224] and imaged 3D structures down to the atomic level [225, 226].

Real-time imaging promises to usher tabletop EUV ptychography CDI towards becoming commonplace in modern microscopy. Currently, camera readout rates and reconstruction time

give at minimum, about an hour between locating the part of the sample to image and having a reasonable reconstruction. For a full-chip scan and readout rate of 1 MHz, a ptychography scan that requires $<$ 1 minute of exposure time will take over 30 minutes to collect all the data due to the readout time of the camera. Time is also spent transferring the raw data from the experiment-control computer to the reconstruction computer, and then the data must be processed and reconstructed.

Fortunately, there are paths forward to cut down this time significantly. New camera and CMOS technology can read data out at a much faster rate. Direct Ethernet connections and automated processing software, done in parallel on multiple GPUs, can speed up the transfer and reconstruction processes. Much as ever-increasing computing power has enabled the field of computational imaging to grow rapidly, so will further increase allow it to lead to real-time video-rate CDI microscopy.

7.5 Conclusions

Over the past 10 years, EUV tabletop coherent diffractive imaging microscopy has matured from low-NA imaging of isolated test samples [47] to a full-field, high-NA microscope capable of imaging dynamic, three-dimensional, and real-world industry-relevant samples. As work continues to extend the microscopy capability using ptychography CDI and variations thereof, this microscopy technique proves itself to be versatile and widely applicable to a range of samples. The continued algorithm and instrument development, higher-flux and shorter-wavelength harmonic sources, and the synthesis of different imaging and ultrafast metrology techniques are rapidly advancing this technology to becoming an everyday tool for nanoscale science and nanotechnology.

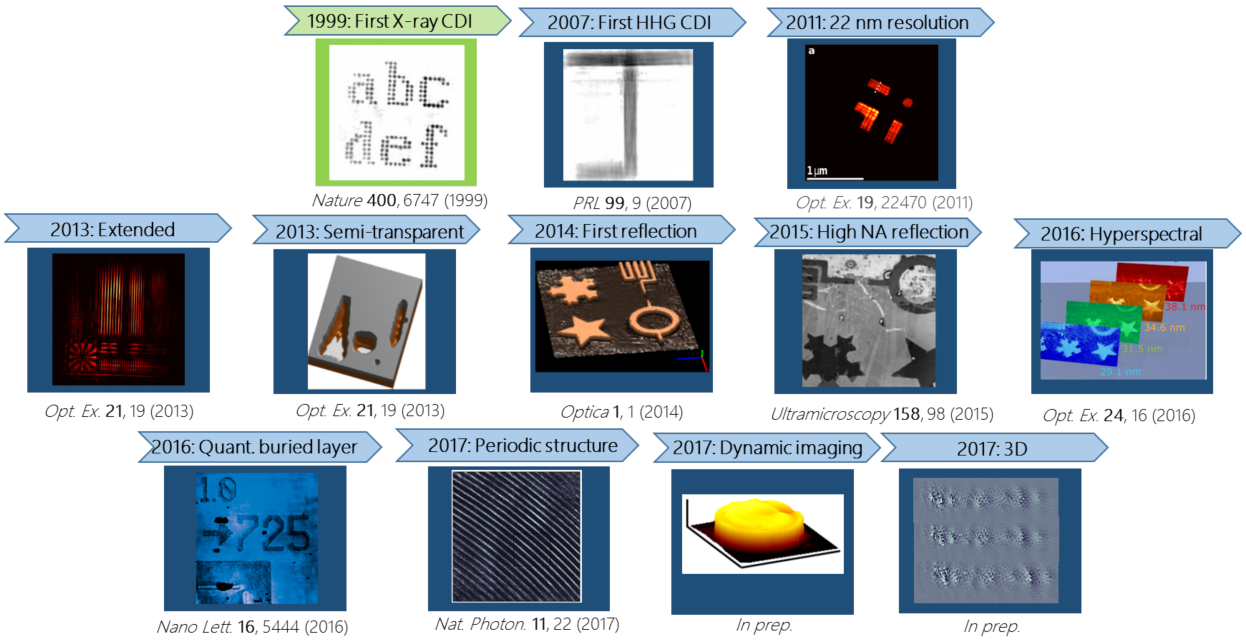

Figure 7.7: **Progress in HHG EUV CDI**. Timeline highlighting progress made in EUV/X-ray CDI, beginning with the first demonstration of CDI in the X-ray range (green) along with work done in the last 10 years on the tabletop EUV HHG CDI microscope (blue). Figures adapted from Refs. [39, 40, 47, 52, 53, 59, 77, 86, 145, 211, 220].

Bibliography

[1] C. K. Rosenthal, N. Gray, and N. Blow, "Milestones in Light Microscopy," Nature Cell Biology, vol. 11, pp. S6—-S9, 2009.

[2] R. Hooke, Micrographia: or Some Physiological Descriptions of Minute Bodies, Made by Magnifying Glasses with Observations and Inquiries Thereupon. Martyn, John, 1st ed., 1665.

[3] D. Sayre, "Some implications of a theorem due to Shannon," Acta Crystallographica, vol. 5, no. 6, p. 843, 1952.

[4] J. Cowley, "The future of high-resolution electron microscopy," Ultramicroscopy, vol. 18, no. 4, pp. 463–467, 1985.

[5] J. E. Hobbie, R. J. Daley, and S. Jasper, "Use of nuclepore filter counting bacteria by fluoroscence microscopy," Applied and Environmental Microbiologynvironmental microbiology, vol. 33, pp. 1225–1228, 1977.

[6] E. Abbe, "Beiträge zur Theorie des Mikroskops und der mikroskopischen Wahrnehmung," Archiv für Mikroskopische Anatomie, vol. 9, pp. 413–418, 1873.

[7] F. Zernike, "Phase contrast, a new method for the microscopic observation of transparent objects," Physica, vol. 9, no. 10, pp. 974–986, 1942.

[8] M. Born and E. Wolf, Principles of Optics. Cambridge University Press, 7th ed., 1999.

[9] Q. Wu, G. D. Feke, R. D. Grober, and L. P. Ghislain, "Realization of numerical aperture 2.0 using a gallium phosphide solid immersion lens," Applied Physics Letters, vol. 75, no. 26, pp. 4064–4066, 1999.

[10] K. Vernon-Parry, "Scanning electron microscopy: an introduction," III-Vs Review, vol. 13, no. 4, pp. 40–44, 2000.

[11] G. Binnig, C. F. Quate, and C. Gerber, "Atomic Force Microscope," Physical Review Letters, vol. 56, no. 9, pp. 930–934, 1986.

[12] N. Jalili and K. Laxminarayana, "A review of atomic force microscopy imaging systems: Application to molecular metrology and biological sciences," Mechatronics, vol. 14, no. 8, pp. 907–945, 2004.

[13] E. Hecht, Optics. Pearson education, Addison-Wesley, 2002.

[14] J. C. H. Spence, U. Weierstall, and M. Howells, "Coherence and sampling requirements for diffractive imaging," Ultramicroscopy, vol. 101, no. 2-4, pp. 149–152, 2004.

[15] M. G. Nomarski, "Microinterféromètre différentiel à ondes polarisées," Journal de Physique et le Radium, vol. 16, pp. S9–S13, 1955.

[16] R. D. Allen, G. B. David, and M. G. Nomarski, "The Zeiss-Nomarski differential interference equipment for transmitted-light microscopy," Zeitschrift fur wissenschaftliche Mikroskopie und mikroskopische Technik, vol. 69, pp. 193–221, 1963.

[17] M. K. Kim, "Principles and techniques of digital holographic microscopy," SPIE Reviews, vol. 1, no. 018005, 2010.

[18] C. Wang, H. Shpaisman, A. D. Hollingsworth, and D. G. Grier, "Celebrating Soft Matter's 10th Anniversary: Monitoring colloidal growth with holographic microscopy," Soft Matter, vol. 11, no. 6, pp. 1062–1066, 2015.

[19] Z. Liu, L. Tian, S. Liu, and L. Waller, "Real-time brightfield, darkfield, and phase contrast imaging in a light-emitting diode array microscope," Journal of Biomedical Optics, vol. 19, no. 10, p. 106002, 2014.

[20] E. Betzig, A. Lewis, A. Harootunian, M. Isaacson, and E. Kratschmer, "Near Field Scanning Optical Microscopy (NSOM)," Biophysical Journal, vol. 49, no. 1, pp. 269–279, 1986.

[21] Y. Inouye and S. Kawata, "Near-field scanning optical microscope with a metallic probe tip," Optics Letters, vol. 19, no. 3, pp. 159–161, 1994.

[22] R. C. Dunn, "Near-Field Scanning Optical Microscopy," Chemical Review, vol. 99, no. 2891-2927, 1999.

[23] B. Pollard, E. A. Muller, K. Hinrichs, and M. B. Raschke, "Vibrational nano-spectroscopic imaging correlating structure with intermolecular coupling and dynamics," Nature Communications, vol. 5, pp. 1–7, 2014.

[24] M. J. Rust, M. Bates, and X. Zhuang, "Stochastic optical reconstruction microscopy (STORM) provides sub-diffraction-limit image resolution," Nature Methods, vol. 3, no. 10, pp. 793–795, 2006.

[25] M. Gunkel, F. Erdel, K. Rippe, P. Lemmer, R. Kaufmann, C. Hörmann, R. Amberger, and C. Cremer, "Dual color localization microscopy of cellular nanostructures," Biotechnology Journal, vol. 4, no. 6, pp. 927–938, 2009.

[26] T. A. Klar, S. Jakobs, M. Dyba, A. Egner, and S. W. Hell, "Fluorescence microscopy with diffraction resolution barrier broken by stimulated emission," Proceedings of the National Academy of Sciences, vol. 97, no. 15, pp. 8206–8210, 2000.

[27] T. A. Klar, E. Engel, and S. W. Hell, "Breaking Abbe's diffraction resolution limit in fluorescence microscopy with stimulated emission depletion beams of various shapes," Physical Review E, vol. 64, pp. 1–9, 2001.

[28] E. Betzig, G. H. Patterson, R. Sougrat, O. W. Lindwasser, S. Olenych, J. S. Bonifacino, M. W. Davidson, J. Lippincott-schwartz, and H. F. Hess, "Imaging Intracellular Fluorescent Proteins at Nanometer Resolution," Science, vol. 313, pp. 1642–1646, 2006.

[29] J. Goldstein, D. Newbury, D. Joy, C. Lyman, P. Echlin, E. Lifshin, L. Sawyer, and J. Michael, Scanning Electron Microscopy and X-Ray Microanalysis. New York: Springer, 3rd ed., 2003.

[30] G. H. Bernstein, A. D. Carter, and D. C. Joy, "Do SEII electrons really degrade SEM image quality?," Scanning, vol. 35, no. 1, pp. 1–6, 2013.

[31] M. Nagase, H. Narnatsu, K. Murase, T. Makino, and M. Wakamiya, "Nano-scale fluctuations in electron beam resist pattern evaluated by atomic force microscopy," Microelectronic engineering, vol. 30, pp. 419–422, 1996.

[32] R. M. A. Sullen, A. B. Churnside, D. M. Nguyen, M. S. Bull, and T. T. Perkins, "Atomic force microscopy with sub-picoNewton force stability for biological applications," Methods, vol. 60, no. 2, pp. 131–141, 2013.

[33] C. Lee, X. Wei, J. W. Kysar, and J. Hone, "Measurement of the elastic properties and intrinsic strength of monolayer graphene," Science, vol. 321, pp. 385–388, 2008.

[34] M. Marrese, V. Guarino, and L. Ambrosio, "Atomic Force Microscopy: A Powerful Tool to Address Scaffold Design in Tissue Engineering," Journal of Functional Biomaterials, vol. 8, no. 1, p. 7, 2017.

[35] J. D. Jackson, Classical Electrodynamics. Hoboken, NJ: John Wiley & Sons, 3rd ed., 1999.

[36] J. Cowley, Diffraction Physics. Amsterdam: Elsevier, 3rd ed., 1995.

[37] J. W. Goodman, Introduction to Fourier Optics. Greenwood Village: Roberts & Company Publishers, 3rd ed., 2005.

[38] D. F. Gardner, B. Zhang, M. D. Seaberg, L. S. Martin, D. E. Adams, F. Salmassi, E. Gullikson, H. Kapteyn, and M. Murnane, "High numerical aperture reflection mode coherent diffraction microscopy using off-axis apertured illumination.," Optics express, vol. 20, no. 17, pp. 19050–9, 2012.

[39] M. D. Seaberg, B. Zhang, D. F. Gardner, E. R. Shanblatt, M. M. Murnane, H. C. Kapteyn, and D. E. Adams, "Tabletop nanometer extreme ultraviolet imaging in an extended reflection mode using coherent Fresnel ptychography," Optica, vol. 1, no. 1, pp. 39–44, 2014.

[40] B. Zhang, D. F. Gardner, M. D. Seaberg, E. R. Shanblatt, H. C. Kapteyn, M. M. Murnane, and D. E. Adams, "High contrast 3D imaging of surfaces near the wavelength limit using tabletop EUV ptychography," Ultramicroscopy, vol. 158, pp. 98–104, 2015.

[41] D. T. Attwood, Soft X-Rays and Extreme Ultraviolet Radiation: Principles and Applications. Cambridge: Cambridge University Press, 2007.

[42] The Center for X-Ray Optics, "http://www.cxro.lbl.gov/."

[43] W. Chao, B. D. Harteneck, J. A. Liddle, E. H. Anderson, and D. T. Attwood, "Soft X-ray microscopy at a spatial resolution better than 15 nm.," Nature, vol. 435, no. 7046, pp. 1210–1213, 2005.

[44] A. V. Baez and P. Kirkpatrick, "Formation of Optical Images by X-Rays," Journal of the Optical Society of America, vol. 6, no. 1895, pp. 766–774, 1946.

[45] P. Thibault, M. Dierolf, A. Menzel, O. Bunk, C. David, and F. Pfeiffer, "High-resolution scanning x-ray diffration microscopy," Science, vol. 321, pp. 379–383, 2008.

[46] A. Sakdinawat and D. Attwood, "Nanoscale X-ray imaging," Nature Photonics, vol. 4, pp. 840–848, 2010.

[47] R. L. Sandberg, A. Paul, D. A. Raymondson, S. Hädrich, D. M. Gaudiosi, J. Holtsnider, R. I. Tobey, O. Cohen, M. M. Murnane, H. C. Kapteyn, C. Song, J. Miao, Y. Liu, and F. Salmassi, "Lensless diffractive imaging using tabletop coherent high-harmonic soft-X-ray beams," Physical Review Letters, vol. 99, no. 9, pp. 1–4, 2007.

[48] H. N. Chapman and K. a. Nugent, "Coherent lensless X-ray imaging," Nature Photonics, vol. 4, pp. 833–839, dec 2010.

[49] R. H. T. Bates, "Fourier phase problems are uniquely solvable in more than one dimension," Optik, vol. 61, no. 3, pp. 247–262, 1982.

[50] V. Elser, "Phase retrieval by iterated projections," Journal of the Optical Society of America A, vol. 20, no. 1, pp. 40–55, 2003.

[51] S. Marchesini, H. He, H. N. Chapman, S. P. Hau-Riege, a. Noy, M. R. Howells, U. Weierstall, and J. C. H. Spence, "X-ray image reconstruction from a diffraction pattern alone," Physical Review B, vol. 68, no. 14, p. 140101, 2003.

[52] M. D. Seaberg, D. E. Adams, E. L. Townsend, D. A. Raymondson, W. F. Schlotter, Y. Liu, C. S. Menoni, L. Rong, C.-C. Chen, J. Miao, H. C. Kapteyn, and M. M. Murnane, "Ultrahigh 22 nm resolution coherent diffractive imaging using a desktop 13 nm high harmonic source.," Optics express, vol. 19, no. 23, pp. 22470–22479, 2011.

[53] E. R. Shanblatt, C. L. Porter, D. F. Gardner, G. F. Mancini, R. M. Karl, M. D. Tanksalvala, C. S. Bevis, V. H. Vartanian, H. C. Kapteyn, D. E. Adams, and M. M. Murnane, "Quantitative Chemically-Specific Coherent Diffractive Imaging of Buried Interfaces using a Tabletop EUV Nanoscope," Nano Letters, vol. 16, no. 9, pp. 5444–5450, 2016.

[54] R. W. Gerchberg and W. O. Saxton, "A practical algorithm for the determination of phase from image and diffraction plane pictures," Optik, vol. 35, no. 2, pp. 237–246, 1972.

[55] C. E. Shannon, "Communication in the Presence of Noise," Proceedings of the Institute of Radio Engineers, vol. 37, pp. 10–21, 1949.

[56] J. R. Fienup, "Reconstruction of an object from the modulus of its Fourier transform," Optics letters, vol. 3, no. 1, pp. 27–29, 1978.

[57] J. Fienup, "Phase retrieval algorithms: a comparison," Applied Optics, vol. 21, no. 15, pp. 2758–2769, 1982.

[58] I. Robinson, J. Libbert, I. Vartanyants, J. Pitney, D. Smilgies, D. Abernathy, and G. Grübel, "Coherent x-ray diffraction imaging of silicon oxide growth," Physical Review B, vol. 60, no. 14, pp. 9965–9972, 1999.

[59] J. Miao, P. Charalambous, J. Kirz, and D. Sayre, "Extending the methodology of X-ray crystallography to allow imaging of micrometre-sized non-crystalline specimens," Nature, vol. 400, no. 6742, pp. 342–344, 1999.

[60] R. Karl, C. Bevis, R. Lopez-Rios, J. Reichanadter, D. Gardner, C. Porter, E. Shanblatt, M. Tanksalvala, G. F. Mancini, M. Murnane, H. Kapteyn, and D. Adams, "Spatial, spectral, and polarization multiplexed ptychography," Optics Express, vol. 23, no. 23, pp. 30250–30258, 2015.

[61] J. A. Rodriguez, R. Xu, C.-C. Chen, Z. Huang, H. Jiang, A. L. Chen, K. S. Raines, A. Pryor Jr, D. Nam, L. Wiegart, C. Song, A. Madsen, Y. Chushkin, F. Zontone, P. J. Bradley, and J. Miao, "Three-dimensional coherent X-ray diffractive imaging of whole frozen-hydrated cells," IUCrJ, vol. 2, no. 5, pp. 575–583, 2015.

[62] S. Marchesini, "Phase retrieval and saddle-point optimization.," Journal of the Optical Society of America A, vol. 24, no. 10, pp. 3289–96, 2007.

[63] G. Williams, H. Quiney, B. Dahl, C. Tran, a. Peele, K. Nugent, M. Dejonge, and D. Paterson, "Curved beam coherent diffractive imaging," Thin Solid Films, vol. 515, no. 14, pp. 5553–5556, 2007.

[64] L. W. Whitehead, G. J. Williams, H. M. Quiney, D. J. Vine, R. A. Dilanian, S. Flewett, and K. A. Nugent, "Diffractive Imaging Using Partially Coherent X Rays," Physical Review Letters, vol. 103, no. 243902, pp. 1–4, 2009.

[65] S. T. Thurman and J. R. Fienup, "Phase retrieval with signal bias," Journal of the Optical Society of America A, vol. 26, no. 4, pp. 1008–1014, 2009.

[66] D. E. Adams, L. S. Martin, M. D. Seaberg, F. Dennis, H. C. Kapteyn, and M. M. Murnane, "A generalization for optimized phase retrieval algorithms," Optics Express, vol. 20, no. 22, pp. 22470–22479, 2012.

[67] D. R. Luke, "Relaxed Averaged Alternating Reflections for Diffraction Imaging," Inverse Problems, vol. 21, no. 1, p. 13, 2004.

[68] G. J. Williams, M. A. Pfeifer, I. A. Vartanyants, and I. K. Robinson, "Three-Dimensional Imaging of Microstructure in Au Nanocrystals," Physical Review Letters, vol. 90, no. 17, p. 175501, 2003.

[69] J. Miao, J. Amonette, Y. Nishino, T. Ishikawa, and K. Hodgson, "Direct determination of the absolute electron density of nanostructured and disordered materials at sub-10-nm resolution," Physical Review B, vol. 68, no. 1, p. 012201, 2003.

[70] H. Chapman, A. Barty, S. Marchesini, A. Noy, S. Hau-Riege, C. Cui, M. Howells, R. Rosen, H. He, J. Spence, and Others, "High-resolution ab initio three-dimensional x-ray diffraction microscopy," JOSA A, vol. 23, no. 5, pp. 1179–1200, 2006.

[71] G. Williams, H. Quiney, B. Dhal, C. Tran, K. Nugent, a. Peele, D. Paterson, and M. de Jonge, "Fresnel Coherent Diffractive Imaging," Physical Review Letters, vol. 97, no. 2, p. 025506, 2006.

[72] H. M. Quiney, a. G. Peele, Z. Cai, D. Paterson, and K. A. Nugent, "Diffractive imaging of highly focused X-ray fields," Nature Physics, vol. 2, no. 2, pp. 101–104, 2006.

[73] J. M. Rodenburg, A. C. Hurst, A. G. Cullis, B. R. Dobson, F. Pfeiffer, O. Bunk, C. David, K. Jefimovs, and I. Johnson, "Hard-X-ray lensless imaging of extended objects," Physical Review Letters, vol. 98, no. 3, pp. 1–4, 2007.

[74] H. Jiang, C. Song, C.-c. Chen, R. Xu, K. S. Raines, B. P. Fahimian, and C.-h. Lu, "Quantitative 3D imaging of whole , unstained cells by using X-ray diffraction microscopy," Proceedings of the National Academy of Sciences, vol. 107, no. 25, pp. 11234–11239, 2010.

[75] M. M. Seibert, T. Ekeberg, F. R. N. C. Maia, M. Svenda, J. Andreasson, O. Joensson, D. Odic, B. Iwan, A. Rocker, D. Westphal, M. Hantke, D. P. DePonte, A. Barty, J. Schulz, L. Gumprecht, N. Coppola, A. Aquila, M. Liang, T. A. White, A. Martin, C. Caleman, S. Stern, C. Abergel, V. Seltzer, J.-M. Claverie, C. Bostedt, J. D. Bozek, S. Boutet, A. A. Miahnahri, M. Messerschmidt, J. Krzywinski, G. Williams, K. O. Hodgson, M. J. Bogan, C. Y. Hampton, R. G. Sierra, D. Starodub, I. Andersson, S. Bajt, M. Barthelmess, J. C. H. Spence, P. Fromme, U. Weierstall, R. Kirian, M. Hunter, R. B. Doak, S. Marchesini, S. P. Hau-Riege, M. Frank, R. L. Shoeman, L. Lomb, S. W. Epp, R. Hartmann, D. Rolles, A. Rudenko, C. Schmidt, L. Foucar, N. Kimmel, P. Holl, B. Rudek, B. Erk, A. Hoemke, C. Reich, D. Pietschner, G. Weidenspointner, L. Strueder, G. Hauser, H. Gorke, J. Ullrich, I. Schlichting, S. Herrmann, G. Schaller, F. Schopper, H. Soltau, K.-U. Kuehnel, R. Andritschke, C.-D. Schroeter, F. Krasniqi, M. Bott, S. Schorb, D. Rupp, M. Adolph, T. Gorkhover, H. Hirsemann, G. Potdevin, H. Graafsma, B. Nilsson, H. N. Chapman, and J. Hajdu, "Single mimivirus particles intercepted and imaged with an X-ray laser," Nature, vol. 470, no. 7332, pp. 78–86, 2011.

[76] C. Dumas, A. Van der Lee, and L. Palatinus, "Lensless coherent imaging of proteins and supramolecular assemblies: Efficient phase retrieval by the charge flipping algorithm," Journal of Structural Biology, vol. 182, no. 2, pp. 106–116, 2013.

[77] B. Zhang, M. D. Seaberg, D. E. Adams, D. F. Gardner, E. R. Shanblatt, J. M. Shaw, W. Chao, E. M. Gullikson, F. Salmassi, H. C. Kapteyn, and M. M. Murnane, "Full field tabletop EUV coherent diffractive imaging in a transmission geometry," Optics Express, vol. 21, p. 21970, sep 2013.

[78] B. Abbey, K. A. Nugent, G. J. Williams, J. N. Clark, A. G. Peele, M. A. Pfeifer, M. De Jonge, and I. McNulty, "Keyhole coherent diffractive imaging," Nature Physics, vol. 4, no. 5, pp. 394–398, 2008.

[79] W. Hoppe, "Diffraction in inhomogeneous primary wave fields. 1. Principle of phase determination from electron diffraction interference," Acta Crystallographica, vol. 495, 1969.

[80] J. M. Rodenburg and H. M. L. Faulkner, "A phase retrieval algorithm for shifting illumination," Applied Physics Letters, vol. 85, no. 20, p. 4795, 2004.

[81] A. M. Maiden and J. M. Rodenburg, "An improved ptychographical phase retrieval algorithm for diffractive imaging," Ultramicroscopy, vol. 109, no. 10, pp. 1256–62, 2009.

[82] F. Zhang, J. Vila-Comamala, A. Diaz, F. Berenguer, R. Bean, B. Chen, A. Menzel, I. K. Robinson, and J. M. Rodenburg, "Translation position determination in ptychographic coherent diffraction imaging," Optics Express, vol. 21, no. 11, p. 13592, 2013.

[83] D. J. Batey, D. Claus, and J. M. Rodenburg, "Information multiplexing in ptychography," Ultramicroscopy, vol. 138, pp. 13–21, 2014.

[84] R. Karl, C. Bevis, R. Lopez-Rios, J. Reichanadter, D. Gardner, C. Porter, E. Shanblatt, M. Tanksalvala, G. F. Mancini, M. Murnane, H. Kapteyn, and D. Adams, "Spatial, spectral, and polarization multiplexed ptychography," Optics Express, vol. 23, no. 23, p. 30250, 2015.

[85] C. S. Bevis, R. Karl-Jr., J. Reichanadter, D. F. Gardner, C. L. Porter, E. R. Shanblatt, M. D. Tanksalvala, G. F. Mancini, H. C. Kapteyn, M. M. Murnane, and D. E. Adams, "Multiple beam ptychography for large field-of-view, high throughput, quantitative phase contrast imaging," Submitted, 2017.

[86] D. F. Gardner, M. Tanksalvala, E. R. Shanblatt, X. Zhang, B. R. Galloway, C. L. Porter, R. Karl-Jr., C. Bevis, D. E. Adams, H. C. Kapteyn, M. M. Murnane, and G. F. Mancini, "Subwavelength coherent imaging of periodic samples using a 13.5 nm tabletop high harmonic light source," Nature Photonics, vol. 11, no. 33, pp. 259–264, 2017.

[87] D. J. Batey, T. B. Edo, C. Rau, U. Wagner, Z. D. Pešić, T. a. Waigh, and J. M. Rodenburg, "Reciprocal-space up-sampling from real-space oversampling in x-ray ptychography," Physical Review A, vol. 89, no. 4, p. 43812, 2014.

[88] A. M. Maiden, M. J. Humphry, F. Zhang, and J. M. Rodenburg, "Superresolution imaging via ptychography.," Journal of the Optical Society of America A, vol. 28, no. 4, pp. 604–12, 2011.

[89] P. Sidorenko, O. Lahav, Z. Avnat, and O. Cohen, "Ptychographic Reconstruction Algorithm for FROG : Supreme Robustness and Super-Resolution," Optica, vol. 3, no. 12, pp. 1320–1330, 2016.

[90] T. H. Maiman, "Stimulated Optical Radiation in Ruby," Nature, vol. 187, no. 4736, pp. 493–494, 1960.

[91] J. T. Bushburg, J. A. Seibert, E. M. Leidholdt Jr., and J. M. Boone, The Essential Physics of Medical Imaging. Philadelphia: Lippincott Williams & Wilkins, 2nd ed., 2002.

[92] E. M. McMillan, "The Synchrotron– A Proposed High Energy Particle Accelerator," Physical Review, vol. 68, no. 143, pp. 1–2, 1945.

[93] E. D. Courant, M. S. Livingston, and H. S. Snyder, "The Strong-Focusing Synchroton–A New High Energy Accelerator," Physical Review, vol. 88, no. 5, pp. 1190–1196, 1952.

[94] Wikipedia, "X-ray - Wikipedia, The Free Encyclopedia," 2017.

[95] Wikipedia, "X-ray tube - Wikipedia, The Free Encyclopedia," 2017.

[96] C. J. Milne, T. J. Penfold, and M. Chergui, "Recent experimental and theoretical developments in time-resolved X-ray spectroscopies," Coordination Chemistry Reviews, vol. 277-278, pp. 44–68, 2014.

[97] F. R. Elder, A. M. Gurewitsch, R. V. Langmuir, and H. C. Pollock, "Radiation from Electrons in a Synchrotron," Physical Review, vol. 71, no. 829, pp. 829–830, 1947.

[98] P. Cloetens, R. Barrett, J. Baruchel, J.-P. Guigay, and M. Schlenker, "Phase objects in synchrotron radiation hard x-ray imaging," Journal of Physics D: Applied Physics, vol. 29, pp. 133–146, 1996.

[99] F. A. Lima, C. J. Milne, D. C. V. Amarasinghe, M. H. Rittmann-frank, R. M. V. D. Veen, M. Reinhard, V.-t. Pham, S. Karlsson, S. L. Johnson, C. Borca, T. Huthwelker, M. Janousch, F. V. Mourik, R. Abela, F. A. Lima, C. J. Milne, D. C. V. Amarasinghe, V.-t. Pham, S. Karlsson, S. L. Johnson, D. Grolimund, R. Abela, and M. Chergui, "A high-repetition rate scheme for synchrotron-based picosecond laser pump / x-ray probe experiments on chemical and biological systems in solution A high-repetition rate scheme for synchrotron-based picosecond laser pump / x-ray probe experiments on chemi," Review of Scientific Instruments, vol. 82, pp. 063111–063116, 2011.

[100] M. Chergui and A. H. Zewail, "Electron and X-Ray Methods of Ultrafast Structural Dynamics: Advances and Applications," ChemPhysChem, vol. 10, pp. 28–43, 2009.

[101] P. Emma, R. Akre, J. Arthur, R. Bionta, C. Bostedt, J. Bozek, A. Brachmann, P. Bucksbaum, R. Coffee, F.-J. Decker, Y. Ding, D. Dowell, S. Edstrom, A. Fisher, J. Frisch, S. Gilevich, J. Hastings, G. Hays, P. Hering, Z. Huang, R. Iverson, H. Loos, M. Messerschmidt, A. Miahnahri, S. Moeller, H.-D. Nuhn, G. Pile, D. Ratner, J. Rzepiela, D. Schultz, T. Smith, P. Stefan, H. Tompkins, J. Turner, J. Welch, W. White, J. Wu, G. Yocky, and J. Galayda, "First lasing and operation of an ängstrom-wavelength free-electron laser," Nature Photonics, vol. 4, no. 9, pp. 641–647, 2010.

[102] H. Wiedemann, Particle Accelerator Physics. New York: Springer, 3rd ed., 2007.

[103] H. Motz, W. Thon, and R. N. Whitehurst, "Experiments on Radiation by Fast Electron Beams," Journal of Applied Physics, vol. 24, no. 7, pp. 826–833, 1953.

[104] D. A. G. Deacon, L. R. Elias, J. M. J. Madey, G. J. Ramian, H. A. Schwettman, and T. I. Smith, "First Operation of a Free-Electron Laser," Physical Review Letters, vol. 38, no. 16, pp. 892–894, 1977.

[105] J. J. Rocca, "Table-top soft x-ray lasers," Review of Scientific Instruments, vol. 70, no. 10, p. 3799, 1999.

[106] D. L. Matthews, P. L. Hagelstein, M. D. Rosen, M. J. Eckart, N. M. Ceglio, A. U. Hazi, H. Medecki, B. J. MacGowan, J. E. Trebes, B. L. Whitten, E. M. Campbell, C. W. Hatcher, A. M. Hawryluk, R. L. Kauffman, L. D. Pleasance, G. Rambach, J. H. Scofield, G. Stone, and T. A. Weaver, "Demonstration of a soft x-ray amplifier," Physical Review Letters, vol. 54, no. 2, pp. 110–113, 1985.

[107] M. D. Rosen, P. L. Hagelstein, D. L. Matthews, E. M. Campbell, A. U. Hazi, B. L. Whitten, B. Macgowan, R. E. Turner, and R. W. Lee, "Exploding-Foil Technique for Achieving a Soft X-Ray Laser M.," Physical Review Letters, vol. 54, no. 2, pp. 106–110, 1985.

[108] J. J. Rocca, V. Shlyaptsev, F. G. Tomasel, O. D. Cortzar, D. Hartshorn, and J. L. A. Chilla, "Demonstration of a discharge pumped table-top soft-x-ray laser," Physical Review Letters, vol. 73, no. 16, pp. 2192–2195, 1994.

[109] C. Baumgarten, M. Pedicone, H. Bravo, H. Wang, L. Yin, C. S. Menoni, J. J. Rocca, and B. A. Reagan, "1 J, 05 kHz repetition rate picosecond laser," Optics Letters, vol. 41, no. 14, p. 3339, 2016.

[110] S. Hooker and C. Webb, Laser Physics. Oxford University Press, 2010.

[111] A. McPherson, G. Gibson, H. Jara, U. Johann, T. S. Luk, I. A. McIntyre, K. Boyer, and C. K. Rhodes, "Studies of multiphoton production of vacuum-ultraviolet," Journal of the Optical Society of America B, vol. 4, no. 4, pp. 595–601, 1987.

[112] M. Ferray, A. L'Huillier, X. F. Li, L. A. Lompre, G. Mainfray, and C. Manus, "Multiple-harmonic conversion of 1064 nm radiation in rare gases," Journal of Physics B, vol. 21, pp. L31—-L35, 1988.

[113] J. L. Krause, K. J. Schafer, and K. C. Kulander, "High-Order Harmonic Generation from Atoms and Ions in the High Intensity Regime," Physical Review Letters, vol. 68, no. 24, pp. 3535–3538, 1992.

[114] M. Lewenstein, Balcou, Ivanov, L'Huillier, and Corkum, "Theory of high-harmonic generation by low-frequency laser fields," Physical Review A, vol. 49, no. 3, pp. 2117–2132, 1994.

[115] A. Rundquist, C. G. Durfee, Z. Chang, C. Herne, S. Backus, M. M. Murnane, and H. C. Kapteyn, "Phase-Matched Generation of Coherent Soft X-rays," Science, vol. 280, no. 1412, pp. 1412–1415, 1998.

[116] T. Popmintchev, M.-C. Chen, D. Popmintchev, P. Arpin, S. Brown, S. Alisauskas, G. Andriukaitis, T. Balciunas, O. D. Mücke, A. Pugzlys, A. Baltuska, B. Shim, S. E. Schrauth, A. Gaeta, C. Hernández-García, L. Plaja, A. Becker, A. Jaron-Becker, M. M. Murnane, and H. C. Kapteyn, "Bright coherent ultrahigh harmonics in the keV x-ray regime from mid-infrared femtosecond lasers.," Science, vol. 336, no. 6086, pp. 1287–91, 2012.

[117] P. B. Corkum, "Plasma perspective on strong field multiphoton ionization," Physical Review Letters, vol. 71, no. 13, pp. 1994–1997, 1993.

[118] J. Zhou, J. Peatross, M. Murnane, H. Kapteyn, and I. Christov, "Enhanced High-Harmonic Generation Using 25 fs Laser Pulses," Physical Review Letters, vol. 76, no. 5, pp. 752–755, 1996.

[119] C. G. Durfee, A. R. Rundquist, S. Backus, C. Herne, M. M. Murnane, and H. C. Kapteyn, "Phase Matching of High-Order Harmonics in Hollow Waveguides," Physical Review Letters, vol. 83, no. 11, pp. 2187–2190, 1999.

[120] T. Popmintchev, M.-C. Chen, P. Arpin, M. M. Murnane, and H. C. Kapteyn, "The attosecond nonlinear optics of bright coherent X-ray generation," Nature Photonics, vol. 4, no. 12, pp. 822–832, 2010.

[121] C. Ding, W. Xiong, T. Fan, D. D. Hickstein, T. Popmintchev, X. Zhang, M. Walls, M. M. Murnane, and H. C. Kapteyn, "High flux coherent super-continuum soft X-ray source driven by a single-stage, 10mJ, Ti:sapphire amplifier-pumped OPA.," Optics express, vol. 22, no. 5, pp. 6194–6202, 2014.

[122] P. B. Corkum and F. Krausz, "Attosecond science," Nature Physics, vol. 3, pp. 381–387, 2007.

[123] H. C. Kapteyn, M. M. Murnane, and I. P. Christov, "Extreme Nonlinear Optics: Coherent X Rays from Lasers," Physics Today, vol. 58, no. 3, pp. 39–46, 2005.

[124] A. L'Huillier and P. Balcou, "High-Order Harmonic Generation in Rare Gases with a 1-ps 1053-nm Laser," Physical Review Letters, vol. 70, no. 6, pp. 774–777, 1993.

[125] D. D. Hickstein, F. J. Dollar, P. Grychtol, J. L. Ellis, R. Knut, C. Hernández-garcía, D. Zusin, C. Gentry, J. M. Shaw, T. Fan, K. M. Dorney, A. Becker, A. Jaro, H. C. Kapteyn, M. M. Murnane, and C. G. Durfee, "Non-collinear generation of angularly isolated circularly polarized high harmonics," Nature Photonics, vol. 9, pp. 743–750, 2015.

[126] S. Ghimire, A. D. Dichiara, E. Sistrunk, P. Agostini, L. F. Dimauro, and D. A. Reis, "Observation of high-order harmonic generation in a bulk crystal," Nature Physics, vol. 7, no. 2, pp. 138–141, 2010.

[127] M.-C. Chen, P. Arpin, T. Popmintchev, M. Gerrity, B. Zhang, M. Seaberg, D. Popmintchev, M. M. Murnane, and H. C. Kapteyn, "Bright, Coherent, Ultrafast Soft X-Ray Harmonics Spanning the Water Window from a Tabletop Light Source," Physical Review Letters, vol. 105, no. 17, p. 173901, 2010.

[128] D. J. Kane and R. Trebino, "Characterization of Arbitrary Femtosecond Pulses Using Frequency-Resolved Optical Gating," IEEE Journal of Quanum Electronics, vol. 29, no. 2, pp. 571–579, 1993.

[129] K. W. Delong and R. Trebino, "Frequency-resolved optical gating with the use of second-harmonic generation," Journal of the Optical Society of America B, vol. 11, no. 11, pp. 2206–2215, 1994.

[130] D. J. Kane, A. J. Taylor, R. Trebino, and K. W. Delong, "Single-shot measurement of the intensity and phase of a femtosecond UV laser pulse with frequency-resolved optical gating," Optics Letters, vol. 19, no. 14, pp. 1061–1063, 1994.

[131] R. Trebino, Frequency-Resolved Optical Gating : The Measurement of Ultrashort Laser Pulses. New York: Springer, 2002.

[132] P. Sidorenko and O. Cohen, "Single-shot ptychography," Optica, vol. 3, no. 1, 2016.

[133] V. V. Lozovoy, I. Pastirk, and M. Dantus, "Multiphoton intrapulse interference . IV . Ultrashort laser pulse spectral phase characterization and compensation," Optics Letters, vol. 29, no. 7, pp. 775–777, 2004.

[134] B. Xu, J. M. Gunn, J. M. D. Cruz, V. V. Lozovoy, and M. Dantus, "Quantitative investigation of the multiphoton intrapulse interference phase scan method for simultaneous phase measurement and compensation of femtosecond laser pulses," Journal of the Optical Society of America B, vol. 23, no. 4, pp. 750–759, 2006.

[135] B. L. Henke, E. M. Gullikson, and J. C. Davis, "X-Ray Interactions: Photoabsorption, Scattering, Transmission, and Reflection at E = 50-30,000 eV, Z = 1-92," 1993.

[136] M. Zürch, C. Kern, and C. Spielmann, "Xuv coherent diffraction imaging in reflection geometry with low numerical aperture," Optics Express, vol. 21, no. 18, pp. 21131–21147, 2013.

[137] T. Sun, Z. Jiang, J. Strzalka, L. Ocola, and J. Wang, "Three-dimensional coherent X-ray surface scattering imaging near total external reflection," Nature Photonics, vol. 6, no. 9, pp. 586–590, 2012.

[138] T. Harada, M. Nakasuji, Y. Nagata, T. Watanabe, and H. Kinoshita, "Phase imaging of extreme-ultraviolet mask using coherent extreme-ultraviolet scatterometry microscope," Japanese Journal of Applied Physics, vol. 52, no. 6, pp. 2–7, 2013.

[139] S. Roy, D. Parks, K. A. Seu, R. Su, J. J. Turner, W. Chao, E. H. Anderson, S. Cabrini, and S. D. Kevan, "Lensless X-ray imaging in reflection geometry," Nature Photonics, vol. 5, no. 4, pp. 243–245, 2011.

[140] D. L. Windt, "IMD–Software for modeling the optical properties of multilayer films," Computers in Physics, vol. 12, no. 4, pp. 360–370, 1998.

[141] M. G. Moharam, E. B. Grann, D. a. Pommet, and T. K. Gaylord, "Formulation for stable and efficient implementation of the rigorous coupled-wave analysis of binary gratings," Journal of the Optical Society of America A, vol. 12, no. 5, p. 1068, 1995.

[142] T. Ohtsuka, M. Masuda, and N. Sato, "Ellipsometric Study of Anodic Oxide Films on Titanium in Hydrochloric Acid, Sulfuric Acid, and Phosphate Solution," J. Electrochem. Soc., vol. 132, no. 4, pp. 787–792, 1985.

[143] M. Advincula, X. Fan, J. Lemons, and R. Advincula, "Surface modification of surface sol gel derived titanium oxide films by self-assembled monolayers (SAMs) and non-specific protein adsorption studies," Colloids and Surfaces B, vol. 42, pp. 29–43, 2005.

[144] P. Thibault and A. Menzel, "Reconstructing state mixtures from diffraction measurements," Nature, vol. 494, no. 7435, pp. 68–71, 2013.

[145] B. Zhang, D. F. Gardner, M. H. Seaberg, E. R. Shanblatt, C. L. Porter, R. Karl, C. A. Mancuso, H. C. Kapteyn, M. M. Murnane, and D. E. Adams, "Ptychographic hyperspectral spectromicroscopy with an extreme ultraviolet high harmonic comb," Optics Express, vol. 24, no. 16, pp. 18745–18754, 2016.

[146] H. Niedrig and E. I. Rau, "Information depth and spatial resolution in BSE microtomography in SEM," Nuclear Instruments and Methods in Physics Research Section B, vol. 142, no. 4, pp. 523–534, 1998.

[147] S. L. Erlandsen, P. T. Macechko, and C. Frethem, "High resolution backscatter electron (BSE) imaging of immunogold with in-lens and below-the-lens field emission scanning electron microscopes," Scanning Microscopy International, vol. 13, no. 1, pp. 43–54, 1999.

[148] G. E. Lloyd, "Atomic Number and Crystallographic Contrast Images with the SEM: A Review of Backscattered Electron Techniques," Mineralogical Magazine, vol. 51, no. 359, pp. 3–19, 1987.

[149] P. Vitry, E. Bourillot, C. Plassard, Y. Lacroute, E. Calkins, L. Tetard, and E. Lesniewska, "Mode-synthesizing atomic force microscopy for 3D reconstruction of embedded low-density dielectric nanostructures," Nano Research, vol. 8, no. 7, pp. 1–7, 2015.

[150] G. S. Shekhawat and V. P. Dravid, "Nanoscale imaging of buried structures via scanning near-field ultrasound holography.," Science, vol. 310, no. 5745, pp. 89–92, 2005.

[151] C. Song, R. Bergstrom, D. Ramunno-Johnson, H. Jiang, D. Paterson, M. D. de Jonge, I. McNulty, J. Lee, K. L. Wang, and J. Miao, "Nanoscale Imaging of Buried Structures with Elemental Specificity Using Resonant X-Ray Diffraction Microscopy," Physical Review Letters, vol. 100, no. 2, p. 25504, 2008.

[152] R. A. Bartels, A. Paul, H. Green, H. C. Kapteyn, M. Margaret, S. Backus, I. P. Christov, Y. Liu, D. Attwood, R. A. Bartels, A. Paul, H. Green, H. C. Kapteyn, M. M. Murnane, S. Backus, I. P. Christov, Y. Liu, D. Attwood, and C. Jacobsen, "Generation of Spatially Coherent Light at Extreme Ultraviolet Wavelengths," Science, vol. 297, no. 5580, pp. 376–378, 2002.

[153] H. N. Chapman, "X-ray imaging beyond the limits.," Nature materials, vol. 8, no. 4, pp. 299–301, 2009.

[154] J. Miao, T. Ishikawa, I. K. Robinson, and M. M. Murnane, "Beyond crystallography: Diffractive imaging using coherent x-ray light sources," Science, vol. 348, no. 6234, pp. 530–535, 2015.

[155] I. Robinson and R. Harder, "Coherent x-ray diffraction imaging of strain at the nanoscale," Nature materials, vol. 8, no. 4, pp. 291–298, 2009.

[156] R. Harder and I. K. Robinson, "Coherent X-ray diffraction imaging of morphology and strain in nanomaterials," JOM, vol. 65, no. 9, pp. 1202–1207, 2013.

[157] H. Jiang, C. Song, C.-C. Chen, R. Xu, K. S. Raines, B. P. Fahimian, C.-h. Lu, T.-K. Lee, A. Nakashima, J. Urano, T. Ishikawa, F. Tamanoi, and J. Miao, "Quantitative 3D imaging of whole, unstained cells by using X-ray diffraction microscopy.," Proceedings of the National Academy of Sciences, vol. 107, no. 25, pp. 11234–11239, 2010.

[158] X. Huang, J. Nelson, J. Kirz, E. Lima, S. Marchesini, H. Miao, A. Neiman, D. Shapiro, J. Steinbrener, A. Stewart, and Others, "Soft x-ray diffraction microscopy of a frozen hydrated yeast cell," Physical review letters, vol. 103, no. 19, p. 198101, 2009.

[159] X. Huang, J. Nelson, J. Kirz, E. Lima, S. Marchesini, H. Miao, A. M. Neiman, D. Shapiro, J. Steinbrener, A. Stewart, J. J. Turner, and C. Jacobsen, "Soft X-Ray Diffraction Microscopy of a Frozen Hydrated Yeast Cell," Physical Review Letters, vol. 103, no. 19, p. 198101, 2009.

[160] P. Thibault, M. Dierolf, A. Menzel, O. Bunk, C. David, and F. Pfeiffer, "High-Resolution Scanning X-ray Diffraction Microscopy," Science, vol. 321, no. 5887, pp. 379–382, 2008.

[161] K. Hummler, B. Sapp, J. R. Lloyd, S. Kruger, S. Olson, S. B. Park, B. Murray, D. Jung, S. Cain, A. Park, D. Ferrone, and I. Ali, "TSV and Cu-Cu direct bond wafer and package-level reliability," Proceedings of Electronic Components and Technology Conference, pp. 41–48, 2013.

[162] B. Zhang, D. F. Gardner, M. H. Seaberg, E. R. Shanblatt, C. L. Porter, R. Karl, C. A. Mancuso, H. C. Kapteyn, M. M. Murnane, and D. E. Adams, "Ptychographic hyperspectral spectromicroscopy with an extreme ultraviolet high harmonic comb," Optics Express, vol. 24, no. 16, pp. 18745–18754, 2016.

[163] P. Thibault, M. Dierolf, O. Bunk, A. Menzel, and F. Pfeiffer, "Probe retrieval in ptychographic coherent diffractive imaging.," Ultramicroscopy, vol. 109, no. 4, pp. 338–43, 2009.

[164] E. Mortensen and W. Barrett, "Intelligent Scissors for Image Composition," Computer Graphics, pp. 191–198, 1995.

[165] L. Névot and P. Croce, "Caractérisation des surfaces par réflexion rasante de rayons X. Application à l'étude du polissage de quelques verres silicates," Revue de Physique Appliquée, vol. 15, no. 3, pp. 761–779, 1980.

[166] D. G. Stearns, "The scattering of x rays from nonideal multilayer structures," Journal of Applied Physics, vol. 65, no. 2, p. 491, 1989.

[167] M. W. Chase Jr., "NIST-JANAF Thermochemical Tables," J. Phys. Chem Ref. Data Monograph, vol. 9, pp. 1–1951, 1998.

[168] P. Heitjans and J. Kärger, Diffusion in Condensed Matter. Boston: Birkhauser, 2nd ed., 2005.

[169] S. Hofmann, "Sputter depth profiling: past, present, and future," Surface and Interface Analysis, vol. 46, no. 10-11, pp. 654–662, 2014.

[170] S. Roberts and P. Dobson, "Evidence for reaction at the AI-SiO2 interface," Journal of Physics D: Applied Physics, vol. 14, no. 6, pp. L17–L22, 1981.

[171] L. J. Zeng, T. Greibe, S. Nik, P. Delsing, and E. Olsson, "Interdiffusion at the Al / SiO 2 interface in Al / AlO x / Al Josephson junctions," in Proc. of the 15th European Microscopy Congress, vol. 15, 2012.

[172] P. Keil, D. Lützenkirchen-Hecht, and R. Frahm, "Investigation of room temperature oxidation of Cu in air by Yoneda-XAFS," AIP Conference Proceedings, vol. 882, pp. 490–492, 2006.

[173] J. Zhang, J. Fan, J. Zhang, Z. Sun, Q. Huang, and H. Jiang, "Three-dimensional coherent diffraction imaging of Mie-scattering spheres by laser single-orientation measurement," Chinese Physics B, vol. 24, no. 9, p. 94201, 2015.

[174] D. Sayre, "Prospects for long wavelength X-Ray microscopy and diffraction," Imaging processes and coherence in physics, vol. 112, pp. 229–235, 1980.

[175] J. Miao, D. Sayre, and H. N. Chapman, "Phase retrieval from the magnitude of the Fourier transforms of nonperiodic objects," Journal of the Optical Society of America A, vol. 15, no. 6, p. 1662, 1998.

[176] T. B. Edo, D. J. Batey, a. M. Maiden, C. Rau, U. Wagner, Z. D. Pešić, T. a. Waigh, and J. M. Rodenburg, "Sampling in x-ray ptychography," Physical Review A, vol. 87, no. 5, p. 053850, 2013.

[177] A. M. Maiden, M. J. Humphry, and J. M. Rodenburg, "Ptychographic transmission microscopy in three dimensions using a multi-slice approach," Journal of the Optical Society of America A, vol. 29, no. 8, pp. 1606–14, 2012.

[178] T. M. Godden, R. Suman, M. J. Humphry, J. M. Rodenburg, and a. M. Maiden, "Ptychographic microscope for three-dimensional imaging," Optics express, vol. 22, no. 10, pp. 12513–23, 2014.

[179] D. F. Gardner Jr., Coherent Diffractive Imaging Near the Spatio-Temporal Limit with High-Harmonic Sources. Phd thesis, University of Colorado, 2017.

[180] R. E. Alvarez and A. Macovski, "Energy-selective reconstructions in X-ray computerized tomography.," Physics in medicine and biology, vol. 21, no. 5, pp. 733–744, 1976.

[181] D. J. Brenner and E. J. Hall, "Computed tomography–an increasing source of radiation exposure.," The New England journal of medicine, vol. 357, no. 22, pp. 2277–2284, 2007.

[182] E. H. R. Tsai, I. Usov, A. Diaz, A. Menzel, and M. Guizar-Sicairos, "X-ray ptychography with extended depth of field," Optics Express, vol. 24, no. 25, pp. 1–11, 2016.

[183] A. Devaney, "A filtered backpropagation algorithm for diffraction tomography," Ultrasonic Imaging, vol. 4, no. 4, pp. 336–350, 1982.

[184] W. S. Haddad, J. E. Trebes, E. H. Anderson, R. A. Levesque, and L. Yang, "Ultrahigh-Resolution X-ray Tomography," Science, vol. 266, pp. 1213–1215, 1994.

[185] W. Denk and H. Horstmann, "Serial block-face scanning electron microscopy to reconstruct three-dimensional tissue nanostructure," PLoS Biology, vol. 2, no. 11, 2004.

[186] B. Chen, M. Guizar-Sicairos, G. Xiong, L. Shemilt, A. Diaz, J. Nutter, N. Burdet, S. Huo, J. Mancuso, A. Monteith, F. Vergeer, A. Burgess, and I. Robinson, "Three-dimensional structure analysis and percolation properties of a barrier marine coating.," Scientific reports, vol. 3, p. 1177, 2013.

[187] R. Xu, H. Jiang, C. Song, J. A. Rodriguez, Z. Huang, C.-C. Chen, D. Nam, J. Park, M. Gallagher-Jones, S. Kim, S. Kim, A. Suzuki, Y. Takayama, T. Oroguchi, Y. Takahashi, J. Fan, Y. Zou, T. Hatsui, Y. Inubushi, T. Kameshima, K. Yonekura, K. Tono, T. Togashi, T. Sato, M. Yamamoto, M. Nakasako, M. Yabashi, T. Ishikawa, and J. Miao, "Single-shot three-dimensional structure determination of nanocrystals with femtosecond X-ray free-electron laser pulses," Nature Communications, vol. 5, pp. 1–9, 2014.

[188] M. V. Holt, S. O. Hruszkewycz, C. E. Murray, J. R. Holt, D. M. Paskiewicz, and P. H. Fuoss, "Strain Imaging of Nanoscale Semiconductor Heterostructures with X-Ray Bragg Projection Ptychography," Physical Review Letteres, vol. 112, pp. 1–6, 2014.

[189] S. O. Hruszkewycz, M. Allain, M. V. Holt, C. E. Murray, J. R. Holt, P. H. Fuoss, and V. Chamard, "High-resolution three-dimensional structural microscopy by single-angle Bragg ptychography," Nature Materials, vol. 1, 2016.

[190] K. S. Raines, S. Salha, R. L. Sandberg, H. Jiang, J. A. Rodríguez, B. P. Fahimian, H. C. Kapteyn, J. Du, and J. Miao, "Three-dimensional structure determination from a single view," Nature, vol. 463, no. 7278, p. 30, 2010.

[191] P. Thibault, "Feasibility of 3D reconstructions from a single 2D diffraction measurement," arXiv 0909.1643.

[192] M. Mutzafi, Y. Shechtman, Y. C. Eldar, O. Cohen, and M. Segev, "Sparsity-based Ankylography for Recovering 3D molecular structures from single-shot 2D scattered light intensity.," Nature communications, vol. 6, p. 7950, 2015.

[193] J. Miao, T. Ishikawa, B. Johnson, E. H. Anderson, B. Lai, and K. O. Hodgson, "High resolution 3D X-ray diffraction microscopy," Physical Review Letters, vol. 89, no. 8, pp. 0883031–0883034, 2002.

[194] Y. Nishino, Y. Takahashi, N. Imamoto, T. Ishikawa, and K. Maeshima, "Three-Dimensional Visualization of a Human Chromosome Using Coherent X-ray Diffraction," Physical Review Letters, vol. 102, no. 018101, pp. 018101–018104, 2009.

[195] T. Ekeberg, M. Svenda, C. Abergel, F. R. N. C. Maia, V. Seltzer, J.-M. Claverie, M. Hantke, O. Jönsson, C. Nettelblad, G. van der Schot, M. Liang, D. P. DePonte, A. Barty, M. M. Seibert, B. Iwan, I. Andersson, N. D. Loh, A. V. Martin, H. Chapman, C. Bostedt, J. D. Bozek, K. R. Ferguson, J. Krzywinski, S. W. Epp, D. Rolles, A. Rudenko, R. Hartmann, N. Kimmel, and J. Hajdu, "Three-Dimensional Reconstruction of the Giant Mimivirus Particle with an X-Ray Free-Electron Laser," Physical Review Letters, vol. 114, pp. 1–6, 2015.

[196] J. Miao and O. Levi, "Equally sloped tomography with oversampling reconstruction," Physical Review B, vol. 72, no. 052103, pp. 1–4, 2005.

[197] G. Schneider, P. Guttmann, S. Heim, S. Rehbein, F. Mueller, K. Nagashima, J. B. Heymann, W. G. Müller, and J. G. McNally, "Three-dimensional cellular ultrastructure resolved by X-ray microscopy.," Nature methods, vol. 7, no. 12, pp. 985–987, 2010.

[198] M. Guizar-Sicairos, A. Diaz, M. Holler, M. S. Lucas, A. Menzel, R. a. Wepf, and O. Bunk, "Phase tomography from x-ray coherent diffractive imaging projections," Optics Express, vol. 19, no. 22, p. 21345, 2011.

[199] F. Song, P. Chen, D. Sun, M. Wang, L. Dong, D. Liang, R.-M. Xu, P. Zhu, and G. Li, "Cryo-EM study of the chromatin fiber reveals a double helix twisted by tetranucleosomal units.," Science, vol. 344, no. 6182, pp. 376–380, 2014.

[200] M. Dierolf, A. Menzel, P. Thibault, P. Schneider, C. M. Kewish, R. Wepf, O. Bunk, and F. Pfeiffer, "Ptychographic X-ray computed tomography at the nanoscale.," Nature, vol. 467, no. 7314, pp. 436–439, 2010.

[201] M. Holler, A. Diaz, M. Guizar-Sicairos, P. Karvinen, E. Färm, E. Härkönen, M. Ritala, A. Menzel, J. Raabe, and O. Bunk, "X-ray ptychographic computed tomography at 16 nm isotropic 3D resolution," Scientific reports, vol. 4, p. 3857, 2014.

[202] M. B. Luu, G. a. van Riessen, B. Abbey, M. W. M. Jones, N. W. Phillips, K. Elgass, M. D. Junker, D. J. Vine, I. McNulty, G. a. Cadenazzi, C. Millet, L. Tilley, K. a. Nugent, and A. G. Peele, "Fresnel coherent diffractive imaging tomography of whole cells in capillaries," New Journal of Physics, vol. 16, p. 093012, 2014.

[203] A. Diaz, B. Malkova, M. Holler, M. Guizar-Sicairos, E. Lima, V. Panneels, G. Pigino, A. G. Bittermann, L. Wettstein, T. Tomizaki, O. Bunk, G. Schertler, T. Ishikawa, R. Wepf, and A. Menzel, "Three-dimensional mass density mapping of cellular ultrastructure by ptychographic X-ray nanotomography," Journal of Structural Biology, vol. 192, no. 3, pp. 461–469, 2015.

[204] K. Giewekemeyer, C. Hackenberg, A. Aquila, R. Wilke, M. Groves, R. Jordanova, V. Lamzin, G. Borchers, K. Saksl, A. Zozulya, M. Sprung, and A. Mancuso, "Tomography of a Cryo-immobilized Yeast Cell Using Ptychographic Coherent X-Ray Diffractive Imaging," Biophysical Journal, vol. 109, no. 9, pp. 1986–1995, 2015.

[205] C. Donnelly, M. Guizar-Sicairos, V. Scagnoli, M. Holler, T. Huthwelker, A. Menzel, I. Vartiainen, E. Müller, E. Kirk, S. Gliga, J. Raabe, and L. J. Heyderman, "Element-Specific X-Ray Phase Tomography of 3D Structures at the Nanoscale," Physical Review Letters, vol. 114, no. 11, pp. 1–5, 2015.

[206] M. Holler, M. Guizar-Sicairos, E. H. R. Tsai, R. Dinapoli, E. Müller, O. Bunk, J. Raabe, and G. Aeppli, "High-resolution non-destructive three- dimensional imaging of integrated circuits," Nature, vol. 543, p. 402, 2017.

[207] M. Guizar-Sicairos, J. J. Boon, K. Mader, A. Diaz, A. Menzel, and O. Bunk, "Quantitative interior x-ray nanotomography by a hybrid imaging technique," Optica, vol. 2, no. 3, pp. 259–266, 2015.

[208] M. Stockmar, M. Hubert, M. Dierolf, B. Enders, R. Clare, S. Allner, A. Fehringer, I. Zanette, J. Villanova, J. Laurencin, P. Cloetens, F. Pfeiffer, and P. Thibault, "X-ray nanotomography using near-field ptychography," Optics Express, vol. 23, no. 10, p. 12720, 2015.

[209] A. Suzuki, S. Furutaku, K. Shimomura, K. Yamauchi, Y. Kohmura, T. Ishikawa, and Y. Takahashi, "High-resolution multislice X-ray ptychography of extended thick objects," Physical Review Letters, vol. 112, pp. 1–5, 2014.

[210] K. Shimomura, A. Suzuki, M. Hirose, and Y. Takahashi, "Precession x-ray ptychography with multislice approach," Physical Review B, vol. 91, no. 21, p. 214114, 2015.

[211] E. R. Shanblatt, C. S. Bevis, G. F. Mancini, M. D. Tanksalvala, R. Karl-Jr., C. L. Porter, B. Wang, P. Johnsen, P. Moradifar, D. E. Adams, H. C. Kapteyn, J. Badding, and M. M. Murnane, "Three dimensional microscopy of silicon-infiltrated biological samples with a 12.7 nm tabletop high-harmonic light source," In preparation, 2017.

[212] K. M. Hoogeboom-pot, J. N. Hernandez-charpak, X. Gu, T. D. Frazer, and E. H. Anderson, "A new regime of nanoscale thermal transport: Collective diffusion increases dissipation efficiency," Proceedings of the National Academy of Sciences, vol. 112, no. 16, pp. 4846–4851, 2015.

[213] K. M. Hoogeboom-pot, E. Turgut, J. N. Hernandez-charpak, J. M. Shaw, H. C. Kapteyn, M. M. Murnane, and D. Nardi, "Nondestructive Measurement of the Evolution of Layer-Specific Mechanical Properties in Sub-10 nm Bilayer Films," Nano Letters, vol. 16, pp. 4772–4778, 2016.

[214] J. N. Hernandez-Charpak, K. M. Hoogeboom-pot, Q. Li, T. D. Frazer, J. L. Knobloch, M. Tripp, S. W. King, E. H. Anderson, W. Chao, M. M. Murnane, H. C. Kapteyn, and D. Nardi, "Full Characterization of the Mechanical Properties of 11 - 50 nm Ultrathin Films: Influence of Network Connectivity on the Poisson's Ratio," Nano Letters, vol. 17, pp. 2178–2183, 2017.

[215] P. Müller, M. Schürmann, and J. Guck, "The Theory of Diffraction Tomography," arXiv.org, vol. q-bio.QM, p. 466, 2015.

[216] E. Lee, B. P. Fahimian, C. V. Iancu, C. Suloway, G. E. Murphy, E. R. Wright, D. Castaño-díez, G. J. Jensen, and J. Miao, "Radiation dose reduction and image enhancement in biological imaging through equally-sloped tomography," Journal of Structural Biology, vol. 164, no. 2, pp. 221–227, 2008.

[217] C.-c. Chen, J. Miao, and T. K. Lee, "Tomographic image alignment in three-dimensional coherent diffraction microscopy," Physical Review A, vol. 79, no. 052102, pp. 1–4, 2009.

[218] H. Jiang, R. Xu, C.-C. Chen, W. Yang, J. Fan, X. Tao, C. Song, Y. Kohmura, T. Xiao, Y. Wang, Y. Fei, T. Ishikawa, W. L. Mao, and J. Miao, "Three-Dimensional Coherent X-Ray Diffraction Imaging of Molten Iron in Mantle Olivine at Nanoscale Resolution," Physical Review Letters, vol. 110, no. 20, p. 205501, 2013.

[219] Z. Tao, C. Chen, T. Szilvasi, M. Keller, M. Mavrikakis, H. Kapteyn, and M. Murnane, "Direct time-domain observation of attosecond final-state lifetimes in photoemission from solids," Science, vol. 353, no. 6294, pp. 62–67, 2016.

[220] R. Karl Jr., G. Mancini, D. Gardner, E. Shanblatt, J. Knobloch, T. Frazer, J. N. Hernandez-Charpak, B. Abad Mayor, M. Tanksalvala, C. Porter, C. Bevis, H. Kapteyn, M. Murnane, and D. Adams, "Ultrafast coherent diffractive imaging of acoustic waves in nanostructures," In preparation, 2017.

[221] E. Turgut, C. La-o vorakiat, J. M. Shaw, P. Grychtol, H. T. Nembach, D. Rudolf, R. Adam, M. Aeschlimann, C. M. Schneider, T. J. Silva, M. M. Murnane, H. C. Kapteyn, and S. Mathias, "Controlling the Competition between Optically Induced Ultrafast Spin-Flip Scattering and Spin Transport in Magnetic Multilayers," Physical Review Letters, vol. 110, no. 19, p. 197201, 2013.

[222] E. Turgut, E. Zusin, D. Legut, K. Carva, R. Knut, J. Shaw, H. Nembach, T. Silva, S. Mathias, M. Aeschlimann, P. Oppeneer, H. Kapteyn, M. Murnane, and P. Grychtol, "Stoner versus Heisenberg: Ultrafast exchange reduction and magnon generation during laser-induced demagnetization," Physical Review B, vol. 94, no. 22, 2016.

[223] T. Fan, P. Grychtol, R. Knut, C. Hernandez-Garcia, D. D. Hickstein, D. Zusin, C. Gentry, F. J. Dollar, C. A. Mancuso, C. W. Hogle, O. Kfir, D. Legut, K. Carva, J. L. Ellis, K. M. Dorney, C. Chen, O. G. Shpyrko, E. E. Fullerton, O. Cohen, P. M. Oppeneer, D. B. Milosevic, A. Becker, A. A. Jaron-Becker, T. Popmintchev, M. M. Murnane, and H. C. Kapteyn, "Bright circularly polarized soft X-ray high harmonics for X-ray magnetic circular dichroism," Proceedings of the National Academy of Sciences of the United States of America, vol. 112, no. 46, pp. 14206–14211, 2015.

[224] G. F. Mancini, T. Latychevskaia, F. Pennacchio, J. Reguera, F. Stellacci, and F. Carbone, "Order/Disorder Dynamics in a Dodecanethiol-Capped Gold Nanoparticles Supracrystal by Small-Angle Ultrafast Electron Diffraction," Nano Letters, vol. 16, no. 4, pp. 2705–2713, 2016.

[225] R. Xu, C.-C. Chen, L. Wu, M. C. Scott, W. Theis, C. Ophus, M. Bartels, Y. Yang, H. Ramezani-Dakhel, M. R. Sawaya, H. Heinz, L. D. Marks, P. Ercius, and J. Miao, "Three-dimensional coordinates of individual atoms in materials revealed by electron tomography," Nature Materials, vol. 14, p. 23, 2015.

[226] J. Miao, P. Ercius, and S. J. L. Billinge, "Atomic electron tomography: 3D structures without crystals," Science, vol. 353, no. 6306, p. 2157, 2016.

[227] N. Sarukura, Y. Ishida, H. Nakano, and Y. Yamamoto, "CW passive mode locking of a Ti:sapphire laser," Applied Physics Letters, vol. 56, no. 814, pp. 814–815, 1990.

[228] D. E. Spence, J. M. Evans, W. E. Sleat, and W. Sibbett, "Regeneratively initiated self-mode-locked Ti : sapphire laser," Optics Letters, vol. 16, no. 22, pp. 1762–1764, 1991.

[229] N. Sarukura, Y. Ishida, and H. Nakano, "Generation of 50-fs pulses from a pulse-compressed, cw, passively mode-locked Ti:sapphire laser," Optics Letters, vol. 16, no. 3, pp. 153–155, 1991.

[230] D. E. Spence, P. N. Kean, and W. Sibbett, "60-fsec pulse generation from a self-mode-locked Ti:sapphire laser," Optics Letters, vol. 16, no. 1, pp. 42–44, 1991.

[231] U. Keller, G. W. T'Hooft, W. H. Knox, and J. E. Cunningham, "Femtosecond pulses from a continuously self-starting passively mode-locked Ti:sapphire laser," Optics Letters, vol. 16, no. 13, pp. 1022–1024, 1991.

[232] C. P. Huang, M. T. Asaki, S. Backus, M. M. Murnane, H. C. Kapteyn, and H. Nathel, "17-fs pulses from a self-mode-locked Ti:sapphire laser.," Optics letters, vol. 17, no. 18, pp. 1289–1291, 1992.

[233] M. T. Asaki, C.-P. Huang, D. Garvey, J. Zhou, H. C. Kapteyn, and M. M. Murnane, "Generation of 11-fs pulses from a self-mode-locked Ti:sapphire laser," Optics Letters, vol. 18, no. 12, p. 977, 1993.

[234] I. P. Christov, V. D. Stoev, M. M. Murnane, and H. C. Kapteyn, "Sub-10-fs operation of Kerr-lens mode-locked lasers.," Optics letters, vol. 21, no. 18, pp. 1493–5, 1996.

[235] R. W. Boyd, Nonlinear Optics. San Diego: Elsevier, 3rd ed., 2008.

[236] A. L. Lytle, Phase Matching and Coherence of High-Order Harmonic Generation in Hollow Waveguides. Phd thesis, University of Colorado, 2001.

[237] A. M. Weiner, J. P. Heritage, and E. M. Kirschner, "High-resolution femtosecond pulse shaping," Journal of the Optical Society of America B, vol. 83, no. 8, p. 5391, 1988.

[238] R. Bartels, S. Backus, E. Zeek, L. Misoguti, G. Vdovin, I. P. Christov, M. M. Murnane, and H. C. Kapteyn, "Shaped-pulse optimization of coherent emission of high-harmonic soft x-rays," Nature, vol. 406, no. 6792, pp. 164–6, 2000.

[239] M. D. Seaberg, Nanoscale EUV Microscopy on a Tabletop: A General Transmission and Reflection Mode Microscope Based on Coherent Diffractive Imaging with High Harmonic Illumination. Phd, University of Colorado, 2014.

[240] M. C. Chen, J. Y. Huang, Q. Yang, C. L. Pan, and J.-I. Chyi, "Freezing phase scheme for fast adaptive control and its application to characterization of femtosecond coherent optical pulses reflected from semiconductor saturable absorber mirrors," Journal of the Optical Society of America B, vol. 22, no. 5, p. 1134, 2005.

[241] S. Backus, C. G. Durfee, M. M. Murnane, and H. C. Kapteyn, "High power ultrafast lasers," Review Of Scientific Instruments, vol. 69, no. 3, pp. 1207–1223, 1998.

Appendix A

Gaussian Beam Parameters

An important and useful formalism to understand when considering laser physics is Gaussian beam propagation. Many lasers produce Gaussian beams, that is, beams which have a Gaussian cross section and can be described by the following equations [110],

$$E(r,z) = E_0 \frac{\omega_0}{w(z)} exp(-\frac{r^2}{w(z)^2}) exp\big(-i(kz + k\frac{r^2}{2R(z)}) - \psi(z)\big) \tag{A.1}$$

where E_0 is the amplitude, w_0 is the transverse beam radius at the focus, (or "waist"), $w(z)$ is the beam radius at a certain distance z, k is the wavenumber $2\pi/\lambda$, $R(z)$ is the radius of curvature at a certain distance z, and $\psi(z)$ is the Guoy phase at a distance z.

In this formalism, the beam waist w_0 is taken to be the focal spot of the beam. At this point, the radius of curvature of the phase is infinite.

Several important parameters can be defined in terms of these quantities. In particular, the Rayleigh range is useful for understanding how the beam changes over a certain distance,

$$z_R = \frac{\pi w_0^2}{\lambda}. \tag{A.2}$$

It is useful to note that after a distance z_R on either side of the focus, the beam radius will have increased from w_0 to $\sqrt{2}w_0$.

The beam will have a divergence angle given by approximately

$$\theta \approx \frac{\lambda}{\pi\omega_0}. \tag{A.3}$$

Another useful quantity is the number of Fresnel zones in the beam, which is the number of times the phase wraps over the transverse extent of the beam. A Gaussian beam exactly at the focus will have a flat phase, while the same beam, some distance away from the focus, will have phase curvature- eventually wrapping and forming another Fresnel zone.

Appendix B

Description of the Laser System

B.0.1 Ultrafast Pulses Generated by Ti:Sapphire Oscillators

Titanium-doped sapphire ($Ti:Al_2O_3$, "Ti:Sapphire") laser systems have recently found a number of applications. Ti:Sapphire is an excellent gain medium for near-IR wavelengths, and is readily passively mode-locked [227–234], operating in a pulsed configuration.

The Ti:Sapphire oscillators used in this thesis are constructed from a Brewster-cut crystal, two focusing mirrors to focus the green pump light into the crystal, an output coupler and end mirror to form the ends of the cavity, and two prisms to compensate for dispersion. This type of oscillator is capable of running in CW mode (peak power around 1 W for 4-5W pumping laser) and also in mode-locked or phase locked operation. When the pulse is emitted, it is around 100 fs and on the order of half a Watt. The repetition rate is set by the length of the cavity and is around 80 MHz.

In order to understand the pulsed operation of these lasers, it is instructive to understand the mechanism by which they become pulsed; Kerr-lens mode-locking.

B.0.1.1 Kerr lens mode-locking

Oscillators operate under two basic configurations; continuous wave (CW) and mode-locked (sometimes called phase-locked). When operating in CW, the crystal is being pumped, typically with 532 nm light (frequency-doubled YAG) and is continuously undergoing stimulated emission, and a stable monochromatic beam is emitted.

Kerr lens mode-locking is a type of passive mode-locking which utilizes the optical Kerr effect. The optical Kerr effect occurs when a material's refractive index changes as a function of an external electric field. It was first observed around 25 years ago [230]. Typically, Ti:Sapphire oscillators can mode-lock between 40-100 nm of bandwidth, although not all of these configurations are stable. Depending on the cavity configuration and dispersion, the pulse duration can be anywhere from the order of 10's-100's of femtoseconds [233].

As discussed in relation to phase matching in Eqn. 4.1, the Kerr lens effect stems from the nonlinear index of refraction of the laser crystal [235], where, neglecting higher orders,

$$n \approx n_0 + n_2 \tag{B.1}$$

$$\approx n_0 + \tilde{n_2} I \tag{B.2}$$

where n_i is the i^{th} order in the expansion and I is the laser intensity. More generally, the time-dependent polarizability of a material can be considered,

$$P(t) = \epsilon_0 \left[\chi^{(1)} E(t) + \chi^{(2)} E(t)^2 + \chi^{(3)} E(t)^3 ... \right] \tag{B.3}$$

where ϵ_0 is the free-space permitivity, $E(t)$ is the time-dependent electric field, and $\chi^{(i)}$ is the i^{th} term in the expansion of the electric susceptibility.

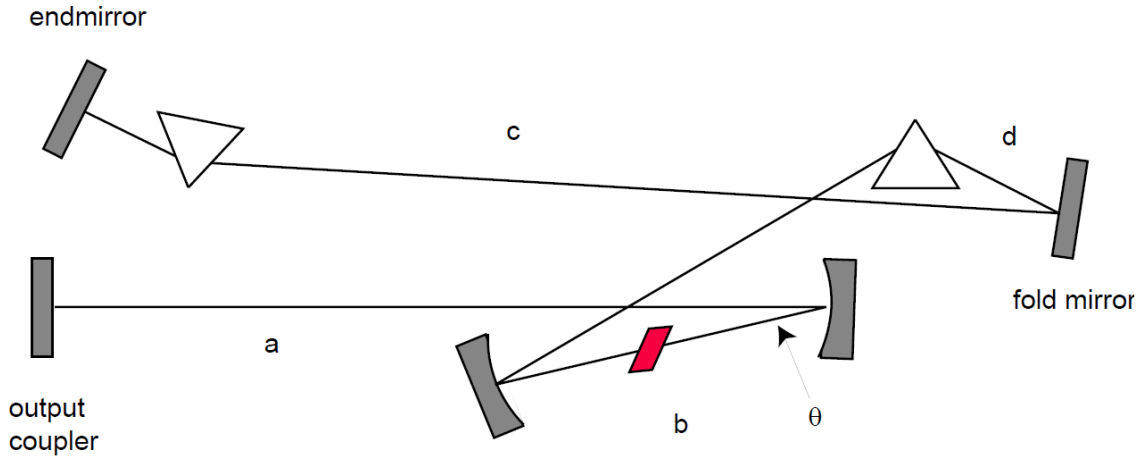

Figure 1. Parameters of a standard Ti:Sapphire laser cavity.
a = ~62cm, b = 10.4 cm, t = 16° , total prism separation (c+d) = ~62cm

Figure B.1: **Schematic of a Ti:Sapphire oscillator cavity**. Schematic and important lengths in a cavity. Figure adapted from Ref. [236].

The bandwidth, center wavelength, spectrum, and mode output by an oscillator depend sensitively on all of the optics being correctly aligned and cleaned. The position of the prisms greatly affect the bandwidth. Because time and frequency are conjugate variables, it is important to have a high bandwidth; as this will support a shorter pulse. For a Gaussian pulse, the time-bandwidth product for a transform-limited pulse is given by the uncertainty relation,

$$\Delta t \Delta \nu > 0.44 \tag{B.4}$$

where Δt is the full width at half maximum (FWHM) of the pulse duration and $\Delta \nu$ is the FWHM of the spectrum.

B.0.2 Chirped pulse amplification system

After the beam emerges from the oscillator, it is not yet it is sent into a Ti:Sapphire amplifier. The amplifier accomplishes three tasks; it increases the average power by a factor of about 20, decreases the repetition rate by a factor of about 40,000, and shortens the pulse by about a factor of 6. This results in an ultrafast high average power, high peak power, high energy pulse. The laser system used for the work in this thesis is a KMLabs Dragon.

Although there are many different configurations of amplifier, the work in this thesis uses a ring amplifier configuration, as illustrated in Fig. B.2. The four main sub-systems of the amplifier are the pulse shaper, the stretcher, the amplifier ring, and the compressor. The stretcher elongates the pulse temporally, thus decreasing the peak intensity, and allowing it to pass through the amplifier ring without burning any of the optics or the amplifier crystal. The compressor re-compresses the pulse temporally, and outputs an ultrafast high peak-intensity pulse. The geometries of the stretcher and compressor can distort various spectral characteristics of the pulse, causing it to not necessarily be Fourier transform limited, and therefore not as short as possible. These distortions are what causes the need for a pulse shaper, and will be discussed next.

B.0.2.1 The Pulse Shaper

Immediately after the oscillator, the beam is sent through the pulse shaper based on designs discussed in Ref. [237–239]. The purpose of the pulse shaper is to compensate for distortions due to slight misalignments in the stretcher and compressor of the amplifier [237, 238].

A laser pulse or other waveform can be mathematically expressed in a number of ways, but one convenient way is in time and frequency space. Temporally, a compressed, amplified pulse is on the order of 20 fs. This number refers to the amplitude of the pulse in time, but the pulse is a complex waveform– it also contains a temporal phase. The pulse must also be considered in the Fourier conjugate space; the wavelength spectrum. Similarly, there is a spectral phase in addition to the spectral amplitude; which will likely be familiar as this is what is viewed on a spectrometer.

Consider a complex waveform and its Fourier transform, expressed in time and frequency space:

$$\tilde{E}(t) = A(t)e^{i\Phi(t)} \tag{B.5}$$

$$E(\omega) = a(\omega)e^{i\phi(\omega)}. \tag{B.6}$$

Neglecting for a moment the physical sources of the phases, consider a polynomial expansion

of the spectral phase. It is not necessary, but often convenient, to work with spectral phase.

$$\phi(\omega) = \phi_0 + \tag{B.7}$$

$$\left.\frac{d\phi}{d\omega}\right|_{\omega_0} (\omega - \omega_0) + \tag{B.8}$$

$$\frac{1}{2!}\left.\frac{d^2\phi}{d\omega^2}\right|_{\omega_0} (\omega - \omega_0)^2 + \tag{B.9}$$

$$\frac{1}{3!}\left.\frac{d^3\phi}{d\omega^3}\right|_{\omega_0} (\omega - \omega_0)^3 + ... \tag{B.10}$$

$$\frac{1}{n!}\left.\frac{d^n\phi}{d\omega^n}\right|_{\omega_0} (\omega - \omega_0)^n \tag{B.11}$$

Physically, each of the terms in Eqns. B.7 has a different effect on the waveform. The first term, ϕ_0 is simply a constant offset and can often be neglected. The second term is a linear phase term, and shifts the phase around in time, as per the Fourier shift theorem. However, the point of $t = 0$ in time is arbitrary, so for the purpose here it may be neglected as well.

The third term in the expansion is known as quadratic phase, and is sometimes called chirp (not to be confused with spatial or angular spatial chirp). The effect of chirp in the temporal domain is that it stretches or compresses the pulse temporally- this is the chirp meant by the *chirped pulse amplification* system.

The next term is the cubic phase, which is typically caused by an incorrect angle of one of the gratings in the stretcher or compressor. The next higher order term (not shown) is known as 4^{th} order phase. Higher terms can and do exist in the spectral phase due to aberrations in the system, but they are often smaller than these first few terms. An exception is sinusoidal phase, which can be caused by misaligned chirped mirrors, and is not readily approximated by a polynomial expansion.

At this point, having a large amount of complicated phase may seem like it could potentially ruin the pulse's temporal characteristics unless it is carefully compensated for by small adjustments in the stretcher and compressor. Luckily, the pulse shaper and its algorithm can fairly easily compensate for many radians of arbitrary phase.

The primary components of the pulse shaper are a grating and spatial light modulator (SLM). The beam is sent into the pulse shaper and reflected from a blazed grating, which serves to spectrally

disperse it. It is then incident upon a SLM (Boulder Nonlinear Systems Model P12,288); a liquid crystal device comprised of 12,288 vertical pixels and capable of adding various amounts of phase delay. Since the pulse is now dispersed into its spectrum, every pixel in the SLM controls the spectral phase corresponding to a particular range of wavelengths in the spectrum. A spectral phase can be applied to the SLM, imprinted on the wavefront, and travel onward with the wave- superposing with whatever other spectral phase changes the pulse may encounter. The pulse shaper has a vertically folded design: the beam is directed slightly downward and travels back along the path it came (including re-encountering the grating, and un-spectrally-dispersing it), until it exits the pulse shaper.

How is the spectral phase from the SLM that goes on the pulse chosen? One excellent choice is the freezing phase algorithm [240], which sequentially moves through a chosen number of pixel groups on the SLM and tries out a set number of different phase values between 0 and 2π. The feedback parameter is the intensity of a second harmonic process: indeed, much like high harmonic generation, second harmonic light is generated more efficiently for shorter pulses. The more the incidental spectral phase in the rest of the amplification system is compensated for, the shorter (temporally) the pulse will be. For each pixel group, the phase value which produces the brightest second harmonic signal is selected. This algorithm is convenient because it is agnostic to the particular shape of the system's spectral phase; it need not be a continuous function approximated well by a polynomial. The feedback system is implemented after the entire amplification system, so the chirp imparted by the stretcher and then removed by the compressor is essentially unknown to the system: only the "net" phase is seen.

B.0.2.2 The stretcher

The stretcher, consists of gratings that elongate the pulse temporally. In fact, the design of the stretcher is somewhat similar to the design of the pulse shaper. The beam is spectrally dispersed using gratings to introduce quadratic spectral phase, and this results in a much longer pulse duration.

B.0.2.3 Amplification and pulse picking

Before the beam is amplified, it must be cut down to the correct repetition rate. The 80 MHz pulse train coming out of the oscillator is decreased through several steps via a delay generator, and is neatly reduced to the final rate via a Pockels cell. The Pockels cell uses the Pockels electro-optic effect to very quickly induce birefringence in a crystal. The incident beam is very well polarized, and when the Pockels cell is "off", the crystal cross-polarizes with the beam and extinguishes it. When the cell is "on", the beam is allowed to pass through and enter the amplifier ring.

The amplifier ring is a multi-pass system that passes the beam through the amplifier crystal about 10 times, before it is kicked out by a pickoff mirror. The Ti:Sapphire amplifier crystal is cryogenically cooled (Cryomech PT90) to reduce thermal lensing using a closed-loop helium system and is pumped with around 80 W of a frequency doubled Nd:YAG, which puts out 90 ns pulses of 532 nm laser (Lee Laser LDP-200MQG-HP). It is important that the pump laser is timed to pump the crystal while the seed beam from the oscillator is present, in order to ensure stimulated emission. This is achieved by sending a coincidence trigger signal from the oscillator to the control box of the pump laser. Within the ring, a mask consisting of 11 holes (though not all need be used) is inserted in order to spatially filter the beam, and a spectral filter is inserted as well to combat gain narrowing.

B.0.2.4 The compressor

Now that the beam has been amplified, it must be temporally re-compressed. Much like the stretcher, this is achieved with gratings. It also passes though a waveplate-polarizer pair allowing the output power to be modulated. Output power is around 6W for a 3 kHz repetition rate, and about 10 W for a 5 kHz rep rate. In each case, the pulse energy is on the order of 2 mJ, and the transform-limited pulse duration is around 20 fs. [241]

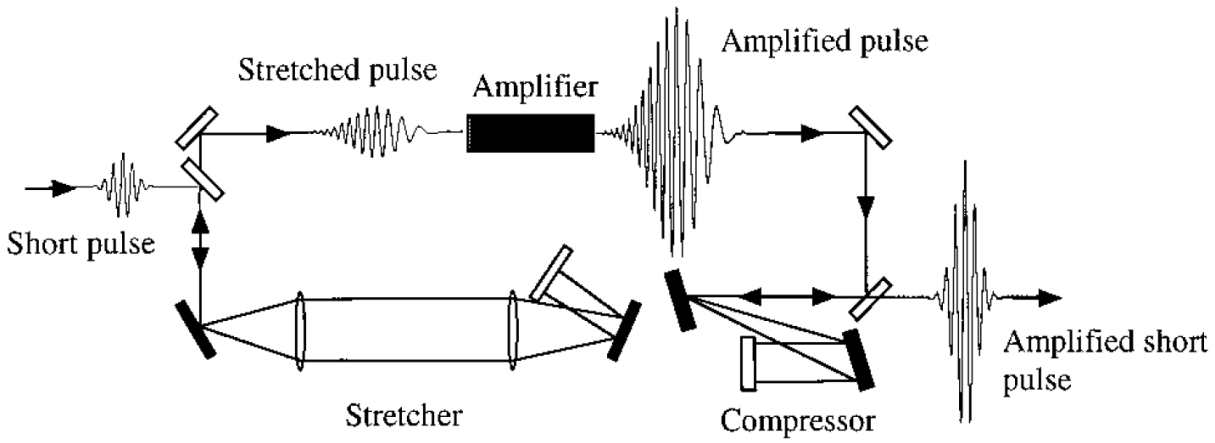

Figure B.2: **Schematic of chirped pulse amplifier**. The pulse is temporally stretched, then amplified, and then temporally compressed. Adapted from Ref. [241].